INVESTIGATING THE TEMPORAL AND SPATIAL VARIABILITY OF PRECIPITATION

A Dissertation Presented to
the Faculty of the Department of Earth and Atmospheric Sciences
University of Houston

In Partial Fulfillment
of the Requirements for the Degree
Doctor of Philosophy

By

James H. Trammell

May 2015

INVESTIGATING THE TEMPORAL AND SPATIAL VARIABILITY OF PRECIPITATION

James H. Trammell

APPROVED:

Dr. Xun Jiang (EAS), Chairman

Dr. Liming Li (Physics), Co-Chairman

Dr. Robert Talbot (EAS)

Dr. Yunsoo Choi (EAS)

Dean, College of Natural Sciences and Mathematics

ACKNOWLEDGEMENTS

My deepest gratitude goes to my advisors, Dr. Xun Jiang and Dr. Liming Li. Without their guidance, support, and encouragement, I would not have been able to finish this dissertation in a timely manner. They have shown me what a true scientist is, and their boundless enthusiasm for research has inspired me throughout my graduate career.

I would also like to thank my additional committee members, Dr. Robert Talbot and Dr. Yunsoo Choi for their valuable comments and advice in finalizing this research. Furthermore, I acknowledge my colleagues: Maochang Liang, Mao Li, Jing Zhou, Eric Fetzer, Yuk Yung, Guangjun Zhang, and Angela Kao.

Finally, my special appreciation goes to my family, to my parents, parents-in-law, and my wife and children: Kelly, Ethan, and Alexis. Without their support and sacrifice, this dissertation would not have been possible.

INVESTIGATING THE TEMPORAL AND SPATIAL VARIABILITY OF PRECIPITATION

An Abstract of a Dissertation
Presented to
the Faculty of the Department of Earth and Atmospheric Sciences
University of Houston

In Partial Fulfillment
of the Requirements for the Degree
Doctor of Philosophy

By

James H. Trammell

May 2015

Abstract

To explore the temporal and spatial variability of precipitation, a statistical tool called Principal Component Analysis (PCA) is applied to precipitation data from Tropical Rainfall Measuring Mission (TRMM), Global Precipitation Climatology Project (GPCP), and Community Atmosphere Model (CAM5). Results for the tropical domain reveal the first leading mode is related to the El Niño Southern Oscillation (ENSO). Further, it is found that the second principal component mode demonstrates correlation with a separate phenomenon, named El Niño Modoki. Results show a positive phase of El Niño Modoki produces positive precipitation anomalies over central Pacific and negative over western and eastern Pacific, analogous to those of typical ENSO episodes. Both observations and the CAM5 model are able to capture the ENSO and El Niño Modoki signals in the tropical precipitation, although the signals in the model are weaker than the observation. In the polar regions, spatial analysis and time series correlations with Northern Annular Mode/Southern Annular Mode Indices suggest the strength of the polar vortex can influence the temporal and spatial variability of precipitation in the high and mid-latitudes. The CAM5 precipitation simulations demonstrate patterns similar to that of the observed GPCP, although they slightly under predict magnitudes.

Next, high and low precipitation areas are defined with climatological monthly mean precipitation larger than 200 millimeters per month (mm/mon) and less than 50 mm/mon. Observed temporal variation reveals that precipitation has an increasing tendency in the wet areas and a decreasing tendency in the dry areas. The NASA Goddard Institute for Space Studies (GISS) model is utilized, and simulations imply that

the increasing greenhouse gases can affect the temporal variation of precipitation over the wet and dry areas, consistent with the observed “rich-get-richer” mechanism. Results further reveal that the atmospheric dynamics related to the convective stability, and hence the vertical motions, contribute to the increased precipitation over the tropical area as a result of global warming. However, the vertical motion in the dry areas does not demonstrate significant change, making the physics of the negative trend of precipitation in these regions more complicated.

Table of Contents

List of Figures

PAGE

List of Tables

PAGE

Chapter 1

Introduction

Broadly, this dissertation aims to investigate the temporal variability and spatial pattern of precipitation using satellite data, observations, and simulation models.

The atmospheric branch of the hydrological cycle is a crucial component of weather and climate in which water vapor leaves the surface by evaporation and returns to it by precipitation**.** The total mass of water vapor is related to the atmospheric temperature by the Clausius-Clapeyron equation. Unlike the relationship between water vapor and air temperature, there is no simple relationship between precipitation and temperature at the global scale even though surface temperature is correlated with local precipitation (Trenberth and Shea, 2005; Adler *et al*., 2008) and precipitation extremes (Allan and Soden, 2008; Liu *et al*., 2009). In addition, large discrepancies in the linear trend of global precipitation exist among different observational studies and climate models (Allen and Ingram, 2002; Adler *et al*., 2003; Trenberth *et al*., 2003; Held and Soden, 2006; Gu *et al*., 2007; Wentz *et al*., 2007; Adler *et al*., 2008; Stephens and Ellis, 2008; Liepert and Previdi, 2009; Trenberth, 2010). The above debate makes it urgent to carefully examine this important scientific topic: How does precipitation vary with time in response to global warming?

A recent observational study (Li *et al*., 2011) provides the spatial pattern of variations of precipitation over the last two decades (i.e., 1988-2009). It gives evidence

that the areas of great precipitation are getting wetter while the areas of least precipitation are getting drier. With these scenarios, it is apparent that precipitation extremes may occur in the form of more frequent severe storms and flooding in one region and of drought and extreme heat in the other.

A proposed explanation for these phenomena is contained in the atmospheric response to the effects of global warming; altering precipitation, temperature, and water vapor. In Li *et al*., 2011, two diverse circumstances were explored on a global scale: areas with precipitation less than 50 mm/month and areas with precipitation greater than 200 mm/month. The analysis of the data sets led to discovering the statistical characteristics of these variables, including intraseasonal variability, interannual variability, and long-term trend. Also, current atmospheric models were used to capture the characteristics of precipitation in an attempt to quantitatively simulate the precipitation trend over the globe.

In Li *et al*., 2011, a related parameter, recycling rate (R), was employed to examine the temporal variation of precipitation in response to global warming (Chahine *et al*., 1997; Li *et al*., 2011). The recycling rate of atmospheric moisture compares the rates of precipitation (P) to that of the rate of total column water vapor (W) via the equation $\Delta R/R = \Delta P/P - \Delta W/W$; where ΔX and X represent the change and mean value of variable X (i.e., R, P, and W) during the time period. In physics, the recycling rate is the same as other parameters, which include residence time (Chahine *et al*., 1992; Trenberth, 1998) and a non-dimensional ratio between the precipitation sensitivity to water vapor sensitivity (Stephens and Ellis, 2008).

From the observational analysis, the results revealed that regions located at the Inter-Tropical Convergence Zone (ITCZ) illustrated a positive recycling rate; implying precipitation trend is increasing faster than water vapor trend. Also, at the two sides of the ITCZ, a negative recycling rate demonstrated water vapor trend is increasing faster than precipitation trend. This conveys that areas that already receive high precipitation are getting wetter, and areas that already receive low precipitation are getting drier. Since the global average of recycling rate has decreased, the implications are that the negative recycling is stronger, or spatially larger, than the positive recycling rate. The qualitative consistency between the two recycling rates confirms that, globally, the recycling rate of atmospheric moisture has decreased over the last two decades. These findings over the wet and dry areas provide a new perspective to examine the amplification of precipitation extremes in response to global warming. This study provides the background and basis for further research contained herein.

1.1 Motivation

Increasing greenhouse gases and their contribution to global warming have been studied and argued for years. We explore the effect and role global warming may have on the temporal variation and spatial pattern of precipitation and its possible influence on causing precipitation extremes. Scientists suggest some different mechanisms on evaluating the relationship between global warming and precipitation. One, the "rich-get-richer" mechanism, is defined as the tendency of convergence zones with large climatological precipitation to receive more precipitation and for subsidence regions with low climatological precipitation to experience reductions under global warming. This

mechanism tends to yield increased precipitation associated with moisture increase in a climatological convergence region (Chou and Neelin, 2004; Neelin *et al*., 2006; Chou *et al*., 2009). Some observational studies (Neelin *et al*., 2006; Allan and Soden, 2008; Li *et al*., 2011) have supplied qualitative evidence for the "rich-get-richer" mechanism. However, there are still some discrepancies between the observed amplifications of rainfall extremes and those predicted by models, implying that projections of future changes in rainfall extremes in response to global warming may be underestimated (Allan and Soden, 2008). Furthermore, the exploration of the spatial pattern of temporal variation is limited. Therefore, the motivation for this research comprises the following four main important goals:

1. To quantitatively simulate the variability of precipitation in order to predict its fluctuation in the future
2. To understand the hydrological cycle as a response to global warming
3. To better understand the physics behind the temporal variation and spatial pattern of precipitation
4. To alleviate, forecast, and prepare for the consequences of drought in one area and flooding in another

In an attempt to quantitatively simulate the variability of precipitation, we investigate its temporal variation and spatial pattern on global and regional scales using multiple satellite-based data sets and observations. Additionally, we explore the surface temperature and omega to examine possible causes of this variation and look into factors that contribute most to the variance in the data. This will aid forecasters in the prediction of precipitation in the future and help in understanding the hydrological cycle as a

response to global warming. In order to provide a numerical basis to better understand the physics that drive the temporal and spatial variability of precipitation, we investigate the meridional circulation through observations and global climate model simulations to see how they may possibly contribute to precipitation extremes in the future. Also, by applying the Principal Component Analysis (PCA) method to both observations and model simulations, factors that contribute most to the variance in the data can be determined and further investigated. These analyses and findings will provide valuable information and insight to decision makers as they prepare for the consequences of drought in one area and flooding in another.

1.2 Dissertation Overview

This dissertation focuses on studying the temporal and spatial variability of precipitation using satellites, observations, and simulation models. Although each chapter here is listed separately, all are related, focusing on different meteorological scales and analyses. Next, we will explain why this research is important and what it aims to achieve.

In Chapter 2, we first explore the temporal and spatial variation of precipitation on a global scale; then we focus on a case study over Texas in 2011. We use TRMM satellite precipitation data to study the global spatial variability. Then, we study the global surface temperature and 500 millibar (mb) omega using NCEP2 reanalysis data, revealing their spatial variance. Next, a case study is explored over Texas during the historic drought of 2011. Spatial variations in climatological precipitation are plotted for Texas and compared with those from the summer months of 2011. This allows for the investigation

of rainfall during La Niña episodes and its deviation from normal. Temporal variations were plotted against Southern Oscillation Index (SOI). As a result, the cross correlation between precipitation and SOI provided a possible forecasting factor for drought over Texas as increasingly positive values of SOI were found to precede the low rainfall events by 5 months. Next, temporal and spatial variations in surface temperature from NCEP2 reanalysis data are used to discover the relationship between precipitation and surface temperature over Texas, disclosing related feedbacks. Five hundred mb omega data from NCEP2 reanalysis are plotted over Texas revealing its temporal and spatial variability. The correlation between precipitation and omega confirms that omega is related to rainfall experienced within a region by the increased sinking motion and atmospheric stability thus helping to limit thunderstorm development. Finally, the PCA method is performed on the TRMM precipitation data over Texas, making known the modes that contribute most to the variance in the data. It was found that the first mode captured 21% of the total variance and determined that El Niño Southern Oscillation (ENSO) was the likely contributor.

In Chapter 3, we analyze the temporal and spatial variability of precipitation over tropical regions from observation and model. GPCP precipitation data are utilized as well as the National Center for Atmospheric Research (NCAR) Community Atmosphere Model (CAM5). PCA is applied to the detrended, deseasonalized, and lowpass filtered precipitation data from GPCP and CAM5 model over 1979-2010. A linear trend is utilized for the time series, seasonal cycles are removed, and a lowpass filter is incorporated to the precipitation anomaly to remove the high frequency oscillation. PCA is then utilized to analyze interannual variability of GPCP precipitation in the tropics

(30°N-30°S). The first and second leading modes are identified and total variances calculated. The spatial distribution of the first leading mode (EOF1) is plotted for the tropical domain. A time series and power spectrum of the first leading mode (PC1) is plotted with Southern Oscillation Index (SOI) to help identify its correlation with ENSO. Next, the spatial distribution of the second leading mode (EOF2) is plotted for the tropical domain. A time series and power spectrum of the second leading mode (PC2) is plotted with El Niño Modoki Index (EMI) to help identify its correlation with the phenomenon known as El Niño Modoki. Similarly, PCA is applied to the CAM5 precipitation over the tropics (30°N-30°S) to investigate if the model can correctly simulate the influence of ENSO and El Niño Modoki on precipitation.

In Chapter 4, we analyze the variability of precipitation over subtropical and polar regions from observation and model. In addition to the GPCP precipitation dataset and CAM5 model previously introduced, NCEP2 reanalysis data are analyzed in this chapter. PCA is applied to analyze interannual variability of the GPCP precipitation in the Arctic (30°N-90°N) and Antarctic (30°S-90°S). The first leading modes are identified and total variances calculated. The spatial distribution of the first leading mode (EOF1) is plotted for the Arctic and Antarctic domain. A time series and power spectrum of the Arctic first leading mode (PC1) is plotted with the 300 mb Northern Annular Mode (NAM) index to aid in identifying negative and positive precipitation anomalies over the polar region and mid-latitudes. Secondly, a time series and power spectrum of the Antarctic first leading mode (PC1) is plotted with the 300 mb Southern Annular Mode (SAM) index to identify the corresponding precipitation anomalies. Similarly, PCA is applied to the CAM5

model simulations over the Arctic and Antarctic to investigate if the model can correctly simulate the variability of precipitation in the NH and SH high latitudes.

In Chapter 5, we investigate precipitation variations over wet and dry areas from observation and model. In addition to the GPCP dataset previously introduced, we employ the NASA Goddard Institute for Space Studies (GISS) atmospheric general circulation model coupled to the hybrid-isopycnic ocean model (HYCOM) to study precipitation, temperature, water vapor, and vertical pressure velocity. The high precipitation and low precipitation areas are defined as the areas with climatological monthly mean precipitation larger than 200 millimeter per month (mm/mon) and less than 50 mm/mon, respectively. Time series are plotted for each area, and from the temporal variation of precipitation, it is evident that the areas already receiving great precipitation tend to receive more while the areas already receiving little precipitation tend to receive less. Then, we use the NASA GISS-HYCOM model to investigate whether the model can capture the overall trends seen in the observations and reproduce the characteristics of precipitation. We conduct experimental simulations in a control run where the greenhouse gases are fixed and a historic run where the historic greenhouse gases are included. Similar simulations are conducted for temperature, water vapor, and vertical pressure velocity. The GISS-HYCOM model is utilized to examine the affect anthropogenic greenhouse gas emissions may have on the temporal variation of the meridional circulation and its associated residual vertical velocity. The increasing trend discovered in the historic simulation suggests an intensifying convection is occurring over the tropics, thus aiding in the enhanced precipitation experienced in those regions.

Chapter 2

Examine the Variability and Trend of Precipitation with a Case Study over Texas during the Drought Year of 2011

2.1 Introduction

The specific goals of this research include the examination of the variability and long-term trend of global precipitation. This chapter will also focus on a case study that investigates the variability of precipitation over Texas, specifically the drought of 2011. Beginning in October 2010, the majority of Texas experienced a relatively dry fall and winter. By March 2011, the state began to develop widespread extreme drought conditions. Precipitation records were re-established for anomalously low values in March–May 2011. This was followed by another record breaking dry spell in June–August 2011 while average surface temperatures rose 2.5°F above any previous record ever established in the state. Additionally, the 12 month rainfall total for October 2010–September 2011 fell far below the previous record set in 1956 (Nielsen-Gammon, 2011). The extreme lack of rainfall and high temperatures resulted in continued hardships for those tending crops and livestock. Conditions were so dry that many crops perished, and grass for livestock ceased to exist. Rivers and reservoir levels diminished as recharge from stream flow was at a minimum. By early fall of 2011, deep-rooted trees began to feel the impact, showing signs of declined health. These combined conditions set the stage for wildfires to ignite and spread beyond control. Several forest fires burned

intensely all around the state causing loss of homes and livestock, leaving behind charred ground and desolation. The drought of 2011 was the most intense one year drought in Texas since 1895, when records in the state first began. This study will explore the sources of these conditions and look for avenues to forecast their occurrence.

Herein, multiple data sets of precipitation, sea surface temperature, and reanalysis meteorological variables are introduced. Each of the tasks performed by this research is chronicled and documented with conclusions and findings. The answers discovered will aid in a better understanding of the temporal and spatial variability of precipitation, along with the physics that drive them. This will lead to accurate prediction of frequency and magnitude of precipitation assisting forecasters and scientists to alleviate, predict, and prepare for possible future precipitation extremes.

2.2 Data

The scope of this research consists of performing detailed data analysis of multiple datasets to interpret trends and variability.

In this dissertation, Tropical Rainfall Measuring Mission (TRMM) precipitation is employed. TRMM precipitation data (Version 7 3A12) are available at 0.25º × 0.25º (latitude by longitude) from 50ºS-50ºN. These data are 3 hourly averaged data from 1998 to the present. TRMM calibrated precipitation data combine precipitation estimates from several different instruments, including TMI, AMSR-E, SSM/I, and AMSU-B (Huffman *et al*., 2007).

The long-term global precipitation data set from the Global Precipitation

Climatology Project (GPCP) will also be utilized for this dissertation and was chosen because of its long period of record. This data set is constructed by combining precipitation information from many different sources (SSM/I, geostationary satellites, AIRS, TOVS, OPI, and gauge data). GPCP Version 2.2 precipitation data are obtained by merging infrared and microwave satellite estimates of precipitation with rain gauge data from more than 6,000 stations (Huffman *et al*., 2009). GPCP global monthly mean precipitation data are from 1979 to the present with grid size of 2.5° × 2.5° (latitude by longitude). These data are available for both land and ocean, with the latest version improved by applying a new updated climate anomaly analysis method for the gauge data and several correction schemes. These data combine several different components, including infrared, microwave, in situ, merged satellite, gauge data, and a calibration / validation component.

The extended reconstructed sea surface temperature (SST) data (1979-2001), containing a spatial resolution of 2º in both latitude and longitude directions, are utilized in this dissertation. Extended SST data are from Physical Sciences Division in the National Oceanic and Atmospheric Administration (NOAA) Earth System Research Laboratory.

Additionally, two meteorological reanalysis datasets, which include some dynamical fields, are used to conduct diagnostic studies. The two reanalysis data sets from the National Centers for Environmental Prediction/Department of Energy (NCEP/DOE) reanalysis 2 (NCEP2) and the European Center for Medium-Range Weather Forecasts (ECMWF) 40 year reanalysis (ERA40) have a horizontal spatial resolution of 2.5º × 2.5º (latitude by longitude). The NCEP2 data range from 1979 to the

present while the ERA40 data range from 1958-2001. The two modern reanalysis datasets have already been introduced in related documents (Kanamitsu *et al*., 2002; Uppala *et al*., 2005). Moreover, another data set named ERA-Interim is applied to the research, which is available from 1979-2013.

For the purpose of this chapter, we use Tropical Rainfall Measuring Mission (TRMM) precipitation data, chosen because of its fine spatial resolution of 0.25º × 0.25º (latitude by longitude) from 40ºS-40ºN. We employ the time period of January 1999-May 2013 for this research. TRMM calibrated precipitation data combine precipitation estimates from several different instruments, including TMI, AMSR-E, SSM/I, and AMSU-B.

Also, the National Centers for Environmental Prediction/Department of Energy (NCEP2) derived reanalysis data are calculated via monthly mean method for measurements of both omega and temperature. Omega data are utilized for the 500 mb pressure level reported in units of Pascal/day. Temperature data are employed for the surface level and reported in units of Kelvin.

The Southern Oscillation Index (SOI) is also studied within this chapter. The SOI is the atmospheric component of the El Niño Southern Oscillation (ENSO) and offers an indication of the development and intensity of an El Niño or La Niña event in the Pacific Ocean. The SOI is calculated by using the pressure anomaly differences between Tahiti, located in the central/eastern Pacific, and Darwin, located in the western Pacific. The pressure anomaly is obtained by subtracting the long-term mean from the monthly mean. The pressure anomaly difference is then divided by the standard deviation of the difference and multiplied by a factor of 10. Sustained negative values of SOI often

indicate an El Niño episode may occur, characterized by decreased trade winds and a warmer central and eastern Pacific Ocean. Sustained positive values of SOI often suggest a La Niña episode is probable, which is indicative of increased trade winds and a warmer western Pacific Ocean. These data are available online[1].

[1] Available at: http://www.cpc.noaa.gov/data/indices/soi

2.3 Trend and Spatial Variability of TRMM Precipitation, Surface Temperature, and Omega

The specific goal of this task includes the examination of the variability and long-term trend of global precipitation with a case study over Texas. This research aims to answer the following questions:

1. What is the spatial variation of global precipitation, temperature, and omega for the last several decades?

2. What is the spatial and temporal variation of precipitation, temperature, and omega over Texas?

3. Can the SOI be used to aid in forecasting drought?

4. Which factors contribute most to the variance in precipitation over Texas?

In the next section, we focus on investigating the spatial variability of TRMM precipitation, monthly mean temperature, and monthly mean omega on a global scale.

2.3.1 Global Analysis

One specific goal of this research incorporates the examination of the spatial variability of global precipitation. Results of precipitation data from TRMM climatology are shown in Figure 2.1 between 40°N-40°S, illustrating more rainfall in the tropical region than in the mid-latitudes.

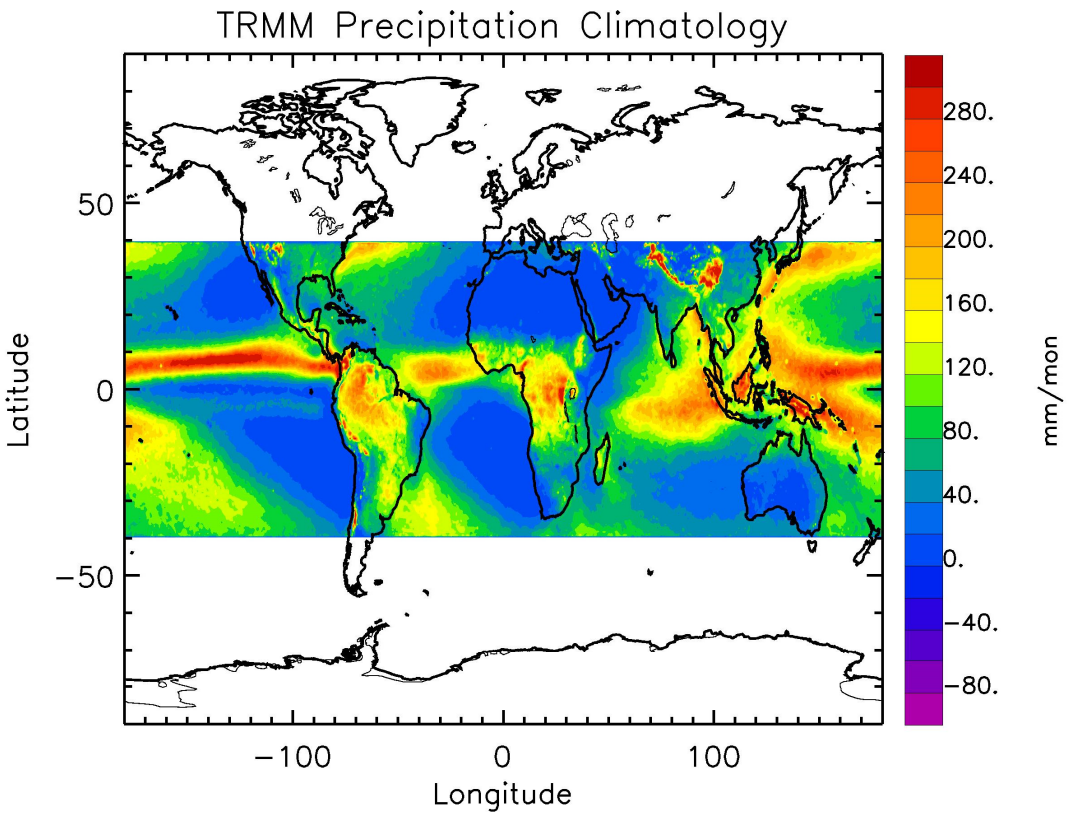

Figure 2.1. TRMM precipitation climatology averaged from Jan 1999 to May 2013 between 40°N-40°S. Units are mm/mon.

The high precipitation area is roughly the same as the Inter-Tropical Convergence Zone (ITCZ) identified by the highly reflective clouds (Waliser and Gautier, 1993). The low precipitation area comprises most of the other regions in the tropics and mid-latitudes. When examining the possible factors that influence the spatial variability of global precipitation, the occurrence and magnitude of several different events around the globe can play a significant role. The development and magnitude of the El Niño Southern Oscillation (ENSO) is one such event.

There exists several indicators in the Pacific Ocean that aid in the formation of an El Niño or La Niña episode. Monthly mean surface temperature climatology derived

from NCEP2 reanalysis data is shown in Figure 2.2. Surface temperature is higher in the tropics than in the high latitudes. Over the Pacific Ocean, surface temperature is high over the western Pacific and low over the eastern Pacific during the normal years. The influence of ENSO on the sea surface temperature (SST), surface pressure, winds, and convection is well known (Trenberth and Shea, 1987; Trenberth, 1997). Generally, ENSO causes warmer water to accumulate over the central and eastern Pacific via changes in the trade winds, ocean currents, and upwelling. These warmer waters create lower atmospheric pressure just above the ocean surface, in turn, causing negative values of omega and promoting vertical rising motion consistent with changes in the Walker circulation (Jiang *et al*., 2010). Convection and thunderstorm development is enhanced over those regions and, via transport, can cause changes in the spatial pattern of precipitation around the globe. Furthermore, sustained negative values of the Southern Oscillation Index (SOI) often indicate the development of El Niño episodes, demonstrating decreased or even reversed trade winds. During La Niña conditions, SST tends to be cooler in the eastern Pacific, with sustained positive values of SOI and increased trade winds. Also associated with La Niña events are positive values of omega over the eastern Pacific and the promotion of the associated vertical sinking motion. These repress convection and thunderstorm development and can lead to a decrease in precipitation over the eastern Pacific.

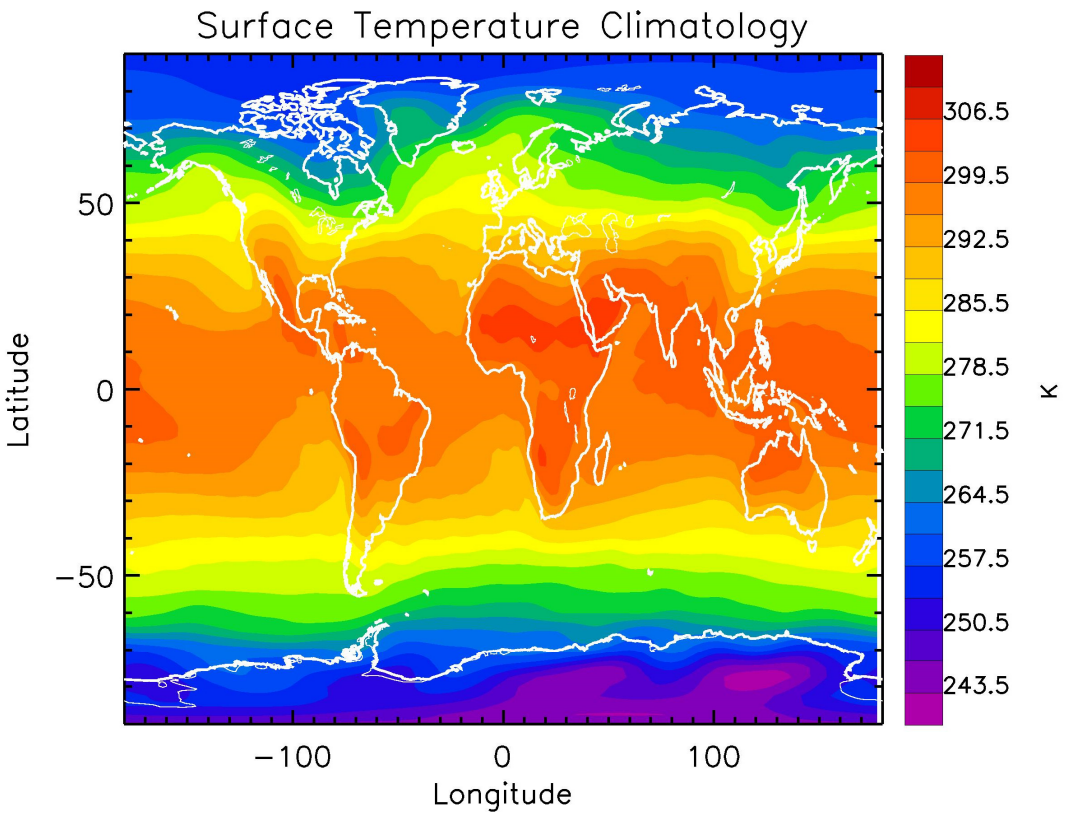

Figure 2.2. NCEP2 monthly mean surface temperature climatology averaged from Jan 1999 to May 2013. Units are Kelvin.

To investigate the differences in trade winds, several instances can occur that promote or negate the change. Opposing the normal Northern Hemisphere flow of the trade winds, Kelvin waves move eastward (Gill, 1982). As the wave propagates, the sea surface will rise and fall by up to several inches over a period of weeks to months. Often these effects are minimal, but if the magnitude and duration are great, they can help nudge the Pacific Ocean into or out of an El Niño pattern.

Another phenomenon, the Madden-Julian Oscillation (MJO), can have its influence as well. Known as a pulse of atmospheric energy generated in the Indian Ocean every few weeks, MJO events can drive clusters of showers and thunderstorms

eastward across the tropical Pacific (Zhang, 2005). Additionally, westerly wind bursts (WWBs) can also assist in supplying energy to generate Kelvin waves. These clumps of west to east wind push directly against the trade winds, opposing their normal flow. They may span hundreds of miles with durations of a few days to several weeks. WWBs are an important aspect of ENSO's dynamics and should be treated as being partially stochastic and partially affected by the large scale ENSO dynamics themselves (Eisenman *et al*., 2005). WWBs can be bolstered by the flow funneling between pairs of low pressure centers, or cyclones, straddling the Equator. These can cause west to east ocean currents to progress into the central Pacific, counteracting the usual trade wind driven flow. The change in ocean currents can be the main source for warm water build-up in the central and eastern Pacific, creating minimal upwelling of deep, cold ocean water to the surface.

Demonstrated in Figure 2.3 is the monthly mean 500 mb omega climatology from derived NCEP2 reanalysis data. Omega (ω) is defined as the vertical change in pressure with time: mathematically, $\omega = dP/dt$, where P is pressure and t is time. It is used to describe the magnitude of vertical motion and may be converted into a parameter known as vertical velocity, given in units of meters per second. Since pressure in the Earth's atmosphere decreases with height from the surface, positive values of omega exhibit sinking vertical motion while negative values indicate rising motion. Discovering these values within a region can help assign probabilities of where convection and thunderstorm development might occur. There are negative omega over the western Pacific and positive over the eastern Pacific as shown in Figure 2.3, which suggest air is rising over the western Pacific and sinking over the eastern Pacific during typical years.

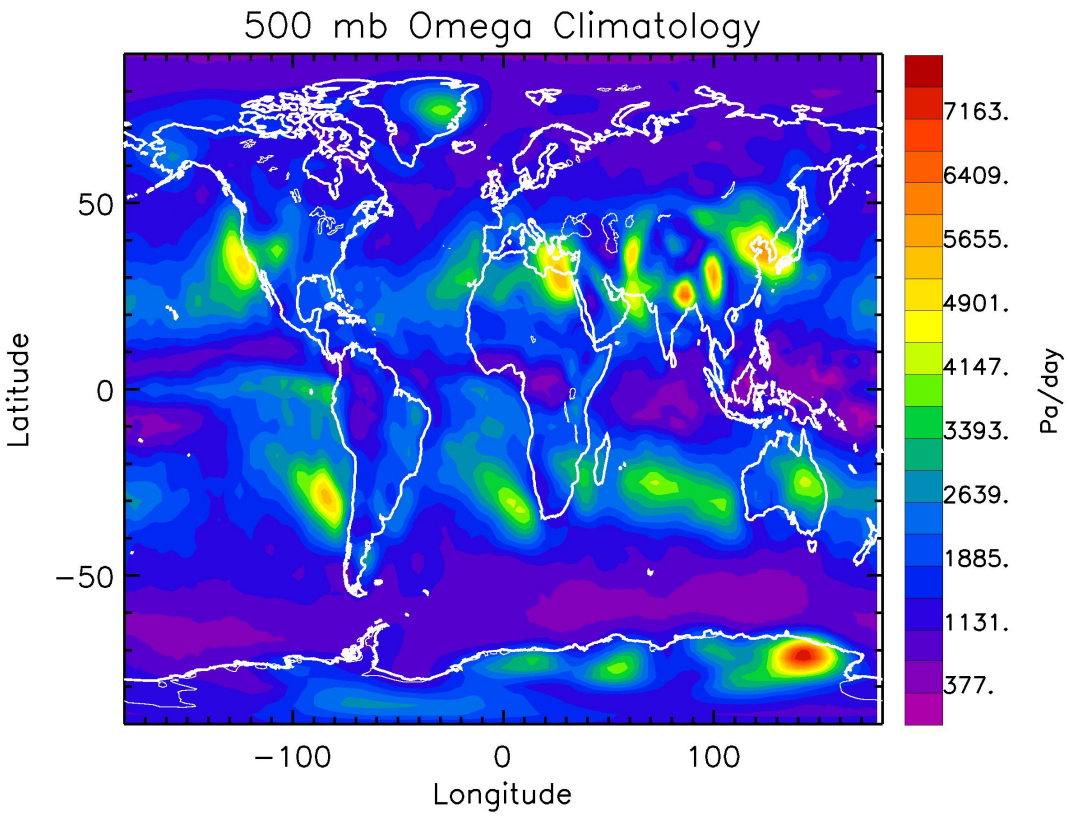

Figure 2.3. NCEP2 monthly mean 500 mb omega climatology averaged from Jan 1999 to May 2013. Units are Pa/day.

Another important component of the tropical ocean atmosphere interaction system, separate from the El Niño Southern Oscillation (Chang and Li, 2000), is known as the Tropospheric Biennial Oscillation (TBO). Over the Indo-Pacific region, monsoon rainfall exhibits this quasi-biennial oscillation (Mooley and Parthasarathy, 1984; Yasunari and Suppiah, 1988; Yasunari, 1990, 1991; Tian and Yasunari, 1992; Shen and Lau, 1995; Webster *et al*., 1998). One of the climate systems that influence atmospheric circulation, TBO, is defined as a tendency for a relatively strong "Indo-Australian" monsoon to be followed by a relatively weak one (Mooley and Parthasarathy, 1984; Yasunari and Suppiah, 1988; Yasunari, 1990, 1991; Tian and Yasunari, 1992; Shen and Lau, 1995;

Webster *et al*., 1998). It occurs in the season prior to the monsoon and involves coupled land-atmosphere-ocean processes over a large area of the Indo-Pacific region (Meehl, 1997). Observations show that the TBO signals appear not only in the Indian-Australian rainfall records but also in the tropospheric circulation, sea surface temperature (SST), and upper ocean thermal fields (Yasunari, 1991; Ropelewski *et al*., 1992; Lau and Yang, 1996; Chang and Li, 2001).

Following the TBO theory (Chang and Li, 2000), the warming in the western Pacific induces not only a strong monsoon but also a stronger Western Walker Cell, and thus, a surface westerly anomaly over the Indian Ocean. This westerly anomaly helps the cold sea surface temperature anomalies (SSTA) to persist through the succeeding seasons, leading to a weaker Asian monsoon and weaker Western Walker Cell in the following summer. The Western Walker Cell blows from the Indian Ocean to the western Pacific and creates a convergence area with the Eastern Walker Cell at the Indo-Pacific region (Meehl and Arblaster, 2002). Although considered separated from ENSO, the SSTA resembles those resulting from El Niño / La Niña conditions (Chang and Li, 2000).

In the next section, we focus on investigating the spatial and temporal variability of precipitation, temperature, and omega over Texas to better understand fluctuations in La Niña years compared to normal years. Additionally, the SOI will be examined to discover consistency at forecasting drought.

2.3.2 Case Study: Texas 2011

The case study for the drought of 2011 over Texas was chosen for its anomalous nature, as it was one of the worst droughts the state had ever recorded. In order to

investigate the variability of precipitation over Texas, TRMM precipitation climatology from January 1999 to May 2013 is displayed in Figure 2.4.

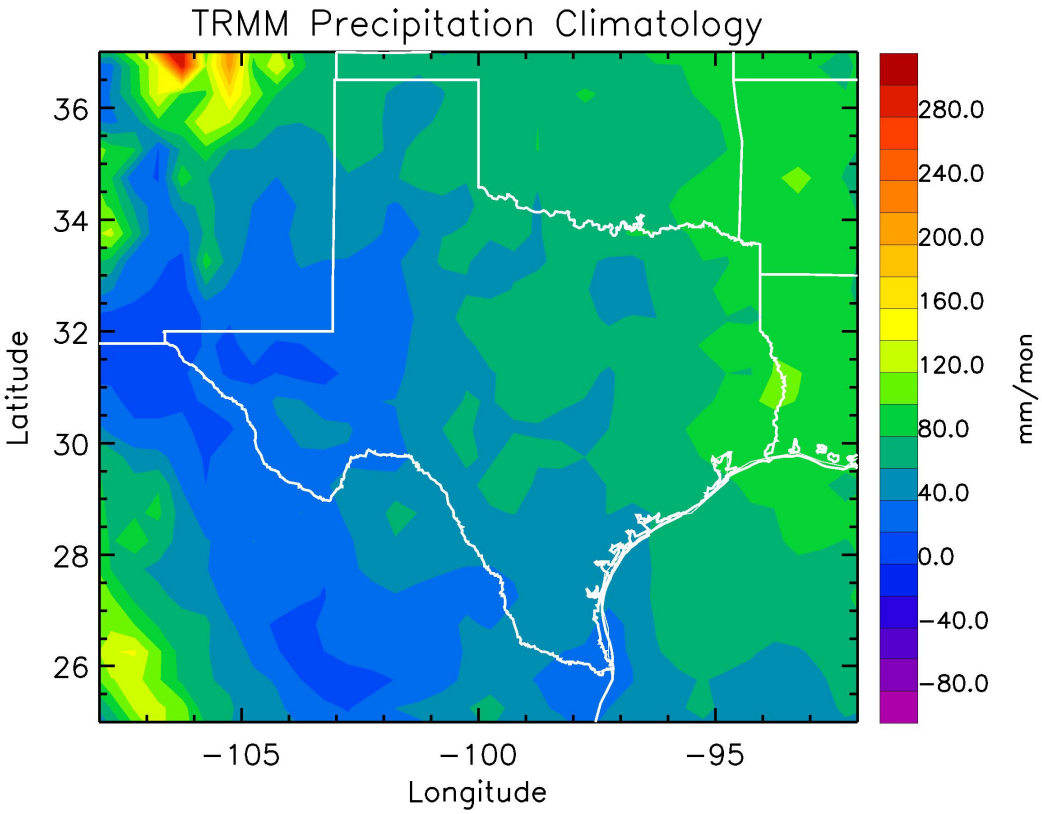

Figure 2.4. TRMM precipitation climatology averaged from Jan 1999 to May 2013 over Texas. Units are mm/mon.

From Figure 2.4, normal rainfall is more prevalent in the northeast/north-central region of the state. This is primarily associated with the seasonal southward migration of the subtropical jet and associated synoptic scale waves (Lydolph, 1989), coupled with the passage of cold fronts and the predominately southeast flow inland from the Gulf of Mexico, transporting ample moisture that evaporates from the ocean's surface. Background climatology during the wintertime suggests that precipitation anomalies over

the land areas that surround the Gulf of Mexico are also associated with cold air outbreaks (Cavazos, 1999). Cold air outbreaks are linked to changes in the sea-level pressure as well as the atmospheric thickness. When the warm waters of the Gulf of Mexico modify cold air masses, moisture and transport of moisture becomes significant. The divergent circulation associated with the subtropical jet entrance region tends to favor low-level northerlies across Mexico and Central America (Schultz *et al*., 1998), assisting in transport of moisture and convection from the Pacific Ocean into the Gulf of Mexico (Iskenderian, 1995; Rasmusson and Mo, 1993).

During analysis of the overall synoptic scale weather conditions of 2011, several weather charts were studied illustrating multiple meteorological variables available online[2]. A predominately zonal flow was found across much of the western United States with a very defined ridge of high pressure in the north-central and northeast regions for the majority of the summer months. This allowed for the typical seasonal southward migration of the subtropical jet into Texas to be diverted eastward of the state. Additionally, several high pressure centers were located all along the southern United States. These several factors helped to account for the drought-like conditions observed across Texas in 2011 as well as explain the flooding conditions experienced in the northeast, as mid-latitude cyclones would tend to track along the defined ridge.

[2] Available at: http://www.hpc.ncep.noaa.gov

Statewide observations were continuously gathered and monitored during the anomalous event. Toward the end of 2011, the drought monitor indicated 69.6% of the state of Texas was in D4 conditions, the worst category on the scale, with 90% of the state in either D3 or D4 conditions. It is interesting to note that in December 2010 none of the state of Texas was in D4 drought conditions and only 9.5% was in D3 conditions. Drought monitor data are available online[3]. To examine an example on a local scale, the City of Pasadena, located within Harris County along the Gulf Coast, only received 9.62 inches of rainfall from January 1-October 8, 2011, which is just above the amount of rainfall El Paso, on the border of New Mexico in west Texas, would normally receive for the same time period. Regionally, precipitation departures were astounding. Table 2.1 illustrates selected rainfall departures from normal for October 2010-October 2011.

TABLE 2.1. Selected precipitation departures from normal for October 2010–October 2011. Units for rainfall departure are inch.

Location	Rainfall Departure
Brenham	-29.70
Conroe	-33.00
Galveston	-22.36
Hobby	-29.89
Bush IAH	-30.94
Livingston	-34.88
Matagorda	-29.93
Tomball	-38.43
Victoria	-26.73

[3] Available at: http://droughtmonitor.unl.edu/Home.aspx

Houston Hobby Airport recorded its driest year ever, while Bush IAH ended 2011 with its third driest year on record. The lengthy time intervals between one inch rainfall events ended October 9, 2011, for the City of Houston, recording 3.02 inches of rainfall that day. The city went an astounding 257 days between one inch rainfall events with the previous record being only 192 days in 1917-1918. The 3.02 inches of rainfall on October 9 was the single greatest amount of rainfall for Houston since the landfall of Hurricane Alex in Mexico on July 2, 2010.

Table 2.2 illustrates observations all across the state of Texas for the entire 2011 year. It shows precipitation in inches and demonstrates the observational sites driest year on record. For comparison is 2011's precipitation along with how it ranked with the previous years. Highlighted in bold are those sites in which 2011 was within the top three driest years on record. Of the sites listed in the table, 10 out of 18 had one of their top three driest years ever.

TABLE 2.2. Precipitation observations for multiple locations in the state of Texas for 2011. Those highlighted in bold represent the sites where their 2011 rank was in the top three driest years on record. For comparison, the previous driest year and amount are shown.

Location	Precipitation (inches)	
	2011 (Rank)	Record Driest (Year)
Abilene, TX	16.83 (19th)	9.78 (1956)
Amarillo, TX	***7.00 (1st)***	9.56 (1970)
Austin, TX	19.68 (8th)	11.40 (1954)
Beaumont, TX	***31.02 (2nd)***	28.90 (1917)
Brownsville, TX	17.93 (14th)	11.59 (1953)
College Station, TX	***19.91 (2nd)***	17.80 (1988)
Corpus Christi, TX	***12.06 (2nd)***	5.38 (1917)
Dallas/Fort Worth, TX	25.88 (28th)	17.21 (1921)
El Paso, TX	5.27 (13th)	2.22 (1891)
Houston, TX	***24.57 (3rd)***	17.66 (1917)
Midland, TX	***5.49 (3rd)***	4.60 (1951)
Lubbock, TX	***5.86 (1st)***	8.73 (1917)
Lufkin, TX	33.75 (14th)	26.49 (1963)
San Angelo, TX	***9.23 (3rd)***	7.41 (1956)
San Antonio, TX	17.58 (14th)	10.11 (1917)
Victoria, TX	***13.08 (1st)***	15.89 (1988)
Waco, TX	27.63 (27th)	13.39 (1917)
Wichita Falls, TX	***12.97 (1st)***	16.07 (1970)

After taking a look at the precipitation observations of 2011, an update is given to the drought situation over Texas as of May 2014. Although some improvements have occurred, the current dryness continues the multi-year drought that has gripped Texas since late 2008. The drought monitor indicates severe to exception drought conditions across nearly all of central and northwest Texas and into most of the panhandle. D4 conditions, or exceptional drought, have risen from 13% of the state to 18% of the state. Currently 90% of the state is in some form of drought, up from 86% a month before this update and 80% three months ago. Across most of southeast Texas, regional

improvements have increased, with only moderate drought conditions found from Lake Livingston southward and westward to The Woodlands, as well as across Fort Bend, Brazoria, Wharton, and Matagorda counties; yet, severe drought conditions are found over Jackson and Victoria counties. Along the Gulf Coast, local counties have received total rainfall 25% of normal for the last five months with much of the area experiencing 30-50% of normal. Regionally across north Texas, Waco has recorded its 2nd driest January-April period ever with a total rainfall of only 3.39 inches. Dallas has encountered its 3rd driest with 3.93 inches of rainfall for the same time period. All precipitation station data are available online[4] from NOAA National Climatic Data Center.

In order to better understand the fluctuation of rainfall during La Niña years compared to normal years, we calculate the spatial variability of TRMM precipitation during the summer of 2011, specifically June through August, illustrated here in Figure 2.5. Typically, El Niño episodes allow for a persistent extended Pacific jet stream and amplified storm track from a residing low pressure located in the eastern Pacific (Ahrens, 2006). This enables a predominately zonal flow across the Pacific Ocean, assisting in transport of moisture and convection from the Pacific Ocean into the Gulf of Mexico and Texas. Conversely, typical La Niña events form a residing high pressure in the eastern Pacific, causing the Pacific jet stream to divert and minimize transport of moisture and convection into Texas (Ahrens, 2006). As such, the extreme La Niña year of 2011 aided in the abnormal lack of precipitation observed in Texas.

[4] Available at: http://www.ncdc.noaa.gov

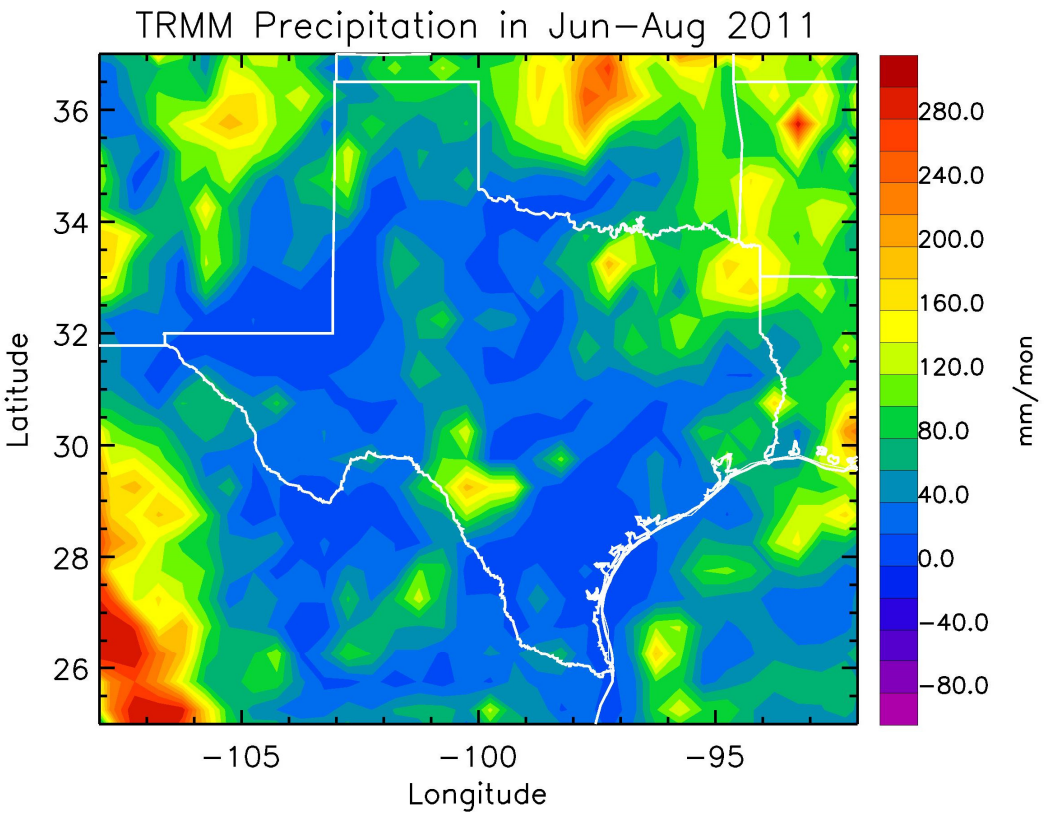

Figure 2.5. TRMM precipitation in June-August 2011 over Texas. Units are mm/mon.

A year of extremely low rainfall over an area can be observed by its effect on the water supply. Water is not only imperative for mere survival, but also serves as a major component for economic stability, logistics, and recreation. Toward the end of 2011, the total water storage for the state of Texas was 31,831,330 acre-feet, or 58.95% full, mainly due to the lack of inflow from dry rivers and streams coupled with increased water withdrawal to meet demands of statewide water utility districts. Consider this example: in mid-October 2011, the City of Houston increased its water withdrawal from Lake Conroe to 165 million gallons per day. This extraction resulted in approximately 17 inches per month of loss to the conservation pool, consequently placing the lake 2.47 feet

below its record low pool elevation. Conservation pool refers to water in a reservoir that lies above the dead pool and below the flood pool. In central Texas, a typical year of average inflow into the Highland Lakes Chain on the Colorado River is around 1.3 million acre-feet. For 2011, the inflow was around 100,000 acre-feet, an astounding lack of water inflow into these lakes. Table 2.3 illustrates selected lake levels in feet below conservation pool with percent capacity toward the end of 2011.

TABLE 2.3. Selected lake levels in feet below conservation pool in conjunction with percent capacity toward the end of 2011.

Lake	**Feet Below Conservation Pool (% Capacity)**
Conroe	-5.47 (69%)
Houston	-5.68 (77%)
Buchanan	-30.83 (38%)
Travis	-53.96 (35%)
Toledo Bend	-12.15 (58%)
Livingston	-3.88 (82%)
Somerville	-10.22 (38%)
Sam Rayburn	-13.52 (55%)
Texana	-11.99 (43%)

To update as of May 2014, lake levels across southeast Texas are up since the drought of 2011 while conditions in central, west, and north Texas continue to become more dire. Several lakes in north Texas fell to record low levels in April 2014 even though it tends to be the wetter time of year for that region of the state. The multi-year drought conditions continue to have significant impacts on lake levels and water supply. The total state water storage is 24,538,797 acre-feet or 64% of normal. Lake levels east

of I-35 are averaging 80-100% of capacity while lakes across west Texas are generally averaging 0-10% of capacity. Table 2.4 illustrates selected lake levels in feet below conservation pool with percent capacity as of May 2014.

TABLE 2.4. Selected lake levels in feet below conservation pool in conjunction with percent capacity as of May 2014.

Lake	Feet Below Conservation Pool (% Capacity)
Conroe	-0.62 (97%)
Houston	0.00 (100%)
Buchanan	-30.03 (38%)
Travis	-55.37 (34%)
Toledo Bend	-1.45 (94%)
Livingston	+0.14 (100%)
Somerville	-2.73 (81%)
Sam Rayburn	-1.97 (92%)
Texana	-3.86 (78%)

North Texas low lake levels include Lake Granbury, which established a new record low of 682.48 feet on April 20, 2014, with a previous record of 685.28 feet in August 1978. Lake Nocona established a record low of 815.62 feet on April 20, 2014, with a previous record of 816.95 feet in October 2000. Lake Ray Hubbard also set a new record low of 427.90 feet on April 3, 2014, with a previous record of 429.72 feet in October 2000. Inflow into the Travis and Buchanan lakes in March 2014 was 8,102 acre-feet or 9% of normal. For comparison, inflows in January-March 2014 were lower than that in 2011 (51,275 acre-feet in 2011 vs. 29,860 acre-feet in 2014) and, without significant rainfall, forecasts call for a continued decline in these storage levels.

There are seventeen key groundwater aquifer locations across the state. As of May 2014, eight locations saw an increase in ground water while nine experienced a decrease. Furthermore, the level of the Edwards Aquifer in central Texas is 0.79 feet away from reaching the stage 3 critical management level. With north and central Texas levels this low, water restrictions are being enforced. Thirty municipalities across the state have less than 90 days of remaining water supply and 7 have less than 45 days. 768 jurisdictions have mandatory water restrictions in place with an additional 389 having voluntary restrictions. A total of 1,157 systems out of 4,639 statewide are being affected or about a quarter of the state's systems. All lake and groundwater data are available online[5] from the Texas Water Development Board.

To further understand the anomalies between La Niña and normal years, we calculate TRMM precipitation difference between the summer of 2011 and climatology, specifically June–August. The difference is calculated by subtracting the climatology from the summer of 2011 precipitation. Figure 2.6 illustrates the spatial difference for the state of Texas and, with mostly negative values, acknowledges the deviation from normal. It is evident that the La Niña event of 2011 had a monumental effect on rainfall over Texas with almost the entire state below average.

[5] Available at: http://www.twdb.texas.gov

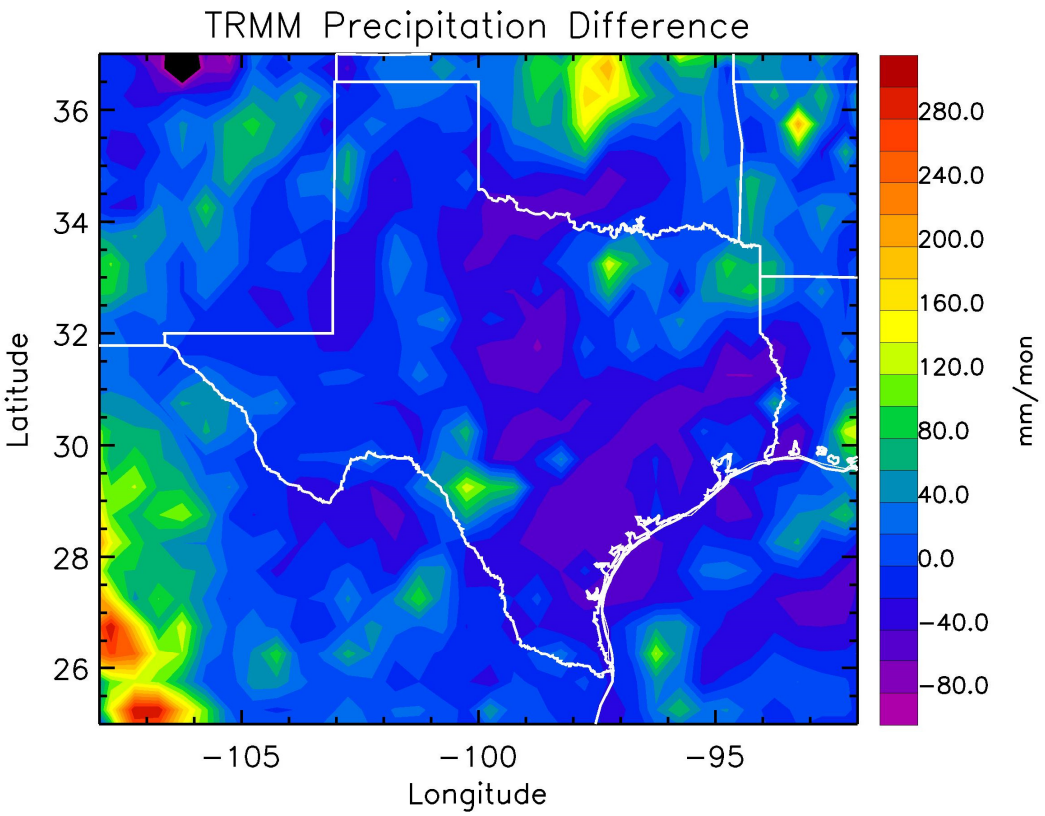

Figure 2.6. TRMM precipitation difference between the summer of 2011 and climatology. Units are mm/mon.

To further investigate the possible relationship between precipitation and Southern Oscillation Index (SOI), mean precipitation data from TRMM are calculated over Texas from January 1999 to May 2013 and plotted against SOI. Detrended and deseasonalized precipitation and inversed SOI data are shown in Figure 2.7a, revealing the temporal variation of precipitation over the Texas area. Precipitation averaged over Texas is shown as the black solid line with the inversed SOI overlain as the red dashed line. To better understand the relationship between precipitation and SOI, a lowpass filter is applied to remove the high frequency signals from both time series. The filter is constructed as the convolution of a step function with a Hanning window and chosen to

obtain a full signal from periods above 15 months and no signal from periods below 12.5 months. Lowpass filtered Texas precipitation data (black solid line) are plotted against lowpass filtered and inversed SOI data (red dashed line) in Figure 2.7b.

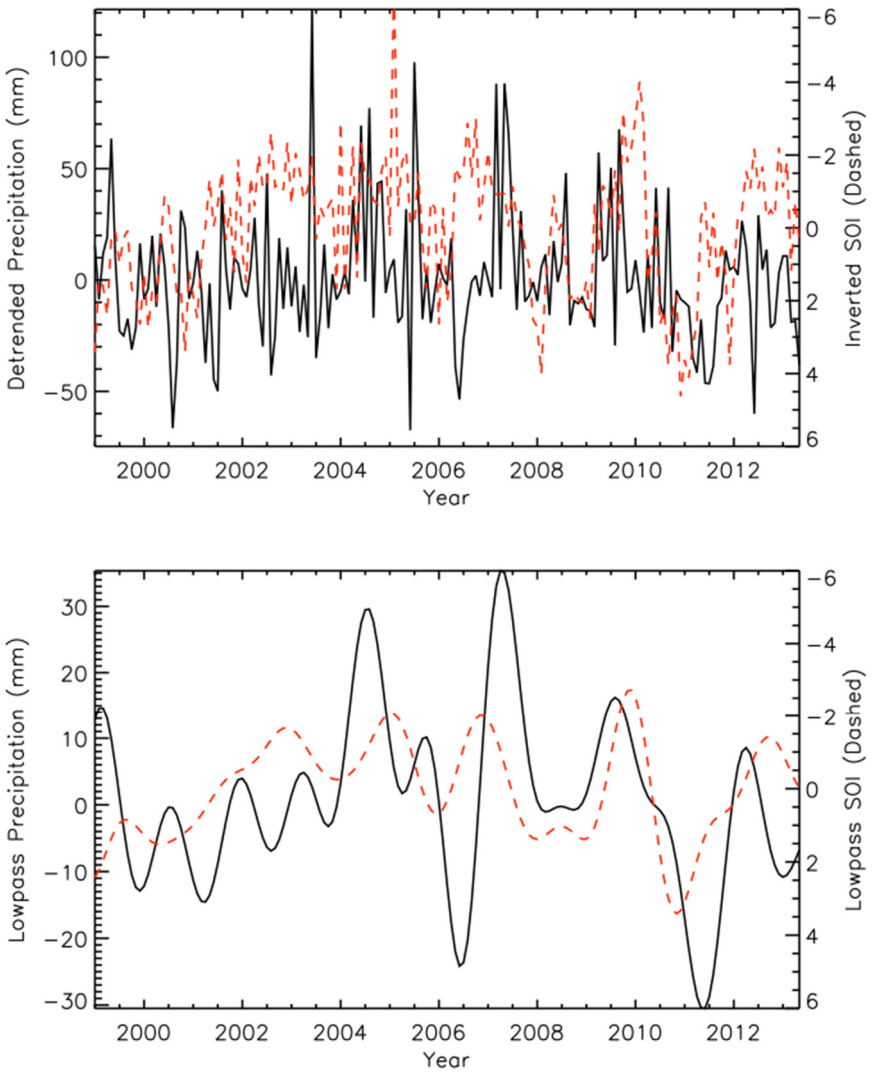

Figure 2.7. (a) Detrended and deseasonalized TRMM precipitation (black solid line) and detrended and inversed SOI (red dashed line) averaged over Texas from Jan 1999 to May 2013. (b) Lowpass filtered precipitation (black solid line) and lowpass filtered & inversed SOI (red dashed line). A 15 month lowpass filter was applied to the time series to remove the high frequency signals.

Since SOI and precipitation are anticorrelated, we plot the inverse of SOI to reveal its relationship with precipitation. Of considerable note are years 2006 and 2011, in which increases in SOI preemptively predict the possibility for below average rainfall. The maximum cross correlation coefficient between lowpass filtered precipitation and lowpass/inversed SOI is 0.5 when the lag is 5 months, suggesting that drought over Texas appears five months after a La Niña event or positive SOI index. This correlation provides a possible forecasting factor for drought over Texas by giving evidence of large scale circulation contributions from the tropical Pacific with below average sea surface temperatures, leading to strong sinking air and less precipitation over Texas.

One of the most significant developments in 2011 was the falling of the Palmer Drought Severity Index (PDSI) to its lowest level ever for the state of Texas. PDSI is thought to be the most influential index of meteorological drought used in the United States (Heim, 2002). It was developed with intentions of measuring the cumulative departure from mean in atmospheric moisture supply and demand at the surface, incorporating antecedent precipitation and surface temperature into a hydrological accounting system (Dai *et al*., 2004). In 2011, the PDSI fell a staggering 10 points from 2010, recording one of the worst droughts for the state. The value of -7.97 was established in September 2011, breaking the previous record of -7.80 in September 1956. To highlight the severity, the next closest value occurred in August 1918 at -7.09 (Nielsen-Gammon, 2011).

Monthly mean surface temperature climatology derived from NCEP2 reanalysis data is shown in Figure 2.8. It illustrates the spatial pattern of surface temperature climatology over Texas. Lower surface temperatures generally occur closer to the Gulf

Coast and increase westward as the atmosphere becomes drier and precipitable water values diminish. Precipitable water can be defined as the depth of liquid water that would be obtained at the Earth's surface if the total amount of water vapor within a column above it were to fully condense (Tuller, 1968).

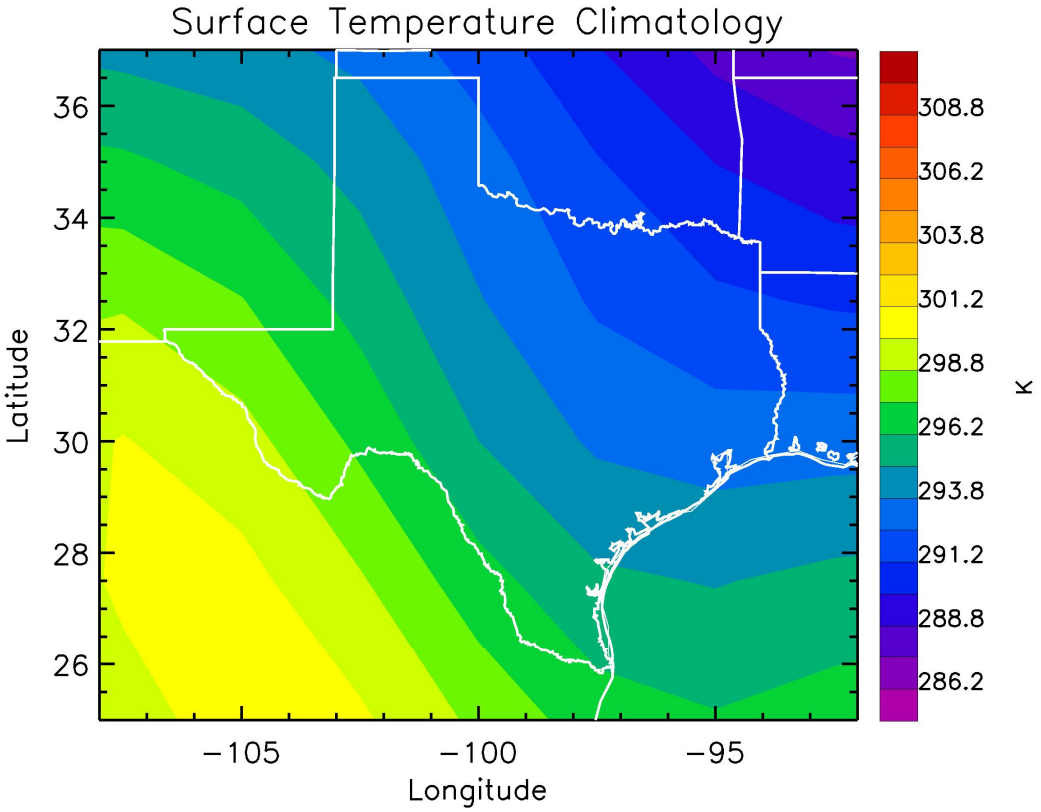

Figure 2.8. NCEP2 monthly mean surface temperature climatology averaged from Jan 1999 to May 2013. Units are Kelvin.

As precipitation and soil moisture decrease, a feedback occurs that causes higher than average surface temperatures (Brutsaert, 1998; Wang *et al*., 2008). This feedback is explained in the differences between latent and sensible heat. As energy is added to water, it changes its state or phase. The heat added during evaporation breaks the bonds between clusters of water molecules, creating individual molecules that escape the

surface as a gas. The heat used in the phase change from a liquid to a gas is called the latent heat of vaporization. It is referred to as "latent" because the heat is being stored in the water molecule to later be released during the condensation process. Latent heat is not felt or sensed as it does not raise the temperature of the water molecule and hence does not affect the air temperature. On the other hand, sensible heat can be sensed and is evident by its temperature: the higher the temperature, the greater the sensible heat content. When little water is available at the surface for evaporation, minimal transfer of latent heat energy occurs, and an absence of a latent heat energy flux exists at the surface. Therefore, most of the available energy is allocated to sensible heat transfer creating warmer air temperatures.

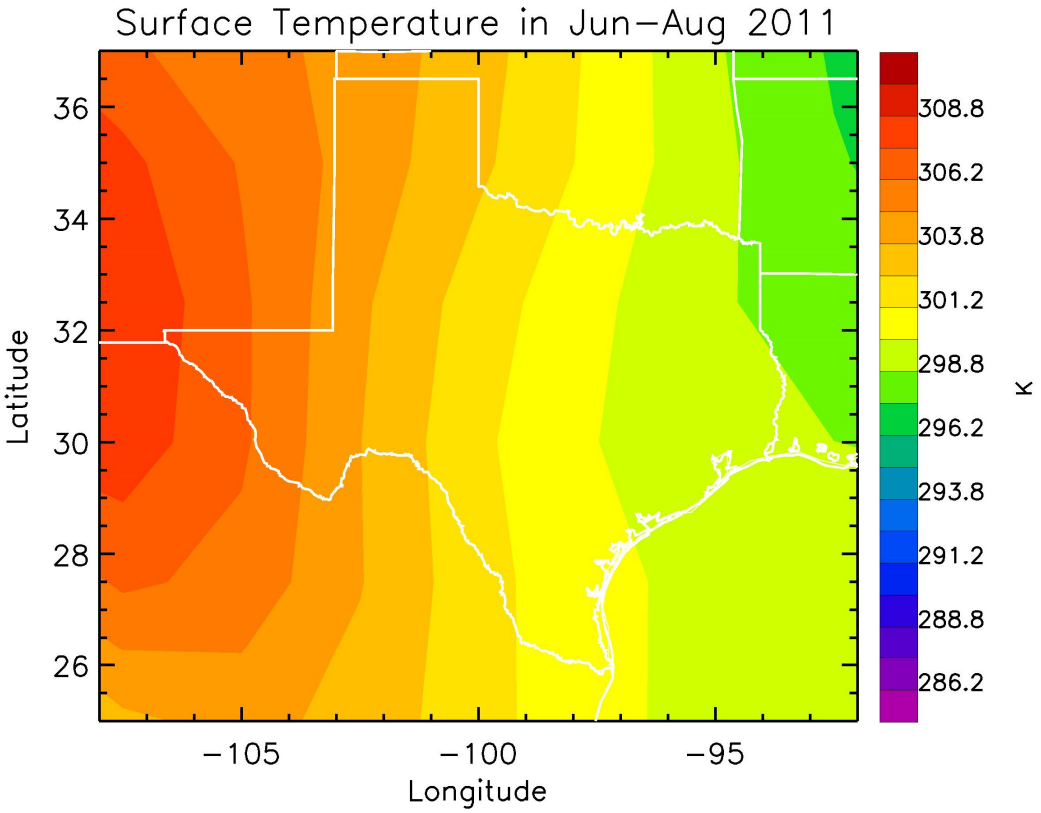

Figure 2.9. NCEP2 monthly mean surface temperature in June-August 2011 over the state of Texas. Units are Kelvin.

Figure 2.9 demonstrates the monthly mean surface temperature in June-August 2011 from derived NCEP2 reanalysis data over the state of Texas. Here, abnormally warmer than normal surface temperatures are shown when compared to the climatology. For convenience, we calculate the difference between the June-August 2011 temperature and climatology in Figure 2.10. The difference is calculated by subtracting the climatology from the June-August 2011 temperature. The spatial difference is shown for the state of Texas, revealing the deviation from average. This can be accounted for by the aforementioned decrease in precipitation and soil moisture, with less associated evaporation, supplying an abundance of solar energy for sensible heating of the atmosphere.

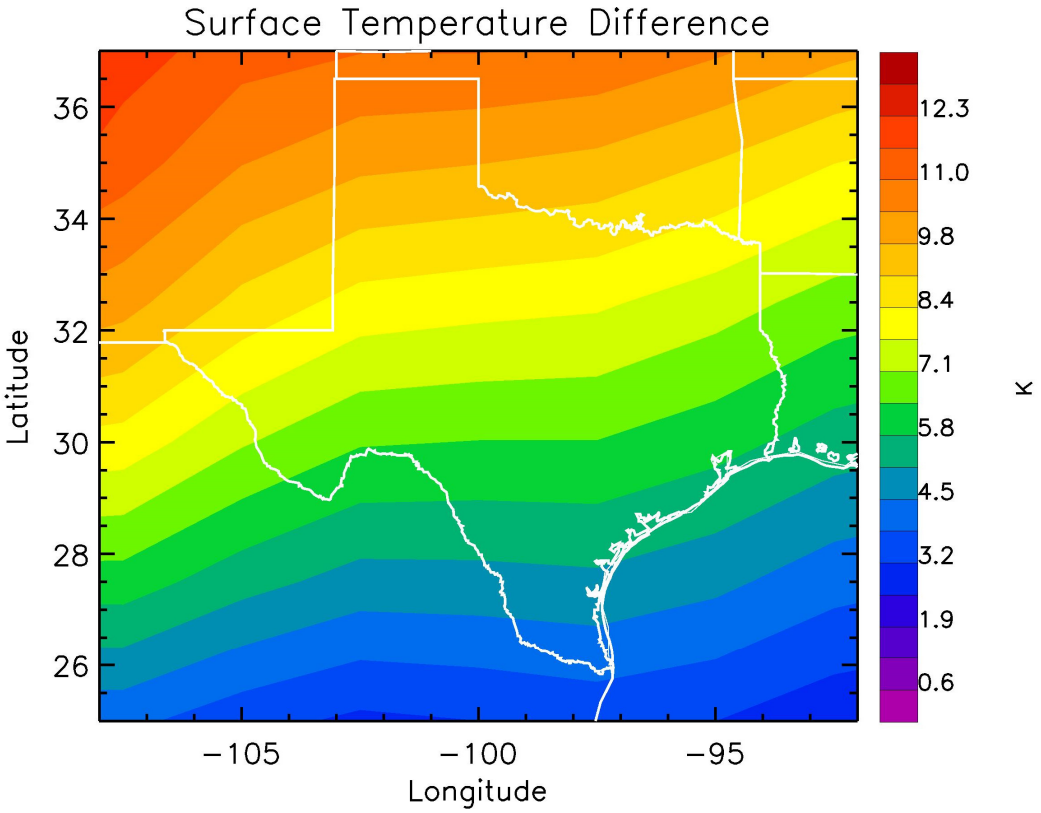

Figure 2.10. NCEP2 monthly mean surface temperature difference between the summer of 2011 and climatology. Units are Kelvin.

Table 2.5 gives observations noted all across the state of Texas for the entire 2011 year. It illustrates the average temperature in degrees Fahrenheit and shows the observational sites hottest year on record. For comparison is 2011's average temperature along with how it ranked with the previous years. Highlighted in bold, we see those sites in which 2011 was within the top three hottest years on record. Of the sites listed in the table, 14 out of 18 had one of their top three hottest years ever. Temperature station data are available online[6] from the National Climatic Data Center.

TABLE 2.5. Temperature observations for multiple locations in the state of Texas for 2011. Those highlighted in bold represent the sites where their 2011 rank was in the top three hottest years on record. For comparison, the previous hottest temperature and year are shown.

Location	Average Temperature (°F)	
	2011 (Rank)	Record Highest (Year)
Abilene, TX	***67.5 (2nd)***	67.6 (1933)
Amarillo, TX	59.7 (7th)	61.5 (1934)
Austin, TX	***72.0 (1st)***	71.6 (2006)
Beaumont, TX	***70.7 (2nd)***	71.3 (1946)
Brownsville, TX	***76.1 (1st)***	76.0 (2006)
College Station, TX	***71.7 (1st)***	70.3 (2006)
Corpus Christi, TX	73.5 (5th)	74.2 (2006)
Dallas/Fort Worth, TX	***68.6 (3rd)***	69.4 (2006)
El Paso, TX	***66.7 (3rd)***	67.4 (1994)
Houston, TX	***71.8 (2nd)***	71.9 (1962)
Midland, TX	***66.7 (1st)***	66.4 (1998)
Lubbock, TX	***62.9 (2nd)***	63.3 (1934)
Lufkin, TX	***69.0 (2nd)***	69.1 (1998)
San Angelo, TX	***69.2 (1st)***	67.7 (2000)
San Antonio, TX	***71.8 (3rd)***	72.1 (1933, 2006)
Victoria, TX	***72.6 (3rd)***	73.7 (1933)
Waco, TX	69.6 (6th)	71.0 (1933)
Wichita Falls, TX	66.6 (6th)	67.8 (1933)

[6] Available at: http://www.ncdc.noaa.gov

By May 2014, KBDI values somewhat recovered from those in 2011, although areas in central and north Texas continued to suffer. KBDI values, ranging from 0 (saturated) to 800 (void of soil moisture to 8 inches deep), averaged 300-400 across much of the southeast Texas region. Jackson County reported values of 500-600 with a few locations showing 600-700 in the northwest areas. Portions of western Brazoria County and southern Montgomery County also illustrated higher values than the remainder of the region.

To better understand the possible relationship between precipitation and sea surface temperature, mean precipitation data from TRMM (V007 3A12) and sea surface temperature data from NCEP2 were calculated over Texas from January 1999 to May 2013. Detrended and deseasonalized precipitation and surface temperature are shown in Figure 2.11a, in which linear trends and annual cycles calculated from the monthly mean data, were removed. Detrended precipitation averaged over Texas is shown as the black solid line with the detrended and inversed surface temperature overlain as the blue dashed line. To further explore the relationship between precipitation and temperature, a lowpass filter is applied to remove the high frequency signals from both time series, thus eliminating large biases in the trend due to significant interannual variability. The filter is constructed as the convolution of a step function with a Hanning window and chosen to obtain a full signal from periods above 15 months and no signal from periods below 12.5 months. Lowpass filtered Texas precipitation (black solid line) are plotted against lowpass filtered and inversed surface temperature (blue dashed line) and lowpass filtered and inversed Southern Oscillation Index (SOI) (red dotted line) in Figure 2.11b. The correlation coefficient between the lowpass filtered precipitation and lowpass filtered and

inversed surface temperature is 0.5. This correlation between precipitation and surface temperature suggests that high temperature is related to drought over Texas.

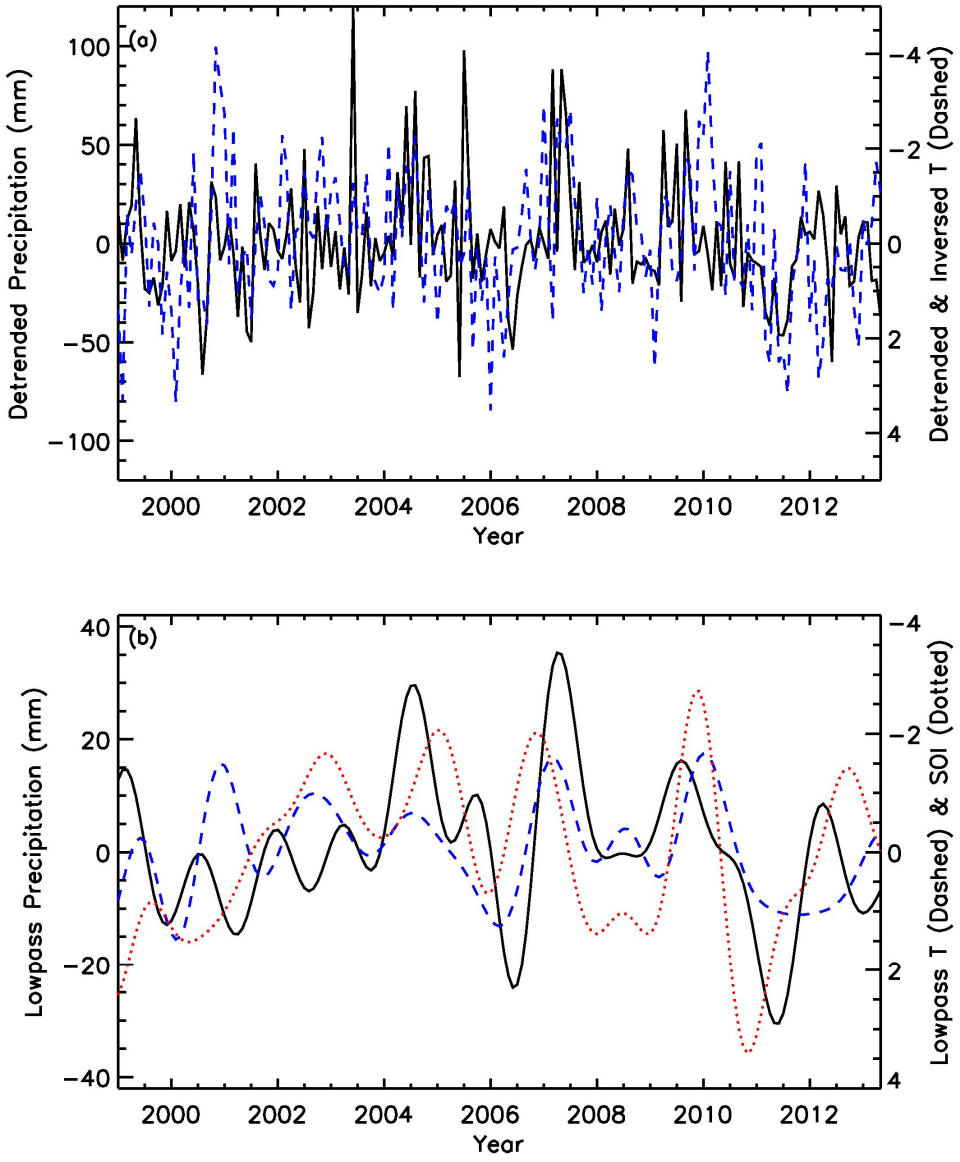

Figure 2.11. (a) Detrended and deseasonalized TRMM precipitation (black solid line) and detrended and inversed NCEP2 temperature (blue dashed line) averaged over Texas from Jan 1999 to May 2013. (b) Lowpass filtered precipitation (black solid line) and lowpass filtered & inversed SOI (red dotted line) and temperature (blue dashed line). A 15 month lowpass filter was applied to the time series to remove the high frequency signals.

To better explore the influence of La Niña episodes on drought over Texas, we evaluate omega during the La Niña event of 2011. Results of omega during the drought year are compared with those from average years.

Omega is defined as the vertical change in pressure with time and is used to describe the magnitude of vertical motion (Hoskins *et al*., 1978). Since pressure in the Earth's atmosphere decreases with height from the surface, positive values of omega exhibit sinking vertical motion while negative values indicate rising motion. To better understand where convection and thunderstorm development might occur, we plot omega over the state of Texas. Shown in Figure 2.12 is the monthly mean 500 mb omega climatology derived from NCEP2 reanalysis data in units of Pascal/day. The spatial climatology pattern reveals all positive values of omega for the state with the highest values in the panhandle and central/west Texas, indicating greater sinking air in those regions. This greater subsidence, coupled with the lack of atmospheric moisture, confirms the precipitation observations and the desert-like environments notorious in these areas.

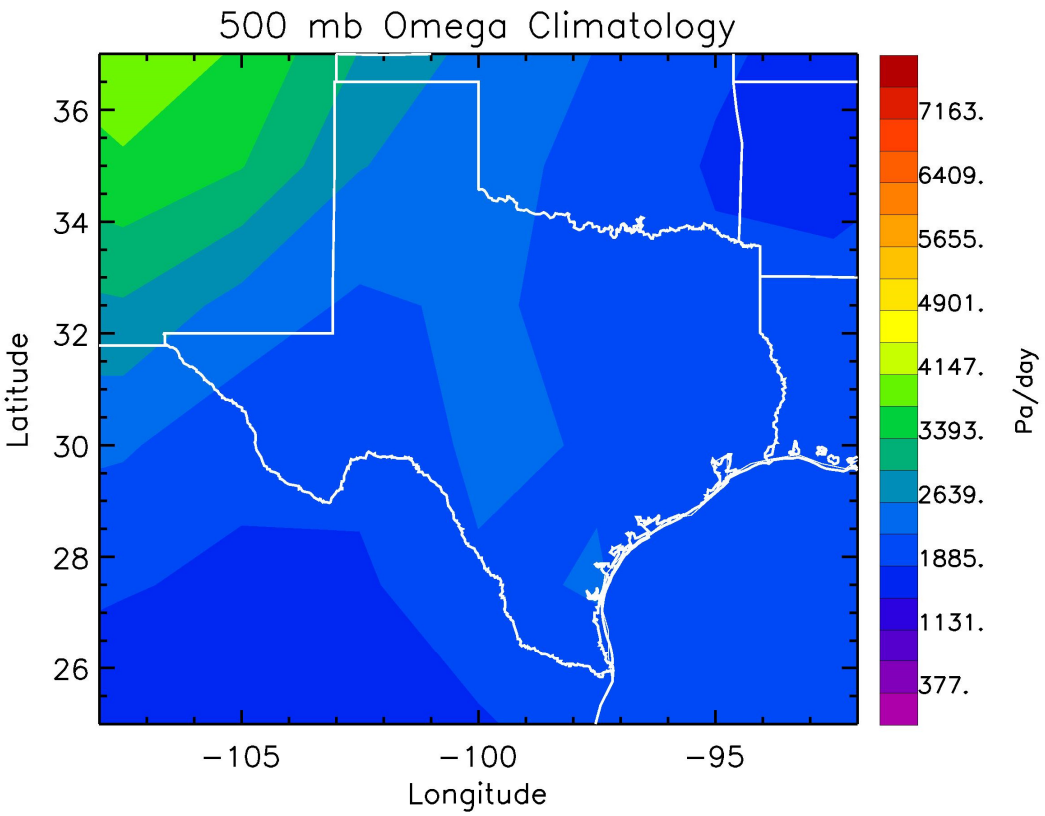

Figure 2.12. NCEP2 monthly mean 500 mb omega climatology from Jan 1999 to May 2013. Units are Pa/day.

Next, we calculate omega for the June–August 2011 time frame. Figure 2.13 displays the monthly mean 500 mb omega from NCEP2 reanalysis data given in Pascal/day. Illustrated here are higher values of omega in most of the state with a decrease toward both the east/southeast and west ends.

With these conditions apparent in 2011, vegetation across the state suffered and fire weather incidents increased. Toward the end of 2011, totals indicated almost 3.9 million acres had burned across the state of Texas. A total of 4,956 structures had been lost with 47,891 structures threatened but saved. Fire weather concerns increased as the first killing freezes of 2011 affected the area, resulting in a heavier fuel loading of finer

fuels. The larger ladder and canopy fuels remained extremely dry; and once finer fuels were cured for the winter season, wildfires would persist. Additionally, the threat for wind driven wildfires was significant across the state with critical days occurring during the passage of typical fall season cold fronts.

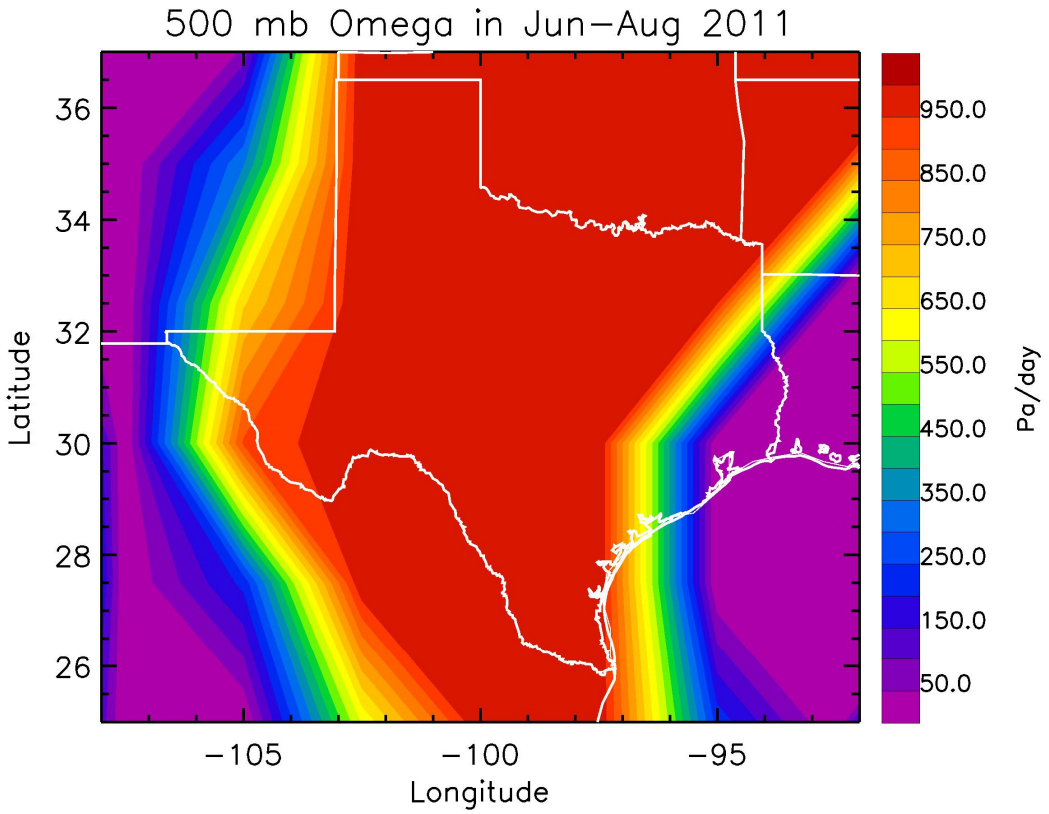

Figure 2.13. NCEP2 monthly mean 500 mb omega for June-August 2011. Units are Pa/day.

Vegetative health is a precursor to the fuel loading that affects the development of wildfires. During 2011, trees continued to suffer across the entire state as rainfall remained below average and temperatures rose. Drought stress led to the invasion of harmful disease and pests that attack and kill weakened trees. Many went dormant in late

summer 2011, due to lack of water aiding to shed leaves. Pine and Water Oak trees took the hardest hit with estimates of at least 2-3 million dying in Harris County and the immediate surrounding counties, with an additional 66-80 million dying in the following years. Native trees such as Cedar and Juniper displayed signs of drought stress and in the Waco/Temple corridor died from lack of water.

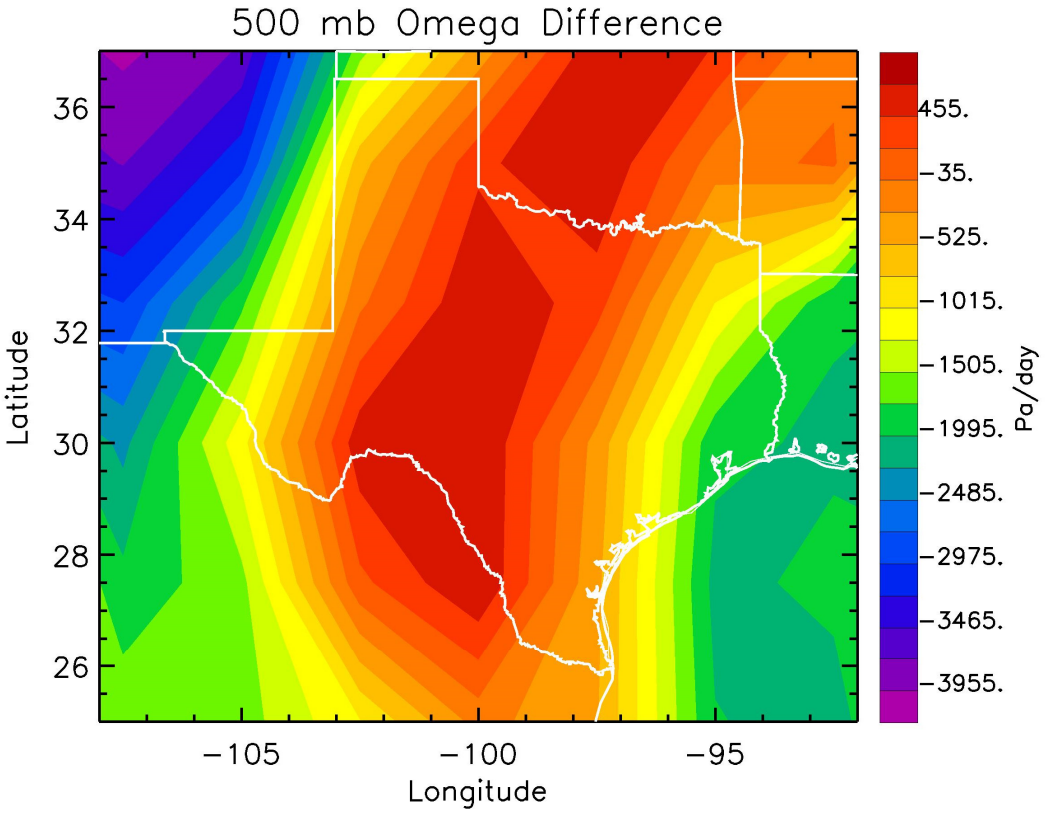

Figure 2.14. NCEP2 monthly mean 500 mb omega difference between the summer of 2011 and climatology. Units are Pa/day.

To investigate anomalies in La Niña years, we calculate the difference between the June-August 2011 omega and climatology in Figure 2.14. It is calculated by subtracting the climatology from the June-August 2011 omega at the 500 mb pressure

level. Shown for approximately half of the state, specifically portions of north, central, and south Texas, omega is more positive than normal, resulting in increased sinking motion during 2011. This supplies an explanation for the decrease in precipitation and can help account for the drought conditions experienced in that year. Moreover, portions of east and west Texas exhibit values of omega less positive than average, showing a slight decrease in sinking motion for those regions.

Fire weather conditions as of May 2014 have shown some improvement since 2011, although very dry air masses, regional lack of rainfall, and warming temperatures caused a significant decline in fine fuels, making wildfire ignition more probable. Large and canopy fuels remain in good condition while ladder fuels become increasingly dry, thus amplifying the potential for large and hot wild land fires. One hundred-hour fuels across much of the north/central region are classified as critically dry and ten-hour fuels contain very minimal moisture, making conditions increasingly dire across central and west Texas where the potential for fast moving, wind driven wildfires is extreme. As of May 2014, eighty six Texas counties have burn bans in effect for these areas, due to 67 wildfires having burned over 16,000 acres.

Vegetative health as of May 2014 has recently declined due to the severe lack of moisture over most of the state. Spring crops had just enough moisture to germinate but are showing signs of wilting with approximately half the expected heights for this time of year. Soil moisture losses have been the greatest in and around the City of Victoria where deficits are averaging between -80 mm to -100 mm.

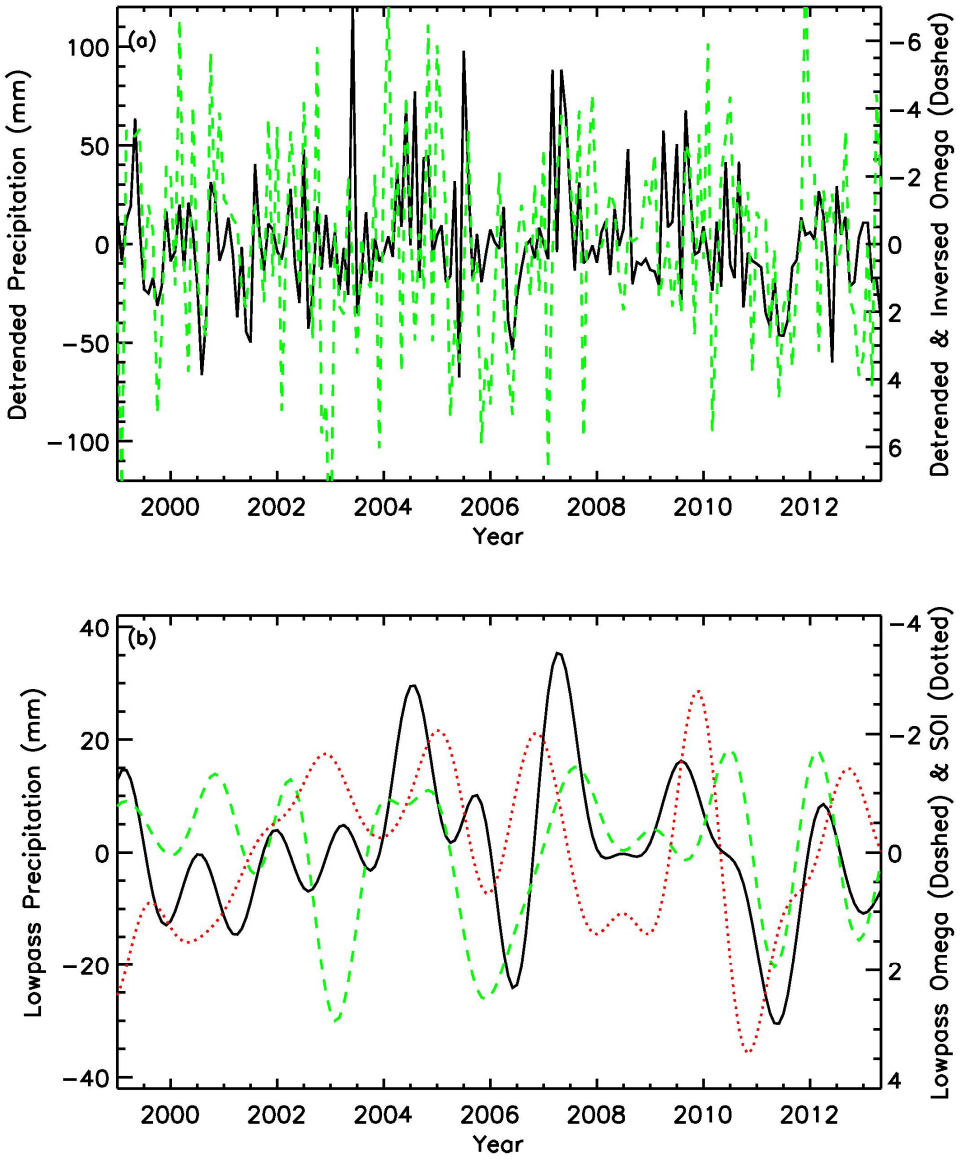

Figure 2.15. (a) Detrended and deseasonalized TRMM precipitation (black solid line) and detrended and inversed NCEP2 omega (green dashed line) averaged over Texas from Jan 1999 to May 2013. (b) Lowpass filtered precipitation (black solid line) and lowpass filtered & inversed SOI (red dotted line) and omega (green dashed line). A 15 month lowpass filter was applied to the time series to remove the high frequency signals.

To further explore the possible relationship between precipitation and omega, mean precipitation data from TRMM and omega data from NCEP2 were calculated over

Texas from January 1999 to May 2013. Detrended and deseasonalized precipitation and omega are shown in Figure 2.15a, in which linear trends and annual cycles, calculated from the monthly mean data, were removed. Detrended precipitation averaged over Texas is shown as the black solid line with the detrended and inversed omega overlain as the green dashed line. To examine the relationship between precipitation and omega further, a lowpass filter is applied to remove the high frequency signals from both time series. Lowpass filtered Texas precipitation (black solid line) are plotted against lowpass filtered and inversed omega (green dashed line) and lowpass filtered and inversed Southern Oscillation Index (SOI) (red dotted line) in Figure 2.15b. The correlation coefficient between the lowpass filtered precipitation and lowpass filtered and inversed omega was found to be 0.41. This correlation between precipitation and omega suggests that omega is related to the rainfall experienced within a region by the increased sinking motion and atmospheric stability, thus helping to limit thunderstorm development. This relationship supplies another approach in examining the temporal and spatial variability of precipitation.

In summary, the economic impacts of the historic drought of 2011 resulted in $5.2 billion in losses accumulated, mainly in the agriculture arena. This accumulation in losses surpassed the $4.1 billion record of 2006. During 2011, the Texas pecan harvest decreased by 20 million pounds compared to the typical crop. A massive red tide bloom affected much of the Texas Gulf Coast and closed the oyster harvesting season, partially due to the lack of fresh water runoff from inland rivers reaching the bays. In fact, many of the Texas bay systems experienced hypersaline water conditions due to lack of freshwater runoff. Wheat crop yields were down about 800,000 acres, and corn suffered

heavily as its yield decreased 40%. Sorghum crop yield diminished 50% and a staggering 52% of the cotton crop was abandoned in 2011, adding about $1.8 billion in losses.

Across Texas, grass that had long since died during the hot summer months resulted in casualties of cattle and wildlife. Truckloads of hay were brought into Texas to supplement the declining supplies of feed. It is estimated that 10,000 head of cattle were relocated to other areas of the country to sustain their needs. A combination of severely reduced feed and lowering water supplies had a tremendous effect on the ability of cattle to survive, thus complicating the situation and adding millions in losses. All data concerning vegetation, fire weather, and economic impacts are available online[7].

[7] Available at: http://www.fs.usda.gov/texas/ and http://texasforestservice.tamu.edu/main/default.aspx

2.4 PCA Analysis of TRMM Precipitation over Texas

To better understand the temporal variation and spatial pattern of precipitation, we utilize a statistical tool named Principal Component Analysis (PCA), which has already been used in a previous study (Jiang *et al*., 2008) to analyze the temporal and spatial variability of precipitation.

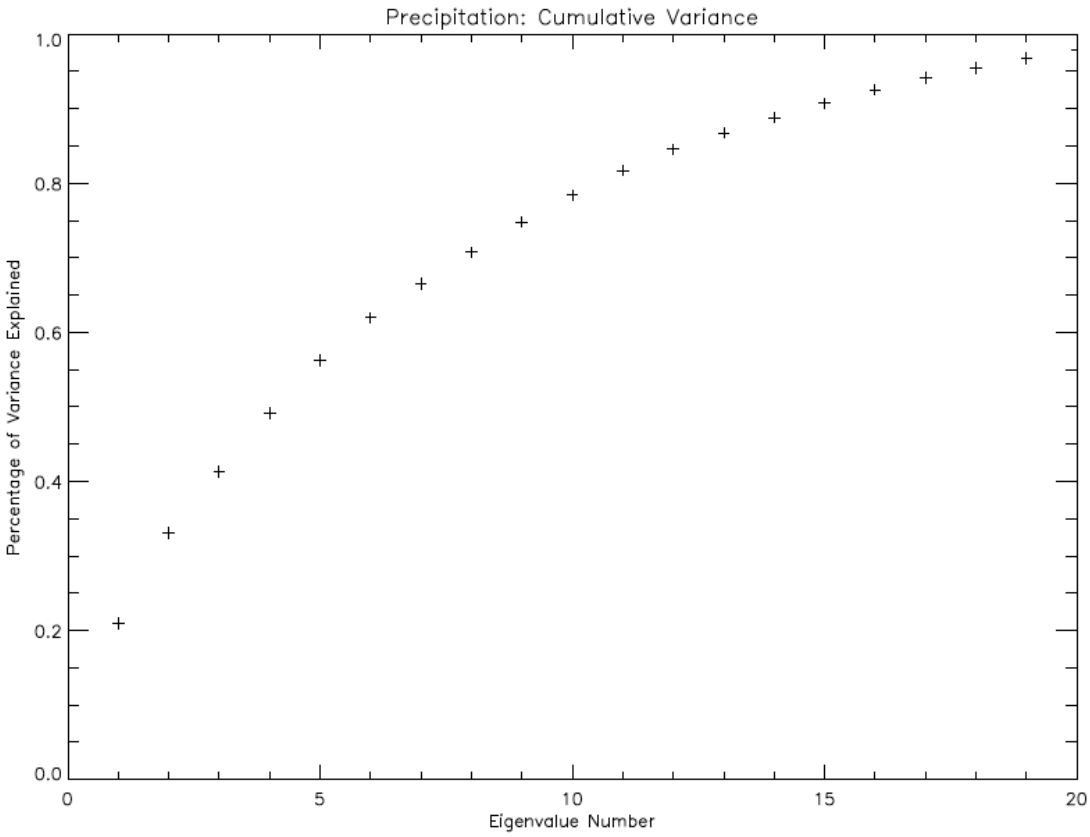

Figure 2.16. Cumulative variance for TRMM precipitation data over Texas. X-axis displays the Eigenvalue numbers with their subsequent percentage of variance explained illustrated along Y-axis.

PCA provides a decomposition of a multivariate dataset into orthogonal functions, known as empirical orthogonal functions (EOFs), with associated time-dependent

amplitude, known as principal component (PC) time series. The EOFs are the Eigenfunctions of the covariance matrix of the dataset sorted by the decreasing values of associated Eigenvalues. Since these Eigenvalues represent the variance captured by each EOF, PCA guarantees that the leading *n* EOFs capture more of the total variance of the dataset than any other *n* orthogonal vectors. By applying PCA to precipitation, we can decompose the data to different modes, thus enabling a more thorough investigation of its spatial pattern and temporal variability.

We use the PCA method to analyze the TRMM precipitation results in the Texas region. Figure 2.16 illustrates the cumulative variance in the TRMM precipitation data. Displayed are the Eigenvalue numbers from the analysis and their subsequent percentage of variance explained. The leading mode of the PCA captures 21% of the total variance in precipitation over Texas, respectively. Illustrated in Figure 2.17a are the spatial variability of the leading mode (EOF1) and its associated contribution of precipitation. The spatial pattern demonstrates the leading mode has minimal effect on the panhandle and west Texas areas and the greatest effect on south, central, and southeast Texas.

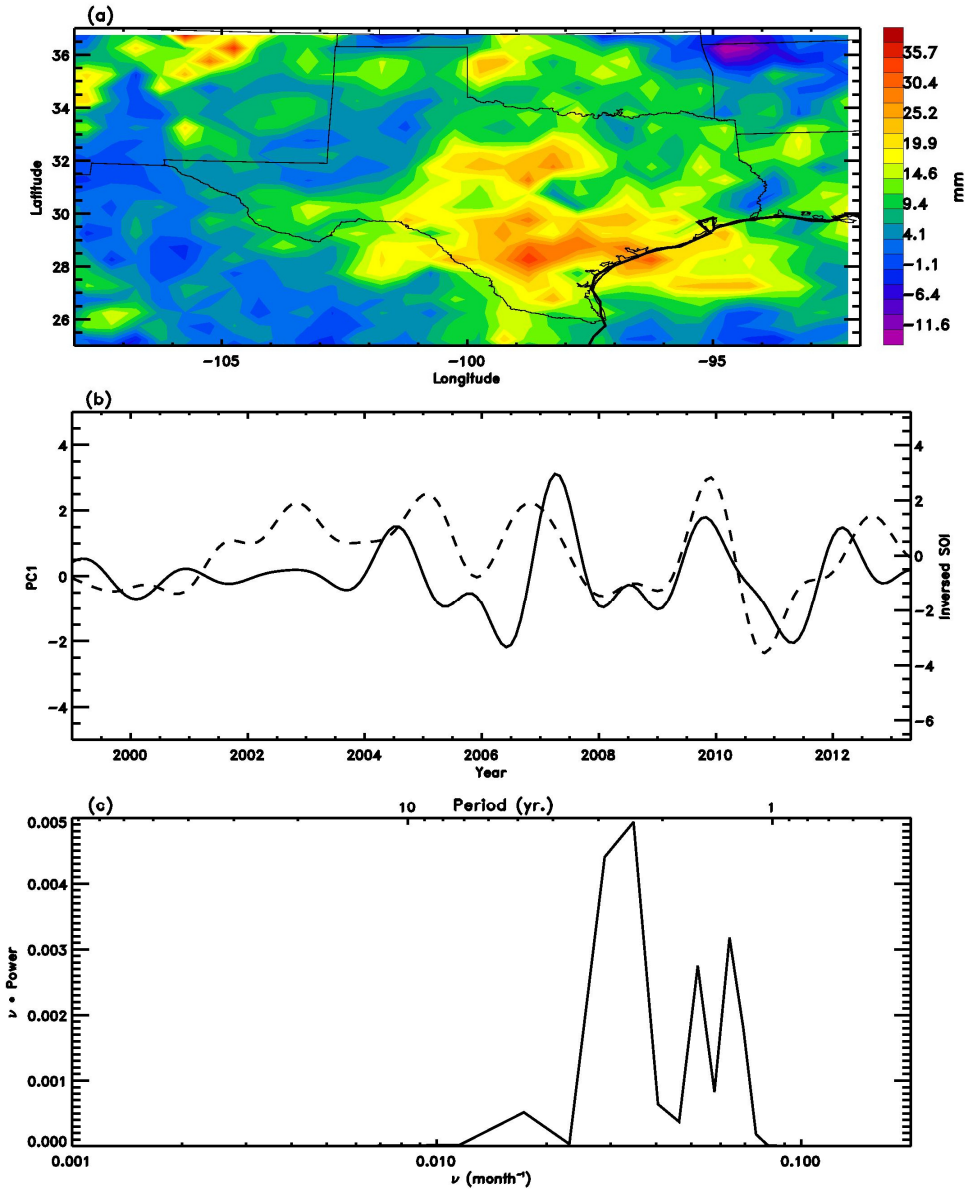

Figure 2.17. (a) Spatial pattern of TRMM precipitation anomalies over Texas from the PCA leading mode (EOF1). Units are mm/month. (b) Southern Oscillation Index (dashed line) and leading PC time series (solid line). A lowpass filter was applied to the inversed and detrended SOI. (c) Power spectrum of the PC1 leading mode displayed in frequency and year.

The Southern Oscillation Index (SOI) is used to calculate the correlations between ENSO and leading PC time series, shown in Figure 2.17b. For a fair comparison, we

applied a lowpass filter and inversed the detrended SOI. Comparison of the time series of the detrended and lowpass filtered SOI and the first mode (PC1) of the TRMM precipitation reveals a moderate correlation. The correlation between the two time series is 0.42, suggesting the greatest variance in precipitation over Texas is related to the phase and cycle of ENSO. Likewise, the power spectrum of the PC1 mode, shown in Figure 2.17c, demonstrates strongest spectral peaks at 2-5 years, which are the dominant peaks in ENSO.

2.5 Conclusions

The anomalies between La Niña and normal years for TRMM precipitation show an extreme deviation from normal with below average rainfall for the majority of the state during 2011 with the exception of a few small areas in northeast and south/central Texas, illustrating above average rainfall. The findings show the maximum cross correlation coefficient between TRMM precipitation and Southern Oscillation Index (SOI) was 0.5 when the lag is 5 months, suggesting that decreasing rainfall over Texas may appear five months after a period of increasing SOI, providing a possible forecasting factor for drought over Texas.

Secondly, the relationship between precipitation and surface temperature was examined. The correlation between TRMM precipitation and surface temperature suggests that high temperature is related to drought over Texas. Previous analysis of global temperature and water vapor profiles suggest variations of gross moist stability of the atmospheric boundary layer and the related adjusting of convection and precipitation

(Held and Soden, 2006; Chou *et al*., 2009). It is understood that a warmer atmosphere has the potential to contain increased water vapor, reducing the gross moist stability of the atmospheric boundary layer; and hence the convection and the related precipitation is amplified in the wet areas (Chou and Neelin, 2004; Chou *et al*., 2009). Furthermore, a previous study shows the recycling rate displays a strong negative temporal variation in the dry areas and a positive temporal variation in the wet areas, implying the rate of water vapor in the global atmosphere is increasing more rapidly than the rate of precipitation (Li *et al*., 2011). With increased water vapor contained in the atmosphere, a reduced temperature gradient exists between the surface and the atmosphere aloft, increasing the overall stability and implying a condition less conducive to produce precipitation. In the Texas case, it is further complicated by influences from the tropical Pacific Ocean and mesoscale meteorological phenomena such as the land/sea breeze interaction with the Gulf of Mexico.

To further explain the temporal variability of precipitation over Texas, we explored the relationship between 500 mb omega and rainfall during 2011. For approximately half of the state of Texas, specifically portions of north, central, and south Texas, omega was found to be more positive than normal during the summer of 2011, resulting in increased sinking motion, limiting convection and thunderstorm development. This supplies an explanation for the decrease in precipitation and can help account for the drought conditions experienced in that year. Subsequently, portions of east and west Texas exhibit values of omega less positive than normal, showing a slight decrease in sinking motion for those regions. The time series for TRMM precipitation and omega suggests they are related by the enhanced sinking motion and increased

atmospheric stability. This relationship supplies another approach in examining the temporal and spatial variability of precipitation.

The leading mode (EOF1) of the TRMM PCA captured 21% of the total variance in precipitation over Texas. The spatial variability of EOF1 revealed minimal effect on the panhandle and west Texas and the greatest effect on south, central, and southeast portions of the state. The correlation between PC1 and SOI suggests the greatest variance in the TRMM data is related to the phase and cycle of ENSO. Additionally, the power spectrum of the PC1 mode is calculated and compared with that of the frequency of ENSO events. The PC1 mode demonstrated its strongest spectral peaks near 2-5 years, similar to that in more recent ENSO cycles.

2.6 Acknowledgments

I especially acknowledge Jeff Lindner, who supplied valuable information concerning the case study over Texas.

Chapter 3

Temporal and Spatial Variability of Precipitation over Tropical Regions from Observation and Model

3.1 Introduction

Precipitation can be influenced by different factors such as atmospheric temperature, circulation, and clouds (Trenberth and Shea, 2005; Adler *et al*., 2008; Allan and Soden, 2008; Liu *et al*., 2009; Li *et al*., 2011; Bony *et al*., 2013). As a response to global warming, it is found that global mean precipitation is increasing with a slower trend than the total mass of water vapor (Allen and Ingram, 2002; Adler *et al*., 2003; Held and Soden, 2006; Gu *et al*., 2007; Adler *et al*., 2008; Stephens and Ellis, 2008; Li *et al*., 2011). In addition to the global mean precipitation, some studies (Chou and Neelin, 2004; Allan and Soden, 2007; Chou *et al*., 2009; Li *et al*., 2011; Durack *et al*., 2012; Polson *et al*., 2013; Chou *et al*., 2013; Trammell *et al*., 2015) explored precipitation variations over different regions and found that precipitation has an increasing tendency in wet areas and a decreasing tendency in dry areas. In addition to the external forcing, changes in the precipitation can also be attributed to natural climate variability (Gu and Adler, 2012; Marvel and Bonfils, 2013). In this chapter, we explore the variability of precipitation over tropical regions from observation and model, using a statistical tool called Principal Component Analysis.

3.2 Model

In addition to the GPCP precipitation dataset previously introduced, the simulation output from the National Center for Atmospheric Research (NCAR) Community Atmosphere Model (CAM5) for the period of 1979-2010 is used in this chapter. CAM5 is the atmospheric component of the Community Earth System Model, version 1 (CESM1). In the CAM5, the radiation scheme uses the Rapid Radiative Transfer Method for GCMs (RRTMG) (Iacono *et al*., 2008). The moist boundary layer is parameterized using the Park and Bretherton (2009) scheme, and the large-scale cloud and precipitation processes are parameterized with a prognostic two-moment bulk cloud microphysics scheme (Morrison and Gettelman, 2008). Shallow convection is parameterized using Park and Bretherton (2009), and deep convection is parameterized using the Zhang and McFarlane (1995) convection scheme with a dilution approximation for the calculation of convective available potential energy (Neale *et al*., 2008). The CAM5 simulation incorporates observed sea surface temperature as lower boundary conditions with a horizontal resolution of 2.5º × 1.9º (latitude by longitude).

3.3 Principal Component Analysis

The specific goal of this chapter includes the examination of the temporal and spatial variability of precipitation via a statistical tool called Principal Component Analysis (PCA). The research aims to answer questions such as follows:

1. What are the temporal and spatial variability of precipitation over tropics?

2. What is the dominant variability of tropical precipitation that explains the maximum amount of variance in the data?

3. How will the model simulate the variability of tropical precipitation?

In the next section, we focus on investigating the spatial and temporal variability of GPCP precipitation for the tropical domain.

3.3.1 GPCP Precipitation at Tropics

To explore the temporal and spatial variability of precipitation, a statistical tool called Principal Component Analysis (PCA) (Richman, 1986; Preisendorfer, 1988; Thompson and Wallace, 2000; Camp *et al*., 2003; Jiang *et al*., 2008a; Jiang *et al*., 2008b) is applied to the detrended, deseasonalized, and lowpass filtered precipitation data from GPCP and CAM5 model from 1979-2010. A linear trend is applied to the time series. Seasonal cycles for each time series are removed, and a lowpass filter is applied to the precipitation anomaly to remove the high frequency oscillation. The filter is constructed as the convolution of a step function with a Hanning window and chosen to obtain a full signal from periods above 15 months and no signal from periods below 12.5 months (Jiang *et al*., 2004).

PCA provides a decomposition of a multivariate dataset into orthogonal functions, known as empirical orthogonal functions (EOFs), with associated time-dependent amplitude, known as principal component (PC) time series. The EOFs are the Eigenfunctions of the covariance matrix of the dataset sorted by the decreasing values of associated Eigenvalues. All Eigenvectors of a matrix are orthogonal, regardless of the

number of dimensions. Since these Eigenvalues represent the variance captured by each EOF, PCA guarantees that the leading *n* EOFs capture more of the total variance of the dataset than any other *n* orthogonal vectors. However, PCA is not a scale-independent method. Therefore, it is necessary to weight each element of the covariance matrix by the area it represents; i.e., scale each time series by square root of area, $\sqrt{\cos\theta}$ (where θ is the latitude), prior to constructing the covariance matrix (Baldwin *et al*., 2007). Eigenfunctions of the covariance matrix of the dataset are the EOFs with associated time-dependent amplitude PC time series. In order to recover the spatial patterns for the original (unscaled) precipitation anomaly, we perform a multiple linear regression for each grid point, using as predictors the PC time series. The resulting linear regression coefficients are the spatial patterns of the precipitation variability associated with the i^{th} PC time series.

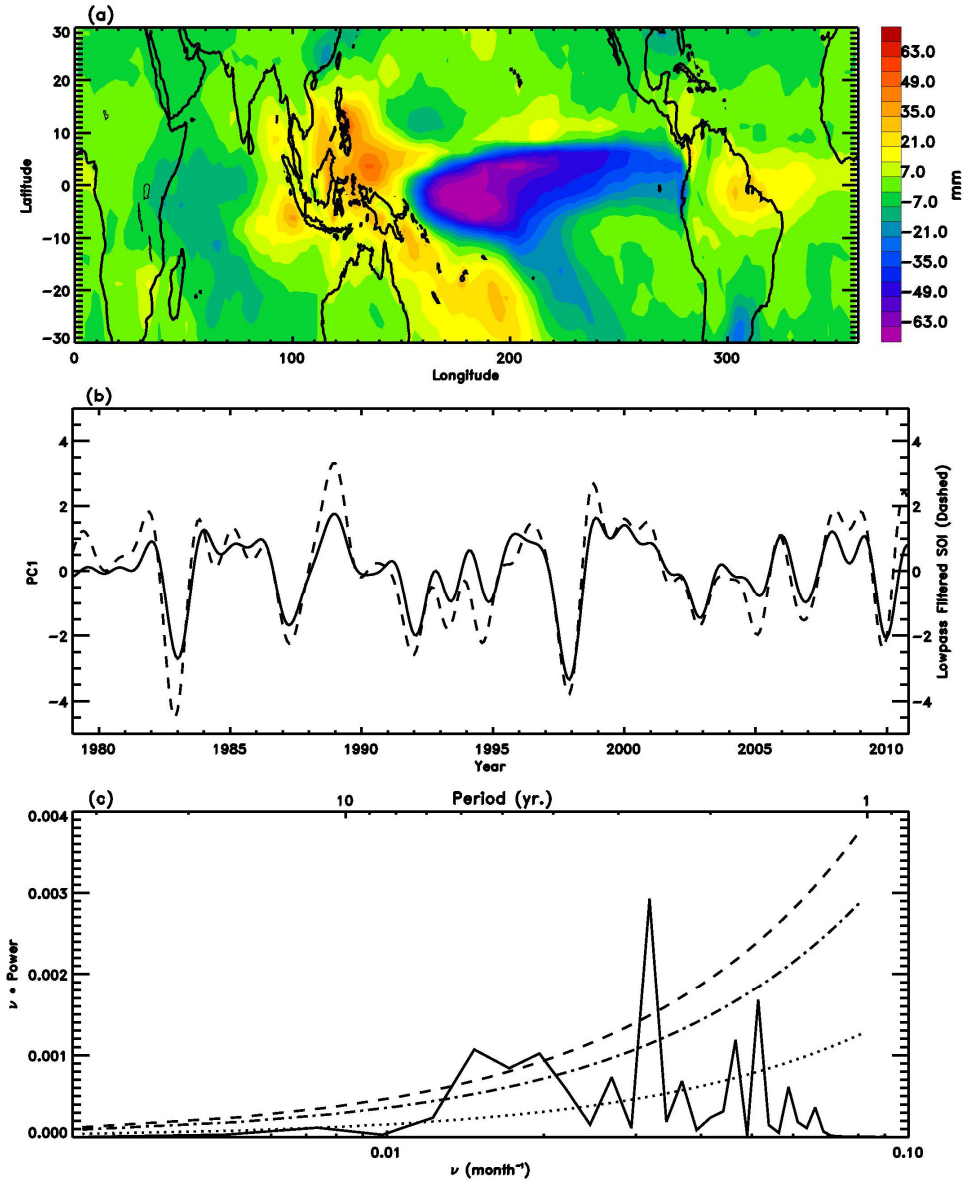

Figure 3.1. (a) The spatial pattern of the first mode of GPCP precipitation anomalies in the tropics. Units are mm. (b) PC1 of the tropical GPCP precipitation (solid line) and Southern Oscillation Index (dashed line). The correlation coefficient is 0.90 (0.1% significance level). (c) Power spectral estimate of the PC1 (Solid), red noise spectrum (Dotted), 90% and 95% confidence interval (Dashed). The first mode explains 31.9% of the total variance.

PCA is utilized to analyze interannual variability of the GPCP precipitation in the tropics (30°N-30°S). The first leading mode accounts for 31.9% of the total variance of GPCP tropical precipitation. The spatial pattern of the precipitation anomalies regressed on the first PC is shown in Figure 3.1a. There are positive precipitation anomalies over western Pacific and negative anomalies over central and eastern Pacific. Values range from 60 mm in the western Pacific and -60 mm over central and eastern Pacific. The spatial pattern is similar with a recent study between GPCP rainfall anomalies and Niño3 Index (Ashok *et al*., 2007). The Southern Oscillation Index (SOI) is used to calculate the correlation between ENSO and PC1, shown in Figure 3.1b. For a fair comparison, a lowpass filter is applied to the detrended SOI. Comparison of the time series of the detrended and lowpass filtered SOI and the first mode (PC1) of the GPCP tropical precipitation reveals a good correlation. The correlation between the two time series is 0.90. The corresponding significance level is 0.1%. The significance statistics for correlations were generated by a Monte Carlo method (Press *et al*., 1992; Jiang *et al*., 2004). Positive SOI represents La Niña months, in which there are positive precipitation anomalies over western Pacific and negative precipitation anomalies over central and eastern Pacific. Negative SOI represents El Niño months, in which there are negative precipitation anomalies over western Pacific and positive precipitation anomalies over central and eastern Pacific. We also applied the power spectral analysis to PC1. The power spectrum of the PC1, shown in Figure 3.1c, demonstrates strong spectral peaks near 2-7 years, similar to those in ENSO.

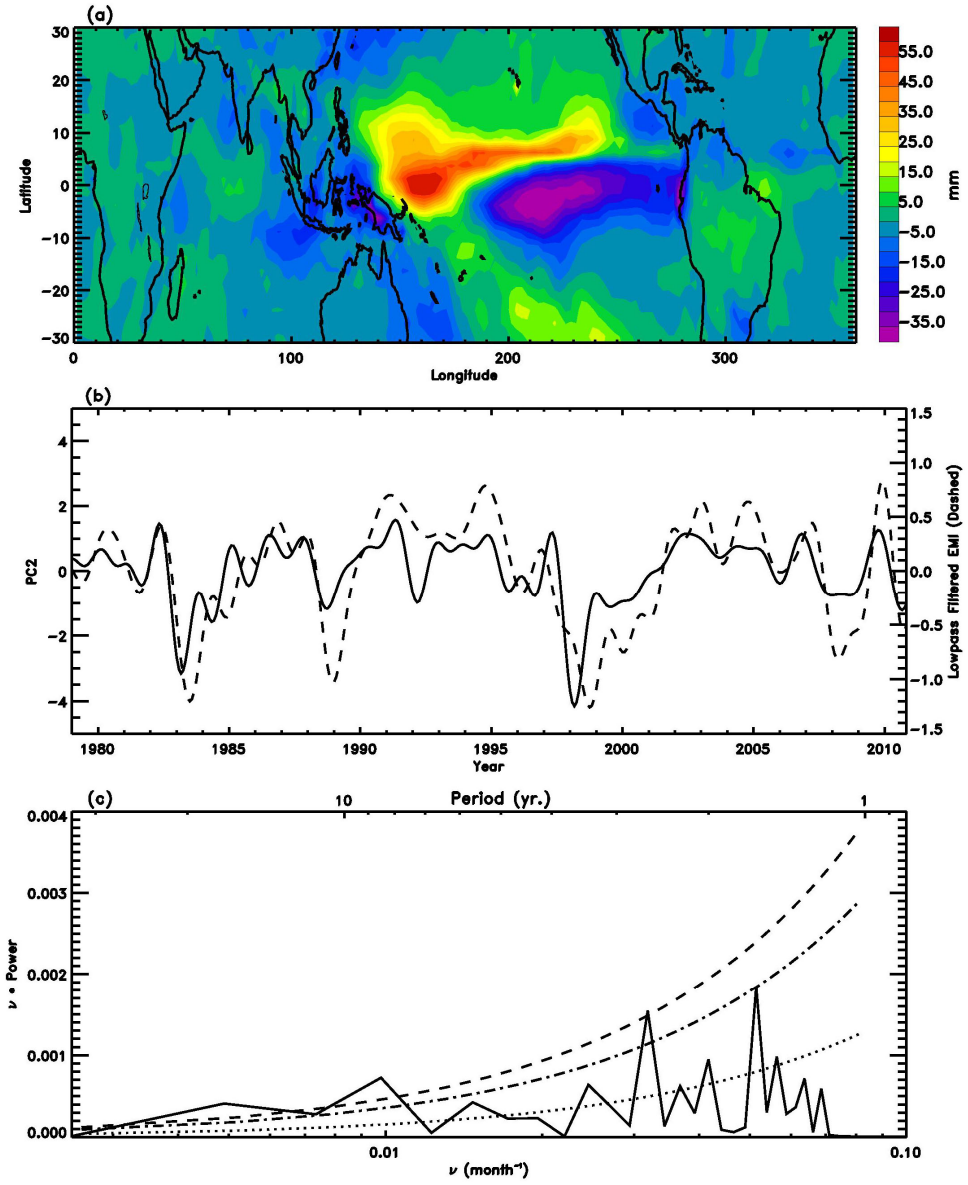

Figure 3.2. (a) The spatial pattern of the second mode of GPCP precipitation anomalies in the tropics. Units are mm. (b) PC2 of the tropical GPCP precipitation (solid line) and inverted El Niño Modoki Index (EMI) (dashed line). The correlation coefficient is 0.75 (0.1% significance level). (c) Power spectral estimate of PC2 (Solid), red noise spectrum (Dotted), 90% and 95% confidence interval (Dashed). The second mode explains 15.6% of the total variance.

The statistical significance of signals in a power spectrum is obtained by comparing the amplitude of a spectral peak to the red noise spectrum (Gilman *et al*., 1963). The 90% and 95% confidence intervals for the power spectrum are found using *F*-statistics to compare the spectrum to the red noise spectrum (Jiang *et al*., 2008a).

The second leading mode accounts for 15.6% of the total variance of GPCP tropical precipitation. Illustrated in Figure 3.2a is the spatial pattern of the precipitation anomalies regressed on the second PC of GPCP tropical precipitation. There are positive precipitation anomalies over central Pacific and negative precipitation anomalies over western and eastern Pacific. Values range from 60 mm in the central Pacific to -40 mm over western and eastern Pacific. The El Niño Modoki Index (EMI) is used to calculate the correlation between the phenomenon known as El Niño Modoki and the second PC time series, shown in Figure 3.2b. EMI is defined as area-averaged Sea Surface Temperature Anomaly (SSTA) difference between central tropical Pacific SSTA and the average of western and eastern tropical Pacific SSTA (Ashok *et al*., 2007). We have applied a lowpass filter to the detrended EMI time series. The correlation coefficient between the detrended and lowpass filtered EMI and the PC2 of the GPCP precipitation is 0.75 (0.1% significance level), suggesting the second mode of GPCP tropical precipitation is related to the phenomenon known as El Niño Modoki. During positive phase of El Niño Modoki, there are positive SSTA over central Pacific and negative SSTA over western and eastern Pacific, which will bring more precipitation to the central area and less to the western and eastern regions. The power spectrum of the PC2 time series, shown in Figure 3.2c, demonstrates 90% significant spectral peaks at 2.6 years and 8.5 years. The derived El Niño Modoki Index (EMI) is defined as EMI = C - 0.5(E + W),

where *C*, *E*, and *W* are the area-averaged SSTA over central tropical Pacific (165°E-140°W, 10°S-10°N), eastern tropical Pacific (110°W-70°W, 15°S-5°N), and western tropical Pacific (125°E-145°E, 10°S-20°N).

The EMI supplies an avenue of measuring events where warmer than normal SSTs occur primarily in the central Pacific with cooler than normal SSTs in the eastern and western portions of the ocean. Compared to traditional ENSO events indicative of warmer SSTs in the eastern Pacific, EMI allows for investigation of the western and central portions of the Pacific as well. Central-based El Niño Modoki events and traditional eastern-based ENSO episodes share seasonal and global weather patterns, but they also have separate pattern features and affect global precipitation patterns differently (Ashok *et al*., 2007). Hence the word "Modoki" means "same but different" in Japanese. El Niño Modoki involves ocean atmosphere coupled processes which include a unique tripolar sea-level pressure pattern during its evolution, analogous to the Southern Oscillation in the case of traditional El Niño events. For this reason, El Niño Modoki is argued to be a separate phenomenon and not part of the evolution of typical ENSO episodes. Previous studies have found that some of the strongest traditional ENSO events were rarely preceded by an El Niño Modoki episode, therefore verifying its contrasting nature (Weng *et al*., 2007; Ashok *et al*., 2007). Precipitation and temperature influences were discovered with impacts over regions in the Far East including Japan and New Zealand, and the western coast of the United States. These are opposite to those of the conventional ENSO, making El Niño Modoki a phenomenon of its own, unrelated to the evolution of ENSO. El Niño Modoki is thought to be produced by the weakening of equatorial easterlies related to a weakened zonal sea surface temperature gradient leading

to an increased flattening of the oceanic thermocline. The warming in the central Pacific is thus strengthened owing to the arrival of downwelling, equatorial Kelvin waves from the west and Rossby waves from the east. This appears to be a cause of more frequent and persistent occurrences of El Niño Modoki during recent decades.

3.3.2 CAM5 Precipitation at Tropics

PCA is also applied to the CAM5 precipitation over tropics (30°N-30°S) to investigate if the model can correctly simulate the influence of ENSO and El Niño Modoki on precipitation. The first leading mode accounts for 24.3% of the total variance of CAM5 tropical precipitation. Illustrated in Figure 3.3a is the spatial pattern of the CAM5 precipitation anomalies regressed on the first PC of CAM5 precipitation over tropics. This mode demonstrates patterns similar to the leading mode of the observed GPCP precipitation; however, magnitudes are somewhat under predicted. Comparison of the time series of the detrended and lowpass filtered SOI and the PC1 of the CAM5 precipitation simulation is shown in Figure 3.3b. The correlation coefficient between the two time series is 0.87 (0.1% significance level). Additionally, the PC1 of CAM5 tropical precipitation correlates well with PC1 from GPCP tropical precipitation with a correlation coefficient of 0.94 (0.1% significance level). The power spectrum of the PC1 mode, shown in Figure 3.3c, demonstrates strong spectral peaks between 2-7 years.

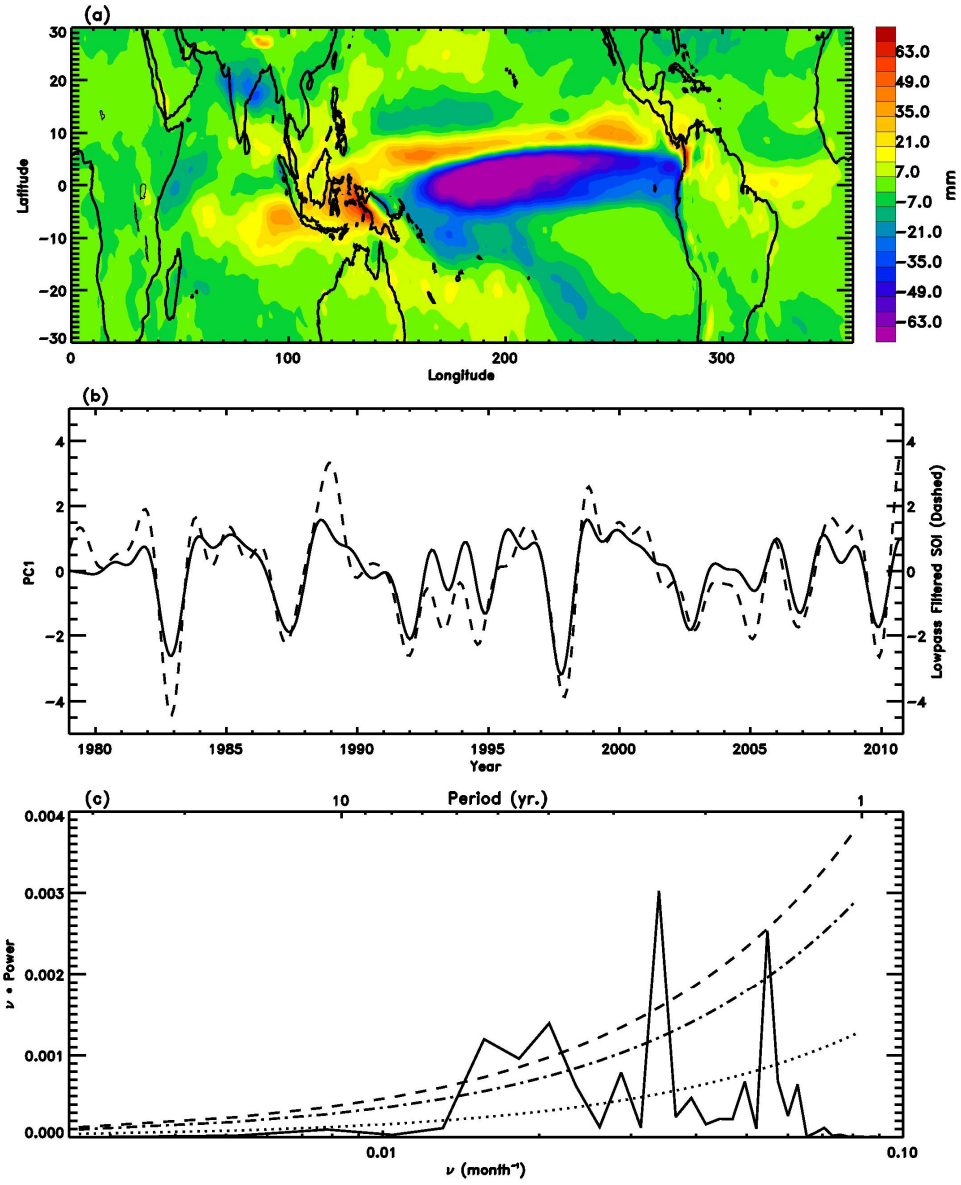

Figure 3.3. (a) The spatial pattern of the first mode of CAM5 precipitation anomalies in the tropics. Units are mm. (b) PC1 of the tropical CAM5 precipitation (solid line) and Southern Oscillation Index (dashed line). The correlation coefficient is 0.87 (0.1% significance level). (c) Power spectral estimate of the PC1 (Solid), red noise spectrum (Dotted), 90% and 95% confidence interval (Dashed). The first mode explains 24.3% of the total variance.

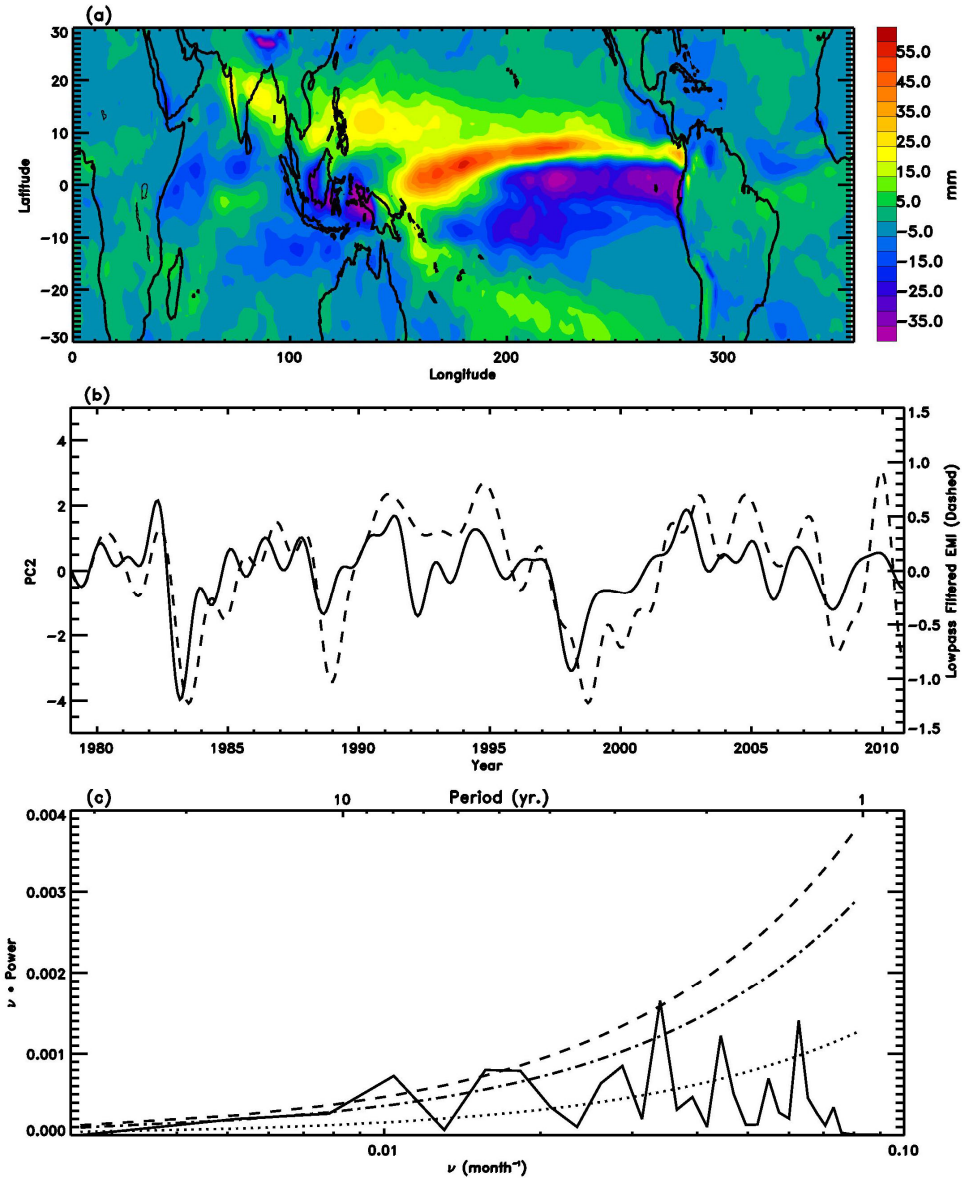

Figure 3.4. (a) Spatial pattern of the second mode of CAM5 precipitation anomalies in the tropics. Units are mm. (b) PC2 of the tropical CAM5 precipitation (solid line) and inverted El Niño Modoki Index (EMI) (dashed line). The correlation coefficient is 0.69 (0.1% significance level). (c) Power spectral estimate of PC2 (Solid), red noise spectrum (Dotted), 90% and 95% confidence interval (Dashed). The second mode explains 11.6% of the total variance.

The second mode of CAM5 tropical precipitation captures 11.6% of the total variance in the CAM5 tropical precipitation. Illustrated in Figure 3.4a is the spatial pattern of the CAM5 precipitation anomalies regressed on the second PC of CAM5 tropical precipitation. This mode demonstrates patterns similar to that of the observed GPCP second mode, although magnitudes are somewhat under predicted. The correlation coefficient between the PC2 and lowpass and detrended EMI is 0.69 (0.1% significance level), demonstrated in Figure 3.4b. Moreover, the PC2 of CAM5 tropical precipitation correlates well with PC2 from GPCP tropical precipitation with a correlation coefficient of 0.89 (0.1% significance level). The power spectrum of the PC2 of CAM5 tropical precipitation, shown in Figure 3.4c, reveals 90% significant spectral peaks at 2.5 years, 5-6 years, and 8 years.

3.4 Conclusions

The first leading mode of the GPCP PCA captured 31.9% of the total variance in tropical precipitation. The spatial pattern of the precipitation anomalies regressed on the first PC illustrates positive precipitation anomalies over western Pacific and negative anomalies over central and eastern Pacific, which is verified by a recent study between GPCP rainfall anomalies and Niño3 Index (Ashok *et al*., 2007). The correlation between PC1 and SOI suggests the first leading mode is related to ENSO. Additionally, the power spectrum of the PC1 time series demonstrates strong spectral peaks near 2-7 years, similar to those in ENSO.

The second mode of the GPCP PCA captured 15.6% of the total variance in tropical precipitation. The spatial pattern of the precipitation anomalies regressed on the second PC of GPCP tropical precipitation show positive precipitation anomalies over central Pacific and negative precipitation anomalies over western and eastern Pacific. This precipitation pattern can be explained by the unique tripole nature of the SSTA caused by El Niño Modoki. The correlation between PC2 and EMI suggests the second mode is related to the phenomenon known as El Niño Modoki. The power spectrum of the PC2 time series demonstrates 90% significant spectral peaks at 2.6 years and 8.5 years.

The first leading mode of the CAM5 model simulation PCA accounts for 24.3% of the total variance in tropical precipitation. The spatial pattern of the CAM5 precipitation anomalies regressed on the first PC of CAM5 precipitation over the tropics demonstrates patterns similar to the leading mode of the observed GPCP precipitation, although magnitudes are somewhat under predicted. Comparison of SOI and PC1 of CAM5 precipitation produced a very similar correlation with that of the observed GPCP precipitation. Furthermore, the PC1 of CAM5 tropical precipitation correlates well with PC1 from GPCP tropical precipitation with a correlation coefficient of 0.94 (0.1% significance level). The power spectrum of the PC1 mode demonstrates strong spectral peaks between 2-7 years, which is also consistent with that of the observed GPCP PC1.

The second mode of CAM5 tropical precipitation captured 11.6% of the total variance in the CAM5 tropical precipitation. The spatial pattern of the CAM5 precipitation anomalies regressed on the second PC of CAM5 tropical precipitation demonstrates patterns similar to that of the observed GPCP second mode, although

magnitudes are again somewhat under predicted. The correlation between the PC2 and EMI once again supplies evidence of the relationship between this mode and El Niño Modoki. The PC2 of CAM5 tropical precipitation also correlates well with the PC2 from GPCP tropical precipitation with a correlation coefficient of 0.89 (0.1% significance level). The power spectrum of the PC2 of CAM5 tropical precipitation reveals 90% significant spectral peaks at 2.5 years, 5-6 years, and 8 years, capturing 2 of the 3 significant peaks as the observations. Both observation and CAM5 model can capture the ENSO and El Niño Modoki signals in the tropical precipitation, although the signals in the CAM5 model are weaker than the observation.

3.5 Acknowledgements

I especially acknowledge Dr. Xun Jiang, whose comments and insight were invaluable to me concerning this chapter.

Chapter 4

Analyze the Variability of Precipitation over Polar Regions from Observation and Model

4.1 Introduction

The polar regions are very important to climate change. The processes in these regions influence the climate at all latitudes and are thought to be particularly sensitive to climate change (IPCC, 2001; Räisänen, 2001; Holland and Bitz, 2003). Since most of Earth's snow and ice are in the polar regions, these areas are expected to be the most affected by the snow/ice - surface albedo feedback effect (Curry and Schramm, 1994). Therefore, it is vital to study these regions and their response to global warming, for they should warm faster than other locations on Earth due to changing surface albedo projections (IPCC, 2001; Räisänen, 2001; Holland and Bitz, 2003). However, observations at the polar regions are limited and accompanied by many uncertainties.

In this chapter, we explore the influence of the annular modes on the precipitation over the polar region. The annular modes are hemispheric scale patterns of climate variability, which are the most important patterns of climate variability in the middle and high latitudes. There are two kinds of annular modes in Earth's atmosphere: the Northern Annular Mode (NAM) and Southern Annular Mode (SAM) (Limpasuvan and Hartmann, 1999). Since it is related closely to the North Atlantic Oscillation, NAM is also referred

to as the "Arctic Oscillation" (Thompson and Wallace, 1998; 2000). NAM's structure covers the larger part of the Arctic, and its variability is more closely related to surface air temperature fluctuations over the Eurasian continent. The annular modes are able to explain variances of week-to-week, month-to-month, or year-to-year in the extratropical atmospheric flow. It is not associated with the seasonal cycle.

The annular modes (NAM/SAM) are the first empirical orthogonal function (EOF) of geopotential height (GPH) over Arctic/Antarctic regions and represent an important tool in the study of winter hemisphere variability (Thompson and Wallace, 1998; 2000). By the PCA method, the original data GPH can be decomposed into two functions: the time function a which produces the principal component (PC) time series, and the space function f which produces the empirical orthogonal functions (EOFs). EOF1 (f_1) represents the spatial pattern for the leading mode of GPH. PC1 (a_1) refers to the leading PC time series of GPH, which is also called the "NAM index". The strength of the polar vortex is characterized by the NAM/SAM index, defined as the leading principal component time series of geopotential heights (Baldwin and Dunkerton, 2001). Positive NAM/SAM values represent a strong polar vortex and negative values show a weak one.

4.2 Data and Model

In addition to the GPCP precipitation dataset and CAM5 model previously introduced, NCEP2 reanalysis data are utilized in this chapter. NCEP2 reanalysis data is a joint product from the National Centers for Environmental Prediction (NCEP) and the National Center for Atmospheric Research (NCAR). These are global data incorporating

observations and numerical weather prediction (NWP) model output dating back to 1948. The data include near surface meteorological fields (temperature, geopotential height, zonal wind, and meridional wind) and surface fluxes. The grid size is 2.5° × 2.5° in 17 levels from 1000 hPa to 10 hPa.

4.3 Results

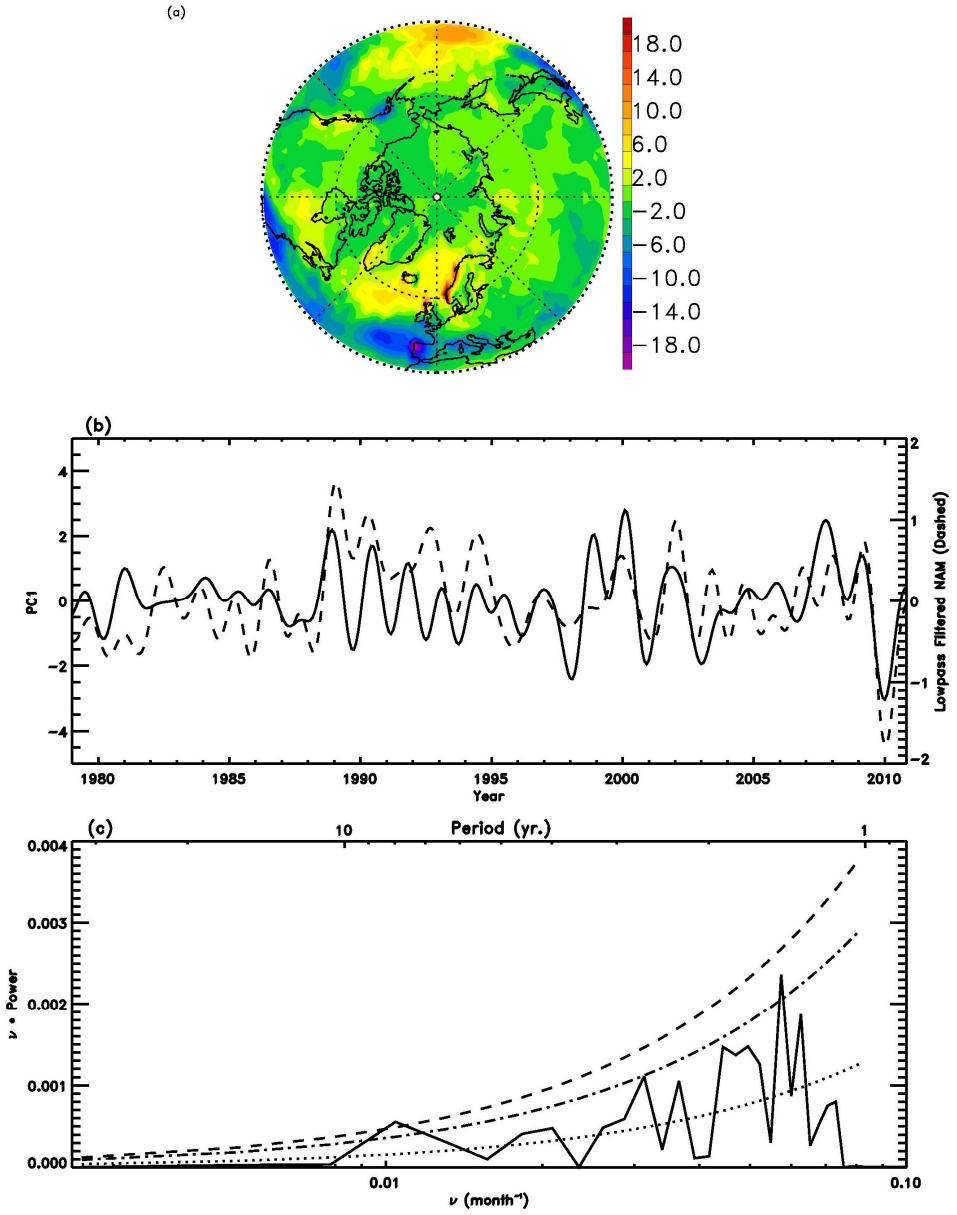

Figure 4.1. (a) The spatial pattern of the first mode of GPCP precipitation anomalies in the NH. Units are mm. (b) PC1 of the NH GPCP precipitation (solid line) and 300 mb NAM Index (dashed line). The correlation coefficient is 0.50 (0.1% significance level). (c) Power spectral estimate of the PC1 (Solid), red noise spectrum (Dotted), 90% and 95% confidence interval (Dashed). The first mode explains 8.3% of the total variance.

PCA is utilized to analyze interannual variability of the GPCP precipitation in the Arctic (30°N-90°N). The first leading mode accounts for 8.3% of the total variance of Arctic GPCP precipitation. The polar projection of the spatial pattern of the precipitation anomalies regressed upon PC1 of Arctic GPCP precipitation is shown in Figure 4.1a. The first mode is approximately zonally symmetric and illustrates negative precipitation anomalies in the polar region and positive precipitation anomalies in the mid-latitudes, which are coincident with the storm track regions. As shown in Figure 4.2a, the positive precipitation anomalies are related to the storm track activities calculated as the variance of sea-level pressure (Chang and Fu, 2002). The temporal behavior of PC1 in the northern hemisphere is demonstrated in Figure 4.1b. For comparison, we overlay the 300 mb Northern Annular Mode (NAM) index as a dashed line. The NAM index is the PC associated with the first leading mode, capturing 14.7% of the total variance for the NCEP2 geopotential height at 300 mb from 1979 to 2010 (Baldwin and Dunkerton, 1999; Thompson and Wallace, 2000). The correlation coefficient between the detrended PC1 and the detrended and lowpass filtered NAM index is 0.50 (0.1% significance level). When the polar vortex is stronger and the NAM index is positive, there are negative precipitation anomalies over the polar region and positive anomalies over the mid-latitudes. The power spectrum of the PC1 of Arctic precipitation in Figure 4.1c reveals 90% significant spectral peaks at 17 months, 32 months, and 8 years.

To explore the possible relationship between precipitation and storm track activities, we regress PC1 of precipitation with storm track data calculated by the variance of ECMWF-Interim sea-level pressure filtered by the 24 hour difference (Chang and Fu, 2002). PC1 of Arctic precipitation is used to regress with storm track data in the

northern hemisphere, shown in Figure 4.2a. Illustrated are positive storm track anomalies over north Pacific, North America, north Atlantic, and Europe. In the southern hemisphere, PC1 of Antarctic precipitation is used to regress with storm track data. As shown in Figure 4.2b, there are positive storm track anomalies over south Pacific Ocean. Regressed storm track magnitudes are up to 10 hPa^2, which is similar to 10% of the local storm track climatological value. The positive storm track anomalies are consistent with the positive precipitation anomalies in the first leading modes of precipitation for both hemispheres.

The statistical significance of signals in a power spectrum is obtained by comparing the amplitude of a spectral peak to the red noise spectrum. The red noise spectrum used in constructing null hypothesis for significance is the spectrum associated with the autocorrelation function, ρ (Gilman *et al*., 1963). Here, ρ is the average of one-lag autocorrelation and the square root of the two-lag autocorrelation. The red noise spectrum associated with the autocorrelation function is illustrated by the following formula:

$$L(h,\rho,M) = \frac{1-\rho^2}{1-2\rho\cos(\frac{h\pi}{M})+\rho^2},$$

where h is frequency and M is the maximum lag (Gilman *et al*., 1963). The 90% and 95% confidence interval for the power spectrum are found using *F*-statistics to compare the spectrum to the red noise spectrum.

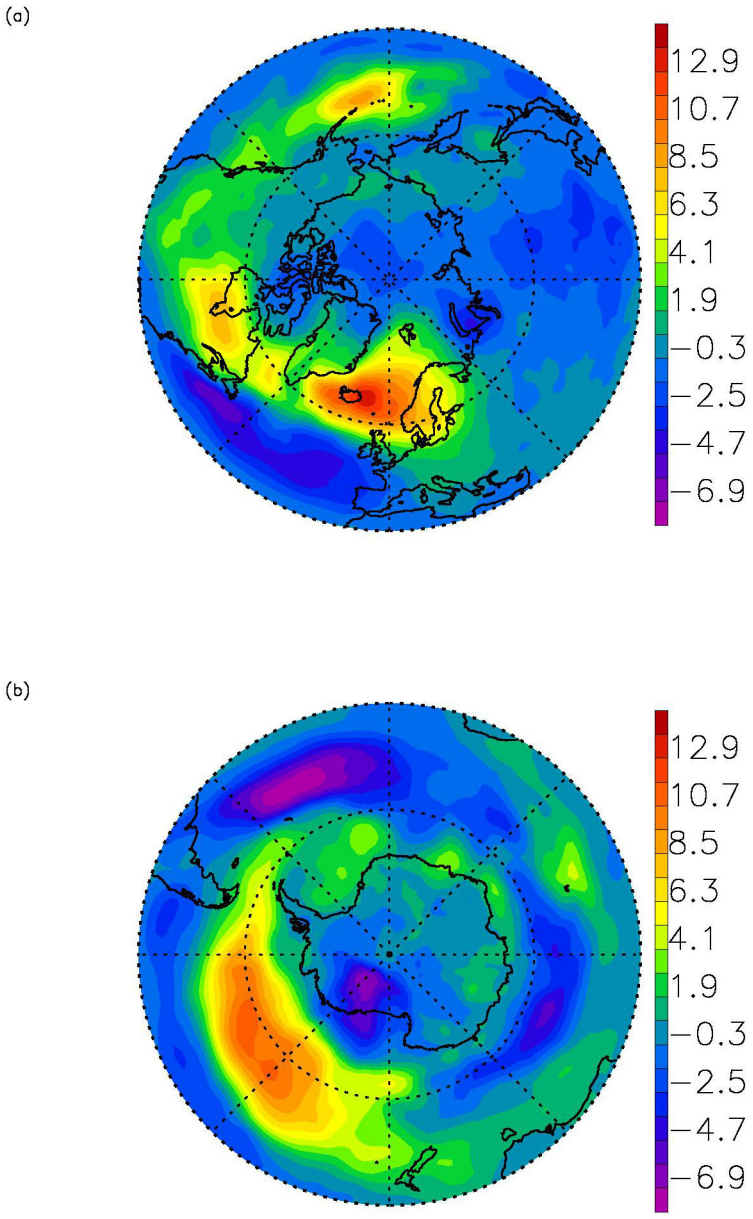

Figure 4.2. (a) Regress Arctic PC1 from ECMWF-Interim storm track data. (b) Regress Antarctic PC1 from ECMWF-Interim storm track data. Units are hPa^2.

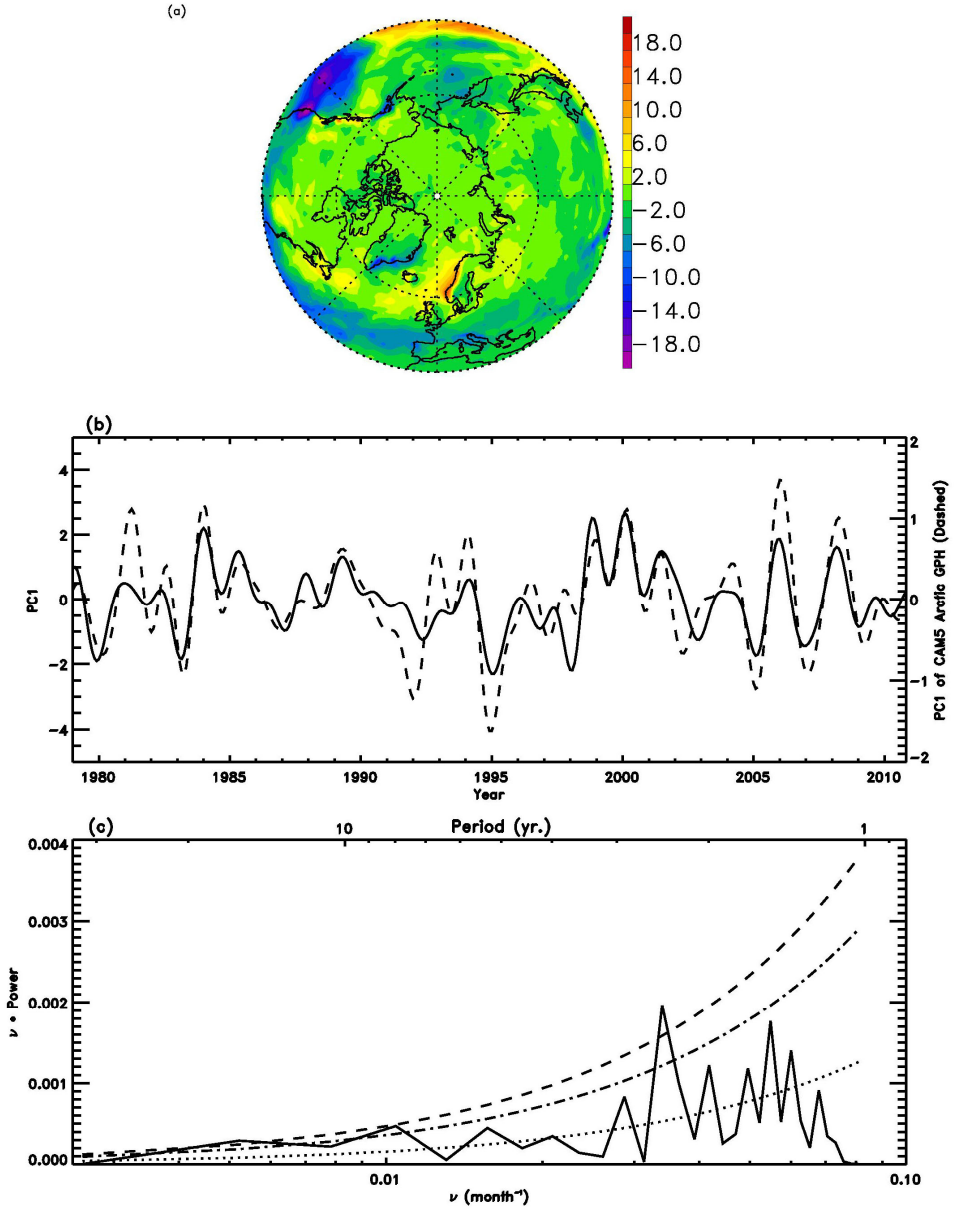

Figure 4.3. (a) The spatial pattern of the first mode of CAM5 precipitation anomalies in the NH. Units are mm. (b) PC1 of the NH CAM5 precipitation (solid line) and PC1 of CAM5 300 mb geopotential height (dashed line). The correlation coefficient is 0.8 (0.1% significance level). (c) Power spectral estimate of the PC1 (Solid), red noise spectrum (Dotted), 90% and 95% confidence interval (Dashed). The first mode explains 8.2% of the total variance.

PCA is also applied to the CAM5 precipitation over Arctic (30°N-90°N) to investigate if the model can correctly simulate the variability in the high latitudes. The first leading mode accounts for 8.2% of the total variance of CAM5 precipitation in the Arctic. Illustrated in Figure 4.3a is the spatial pattern of the CAM5 precipitation anomalies regressed on the first PC of CAM5 Arctic precipitation. This mode demonstrates patterns similar to that of the observed GPCP leading mode; yet, it does not capture the high precipitation anomalies over the Pacific Ocean. To explore the possible relationship between this mode and the polar vortex simulated in the CAM5 model, we calculate the leading mode and PC of the CAM5 300 mb geopotential height from 1979 to 2010. Detrended and lowpass filtered PC1 of the CAM5 300 mb geopotential height is overlain with PC1 of Arctic CAM5 precipitation in Figure 4.3b. The correlation between the two time series is 0.8 (0.1% significance level). Additionally, the CAM5 PC1 correlates well with GPCP PC1 with a correlation coefficient of 0.44 (0.1% significance level). The power spectrum of the model PC1 mode, shown in Figure 4.3c, demonstrates 90% significant spectral peaks at 30 months and 8 years.

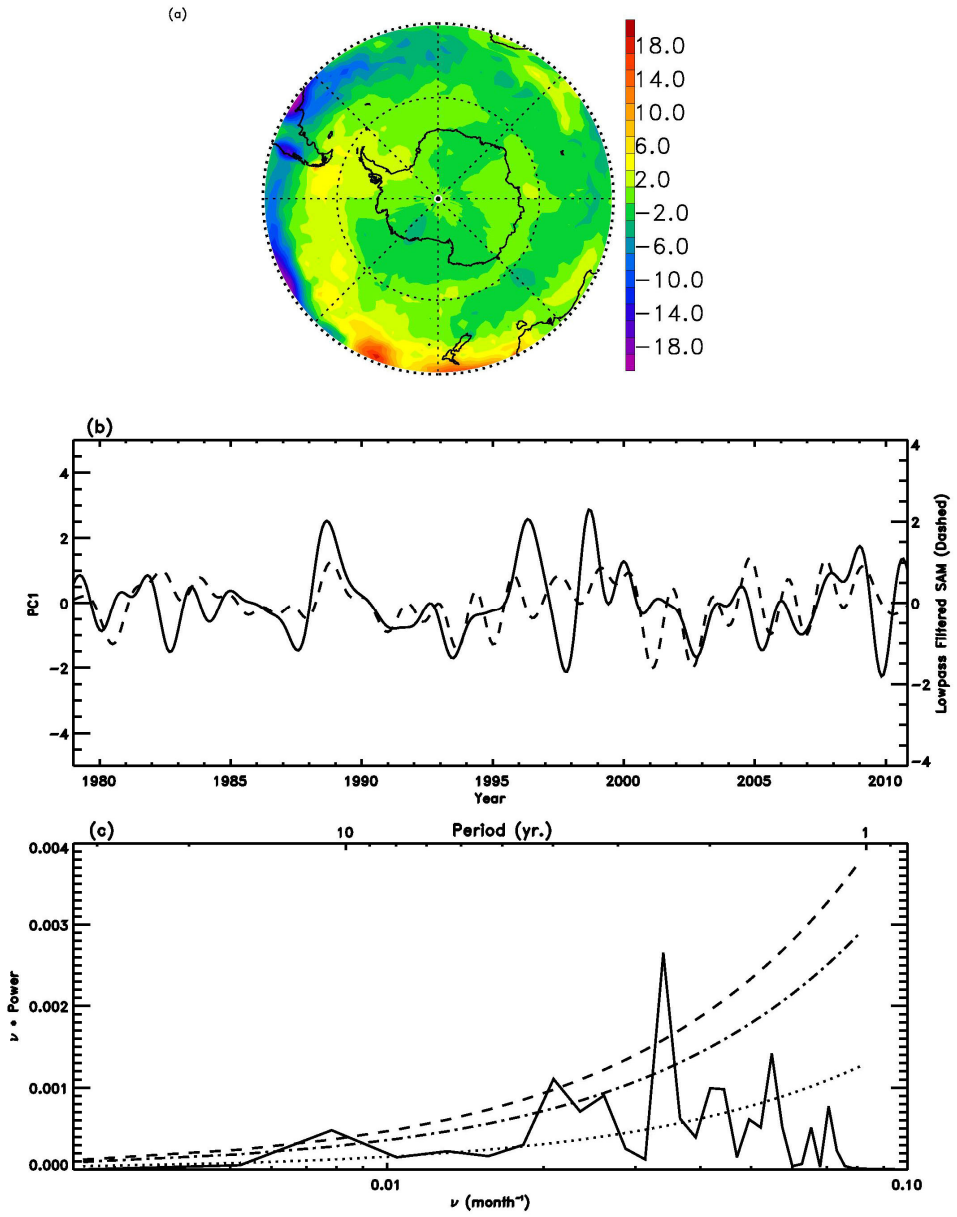

Figure 4.4. (a) The spatial pattern of the first mode of GPCP precipitation anomalies in the SH. Units are mm. (b) PC1 of the SH GPCP precipitation (solid line) and 300 mb SAM Index (dashed line). The correlation coefficient is 0.40 (0.1% significance level). (c) Power spectral estimate of the PC1 (Solid), red noise spectrum (Dotted), 90% and 95% confidence interval (Dashed). The first mode explains 13.2% of the total variance.

In the southern hemisphere (SH), the first mode accounts for 13.2% of the total variance, illustrated in Figure 4.4a. The first mode is zonally symmetric and strongly resembles the first mode in the northern hemisphere (NH); it is associated with the Southern Hemisphere Annular Mode (SAM) (Thompson and Wallace, 2000). The first mode has negative precipitation anomalies in the polar region and positive precipitation anomalies in the mid-latitudes. The positive precipitation anomalies are coincident with the positive storm track anomalies over south Pacific Ocean, as shown in Figure 4.2b. PC1 of Antarctic GPCP precipitation is compared with lowpass filtered 300 mb SAM index (dotted line) in Figure 4.4b. The correlation between the detrended PC1 and detrended and lowpass filtered SAM index is 0.40 (0.1% significance level). A stronger polar vortex in the SH (positive SAM index) will lead to less precipitation in the SH high latitudes. The power spectrum of PC1, demonstrated in Figure 4.4c, reveals 90% significant peaks at 30 months, 4 years, and 10 years.

PCA is now applied to the CAM5 precipitation over Antarctic (30°S-90°S) to investigate if the model can correctly simulate the variability in the SH high latitudes. The first leading mode accounts for 10.3% of the total variance of CAM5 precipitation at Antarctic. Illustrated in Figure 4.5a is the spatial pattern of the CAM5 precipitation anomalies regressed on the first PC of CAM5 Antarctic precipitation. This mode demonstrates patterns similar to that of the observed GPCP leading mode, although the positions for the positive precipitation anomalies are a little different than the observation. Comparison of the time series of the PC1 of CAM5 precipitation over Antarctic and the PC1 of the CAM5 300 mb geopotential height reveals a good correlation coefficient of 0.5 (0.1% significance level), shown in Figure 4.5b. Moreover,

the model PC1 corresponds well with the PC1 of Antarctic GPCP data with a correlation coefficient of 0.75 (0.1% significance level). The power spectrum of the PC1 mode, shown in Figure 4.5c, demonstrates 90% significant spectral peaks at 22 months, 3.5 years, and 11 years.

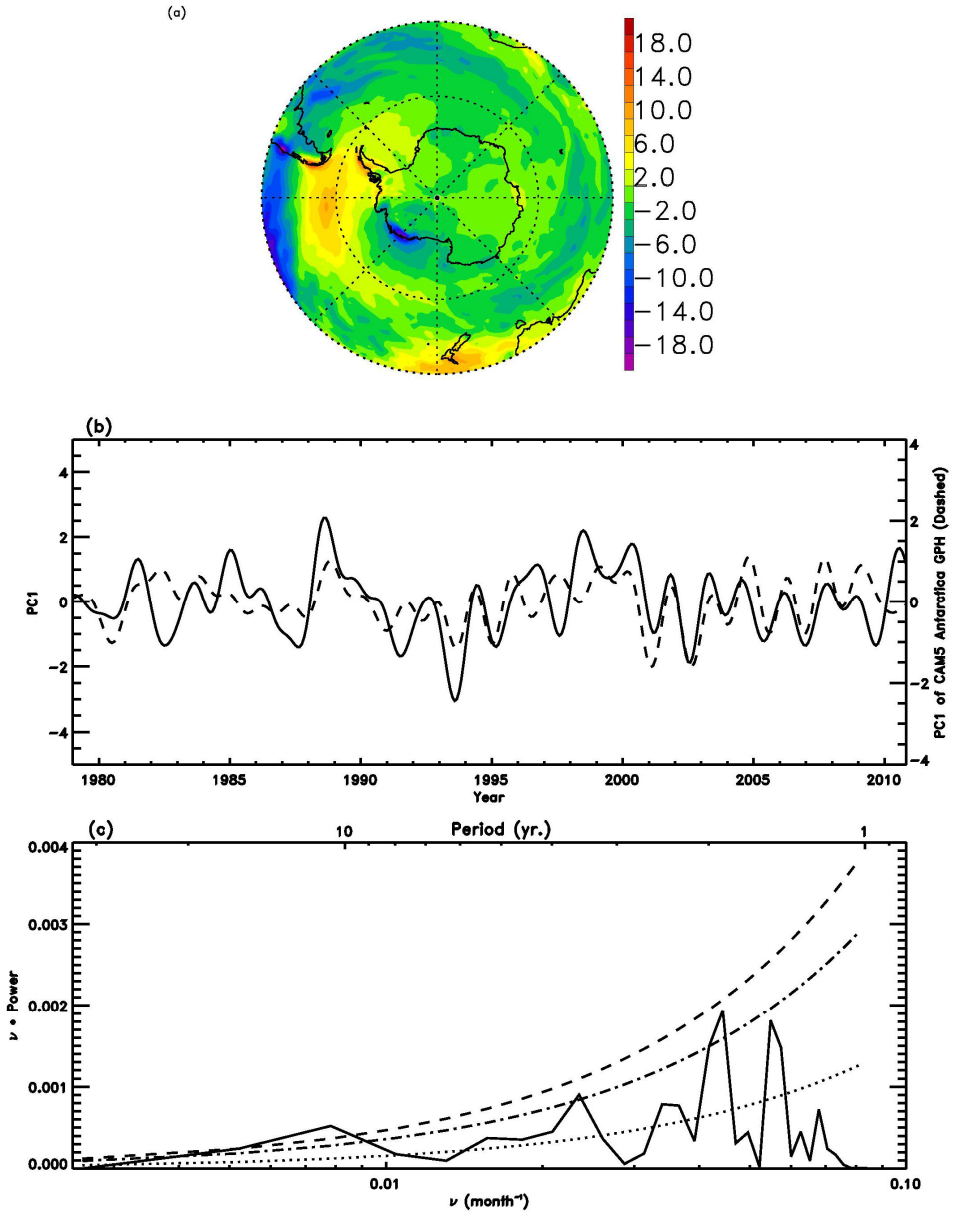

Figure 4.5. (a) The spatial pattern of the first mode of CAM5 precipitation anomalies in the SH. Units are mm. (b) PC1 of the SH CAM5 precipitation (solid line) and PC1 of CAM5 300 mb geopotential height (dashed line). The correlation coefficient is 0.5 (0.1% significance level). (c) Power spectral estimate of the PC1 (Solid), red noise spectrum (Dotted), 90% and 95% confidence interval (Dashed). The first mode explains 10.3% of the total variance.

4.4 Conclusions

The leading mode of the GPCP precipitation PCA in the Arctic (30°N-90°N) captured 8.3% of the total variance in Arctic precipitation. The spatial pattern of the precipitation anomalies regressed upon PC1 of Arctic GPCP precipitation was found to be approximately zonally symmetric with negative precipitation anomalies in the polar region and positive precipitation anomalies in the mid-latitudes, which is related to NAM. These anomalies are coincident with the storm track regions within the subtropics and help explain the significance of the observed spatial pattern. The correlation between Arctic PC1 and NAM index suggests that when a stronger polar vortex exists, the NAM index is positive, there are negative precipitation anomalies over the Arctic, and positive precipitation anomalies exist in the NH mid-latitudes. Additionally, the power spectrum of the PC1 of Arctic precipitation revealed 90% significant spectral peaks at 17 months, 32 months, and 8 years.

The first leading mode of CAM5 model precipitation in the Arctic accounts for 8.2% of the total variance, almost exactly that of the GPCP PC1. The spatial pattern of the CAM5 precipitation anomalies regressed on the first PC of CAM5 Arctic precipitation demonstrates patterns similar to that of the observed GPCP leading mode; however, it does not capture the high precipitation anomalies over the NH Pacific Ocean. PC1 of the CAM5 300 mb geopotential height compared with PC1 of Arctic CAM5 precipitation demonstrates a very good correlation, which suggests this mode and the simulated polar vortex are related. Furthermore, the CAM5 PC1 correlates well with GPCP PC1, illustrating the model's ability in simulating the observations. The power spectrum of the model PC1 mode demonstrates 90% significant spectral peaks at 30

months and 8 years, achieving 2 of the 3 spectral peaks similar to that of the observations.

In the southern hemisphere (SH), the leading mode of the GPCP precipitation PCA in the Antarctic (30°S-90°S) captured 13.2% of the total variance in Antarctic precipitation. The first mode is zonally symmetric and strongly resembles the first mode in the northern hemisphere (NH) when associated with the Southern Hemisphere Annular Mode (SAM). The first mode demonstrates negative precipitation anomalies in the polar region and positive precipitation anomalies in the mid-latitudes. The leading PC1 of Antarctic GPCP precipitation compared with SAM index shows a good correlation. This correlation gives evidence of a stronger polar vortex in the SH when the SAM index is positive, leading to less precipitation over the Antarctic and more over the SH mid-latitudes. The power spectrum of PC1 revealed 90% significant peaks at 30 months, 4 years, and 10 years.

The PCA of the CAM5 precipitation leading mode accounts for 10.3% of the total variance in precipitation over the Antarctic. The spatial pattern of the precipitation anomalies regressed on the first PC of CAM5 Antarctic precipitation demonstrates patterns similar to that of the observed GPCP leading mode, revealing the model can correctly simulate the variability in the SH high latitudes. Nevertheless, the position of the positive precipitation anomalies is slightly different. Comparison of the time series of the PC1 of CAM5 precipitation and the PC1 of the CAM5 300 mb geopotential height reveals a good correlation. The model PC1 corresponds well with the PC1 of Antarctic GPCP observed data. The power spectrum of the CAM5 PC1 mode demonstrates 90% significant spectral peaks at 22 months, 3.5 years, and 11 years, showing 2 of the 3 significant peaks occurring approximately 6-8 months earlier than the observations.

4.5 Acknowledgements

I especially acknowledge Dr. Jingqian Wang, whose previous research supplied tremendous insight into this chapter.

Chapter 5

Investigation of Precipitation Variations over Wet and Dry Areas from Observation and Model

5.1 Introduction

The influence of greenhouse gases on global warming has been investigated in numerous studies (Dickinson and Cicerone, 1986; IPCC, 2007; IPCC, 2013). This paper focuses on the effect global warming may have on the temporal variation and spatial pattern of precipitation and its possible influence on causing precipitation extremes. Compared with the Clausius-Clapeyron equation relating water vapor to the atmospheric temperature (Trenberth *et al.,* 2005; Santer *et al.,* 2007), there is no simple relationship between precipitation and the atmospheric temperature (Trenberth and Shea, 2005; Adler *et al*., 2008; Allan and Soden, 2008; Liu *et al*., 2009; Li *et al*., 2011). This is because precipitation is influenced by more factors such as atmospheric circulation and cloud (Bony *et al*., 2013). It is also found that changes in the precipitation can be attributed to natural climate variability and external influences (Bosilovich *et al*., 2005; Richard *et al*., 2010; Marvel and Bonfils, 2013). Most observational studies (Adler *et al*., 2003; Gu *et al*., 2007; Adler *et al*., 2008; Li *et al*., 2011) and climate models (Allen and Ingram, 2002; Held and Soden, 2006; Stephens and Ellis, 2008; Lambert *et al*., 2008; John *et al*., 2009) suggest that global precipitation is increasing more slowly than the total mass of

water vapor in response to global warming. Previous studies (Chou and Neelin, 2004; Allan and Soden, 2007; Chou *et al*., 2009; Li *et al*., 2011; Durack *et al*., 2012; Polson *et al*., 2013) tried to separate the data into wet versus dry regions; they found that precipitation has an increasing tendency in the wet areas and has a decreasing tendency in dry areas, which is referred to as the "rich-get-richer" mechanism. Recently, Chou *et al*. (2013) found that the wet seasons become wetter, and the dry seasons become dryer. Here, we investigate whether a current climate model can capture the characteristics of the temporal variations of the precipitation by emphasizing the role of the greenhouse gases. Quantitatively simulating the precipitation trend will not only help predict the variation of precipitation in the future, but also will provide a numerical basis to better understand the physics behind the temporal and spatial variability of precipitation.

5.2 Methodology and Data

Both observations and numerical simulations are employed to examine precipitation under two different regions within 40ºS-40ºN: dry areas with precipitation less than 50 mm/month and wet areas with precipitation greater than 200 mm/month. By comparing the current atmospheric model to observations, we can explore how well the model performs in simulating precipitation. In addition, a diagnostic analysis of the numerical simulation will be conducted to investigate the physics behind the temporal trends of precipitation over different areas.

We use the NASA Goddard Institute for Space Studies (GISS) model historic run to study the precipitation, temperature, and water vapor. Specifically, the GISS

atmospheric general circulation model coupled to the hybrid-isopycnic ocean model (HYCOM) (Shindell *et al*., 2006) is utilized. It is an updated version that is used for the IPCC AR4 report (IPCC, 2007). The GISS model has a grid size of $4^\circ \times 5^\circ$ (latitude by longitude) and uses the Model E atmospheric code with 20 layers in the vertical, a model top at 0.1 hPa, and is coupled to the HYCOM ocean model (v. 0.9, 2×2×L16). The atmosphere model includes a gravity-wave drag parameterization in the stratosphere. The HYCOM dynamic ocean model can produce a reasonable magnitude of El Niño Southern Oscillation (ENSO)-like variability (Shindell *et al*., 2006). This model has been used to study the influence of solar and anthropogenic forcing on the tropical hydrology (Shindell *et al*., 2006) and explore the climate drift on twenty-first century projections (Liang *et al*., 2013). The control run starts with year 1850 atmospheric conditions containing fixed amounts of greenhouse gases. The historic model simulation includes the historic greenhouse gas changes in the radiative forcing.

The observational studies of precipitation are based on the data sets from the Global Precipitation Climatology Project (GPCP), which is an international project to construct the global long-term record of precipitation over the whole world on behalf of the World Meteorological Organization (WMO), the World Climate Research Programme (WCRP), and the Global Energy and Water Experiment (GEWEX) (Huffman *et al.,* 1997). There are many investigators and organizations contributing to this project (Adler *et al*., 2003; Schneider *et al*., 2008; Huffman *et al*., 2009). The data sets of precipitation from the latest version of the GPCP (i.e., Version 2.2) are available on the public websites maintained by the Physical Sciences Division (PSD) of the Earth System Research Laboratory (ESRL) in the National Oceanic & Atmospheric Administration

(NOAA). GPCP Version 2.2 precipitation data are derived from satellite and gauge measurements. It incorporates data from SSM/I emission estimates, F17 SSMIS, SSM/I scattering estimates, GPI and OPI estimates and rain gauge analysis, and TOVS estimates (Huffman *et al*., 2012). The spatial resolution of GPCP V2.2 precipitation is $2.5^\circ \times 2.5^\circ$ (latitude by longitude). Analyses based on the observational data sets are conducted to examine the consistency between the historic simulation and the observational study from 1988 to 2012, where GPCP data overlap with Special Sensor Microwave Imager data and are believed to be more reliable (Allan *et al*., 2010).

5.3 Results

The spatial pattern of the observed climatological GPCP V2.2 precipitation for 1988-2012 is shown in Figure 5.1a. The high precipitation and low precipitation areas are defined as the areas with climatological monthly mean precipitation larger than 200 millimeters per month (mm/mon) and less than 50 mm/mon, respectively. The high precipitation areas and low precipitation areas are respectively highlighted by the solid white contours and dotted white contours in Figure 5.1a. Figure 5.1a illustrates that the high precipitation area is roughly the same as the Inter-Tropical Convergence Zone (ITCZ), identified by the highly reflective clouds (Waliser and Gautier, 1993). The low precipitation area comprises most of the other regions in the tropics and mid-latitudes. Two different approaches were attempted when evaluating these data in preparation for plotting a time series. Since the ITCZ fluctuates in position throughout the year, one way to prepare the data is to allow the wet and dry areas to change position with month to

follow the movement of the ITCZ. Another way is to calculate the precipitation over the climatological wet and dry areas as shown in Figure 5.1a. Both approaches yielded similar results. Time series of the observed precipitation over the climatological wet and dry areas are plotted in Figures 5.1b and 5.1c, which include data over both land and ocean between 40°S-40°N. From this temporal variation of precipitation, it is evident that the areas already receiving great precipitation tend to receive more, while the areas already receiving little precipitation tend to receive less. The trend and uncertainty associated with the wet areas are 6.57 ± 0.27 mm/mon/decade, while for the dry areas are -0.98 ± 0.23 mm/mon/decade. Details for trends are listed in Table 5.1. El Niño Southern Oscillation (ENSO) signals have been removed from the precipitation time series at each location by a multiple regression method to avoid large biases in the trend due to significant interannual variability. Also applied to the data was a 20-month lowpass filter to remove the high frequency signals. The lowpass filter is constructed as a convolution of a step function with a Hanning window and chosen to obtain a full signal from periods above 20 months. The linear trend coefficient for the time series is calculated from the least-square fitting method. The standard error of the linear trend is estimated by $SE(b) = (\sigma/\sqrt{N_1})/\sqrt{(1/N_2)\sum x_i^2}$ (Bevington and Robinson, 2003), where σ is the standard deviation of the data, N_1 is the number of degrees of freedom of the data, N_2 is the length of the data set, and x_i is the time series corresponding to a number of measurements with $\sum x_i = 0$. The number of degrees of freedom N_1 is estimated by a formula $N_1 = N_2\left[1 - r(\Delta x)^2\right]/\left[1 + r(\Delta x)^2\right]$ suggested by Bretherton *et al*. (1999), where $r(\Delta x)$ is the autocorrelation corresponding to a lag of time interval Δx.

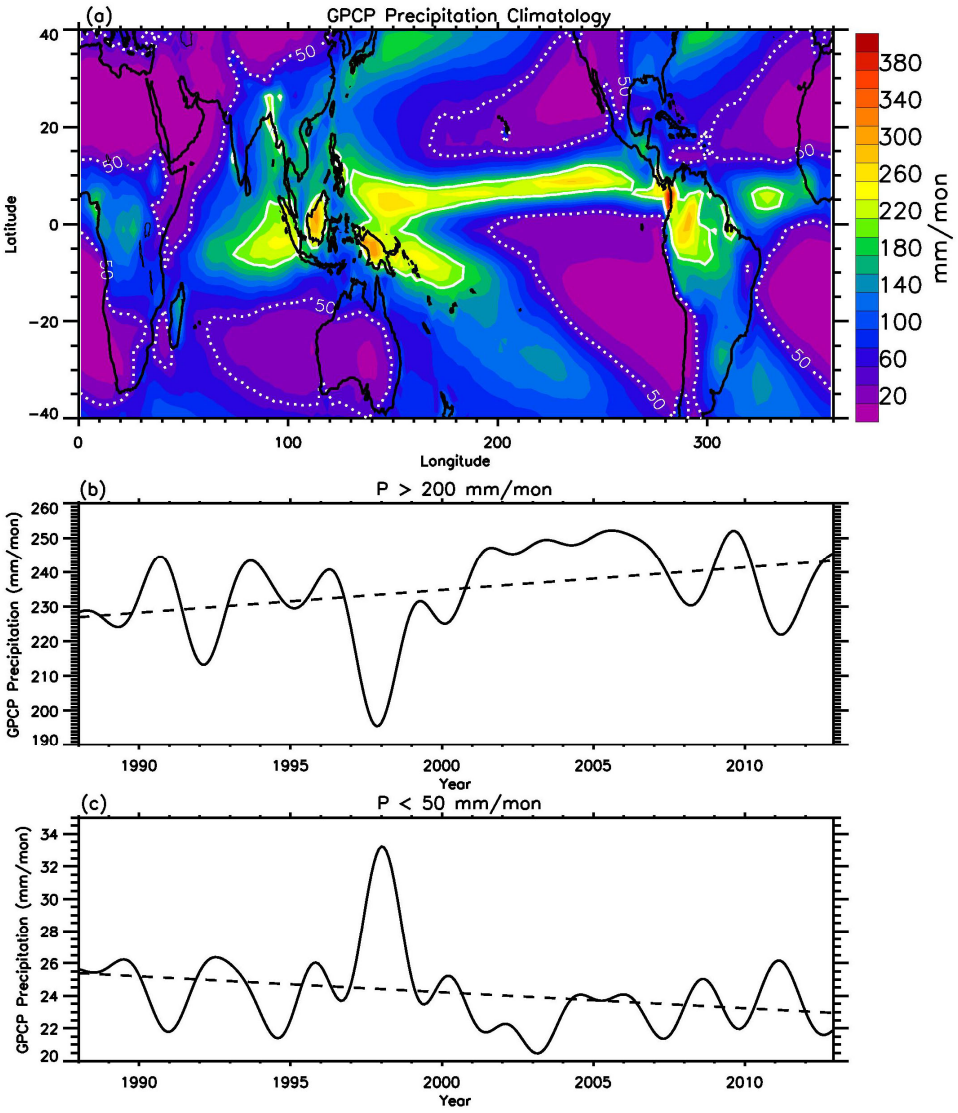

Figure 5.1. (a) Spatial pattern of the mean GPCP V2.2 precipitation (P) for 1988-2012 over the tropical and subtropical regions (40ºS-40ºN). (b) Lowpass filtered time series of precipitation averaged over high precipitation areas (P > 200 mm/mon). (c) Lowpass filtered time series of precipitation averaged over low precipitation areas (P < 50 mm/mon). El Niño Southern Oscillation (ENSO) signals have been removed from the time series by a regression method based on the Niño3.4 index. A lowpass filter is also applied to remove the high frequency signals. Solid white contours refer to the wet area where the precipitation is higher than 200 mm/month. Dotted white contours refer to the dry area where the precipitation is lower than 50 mm/month.

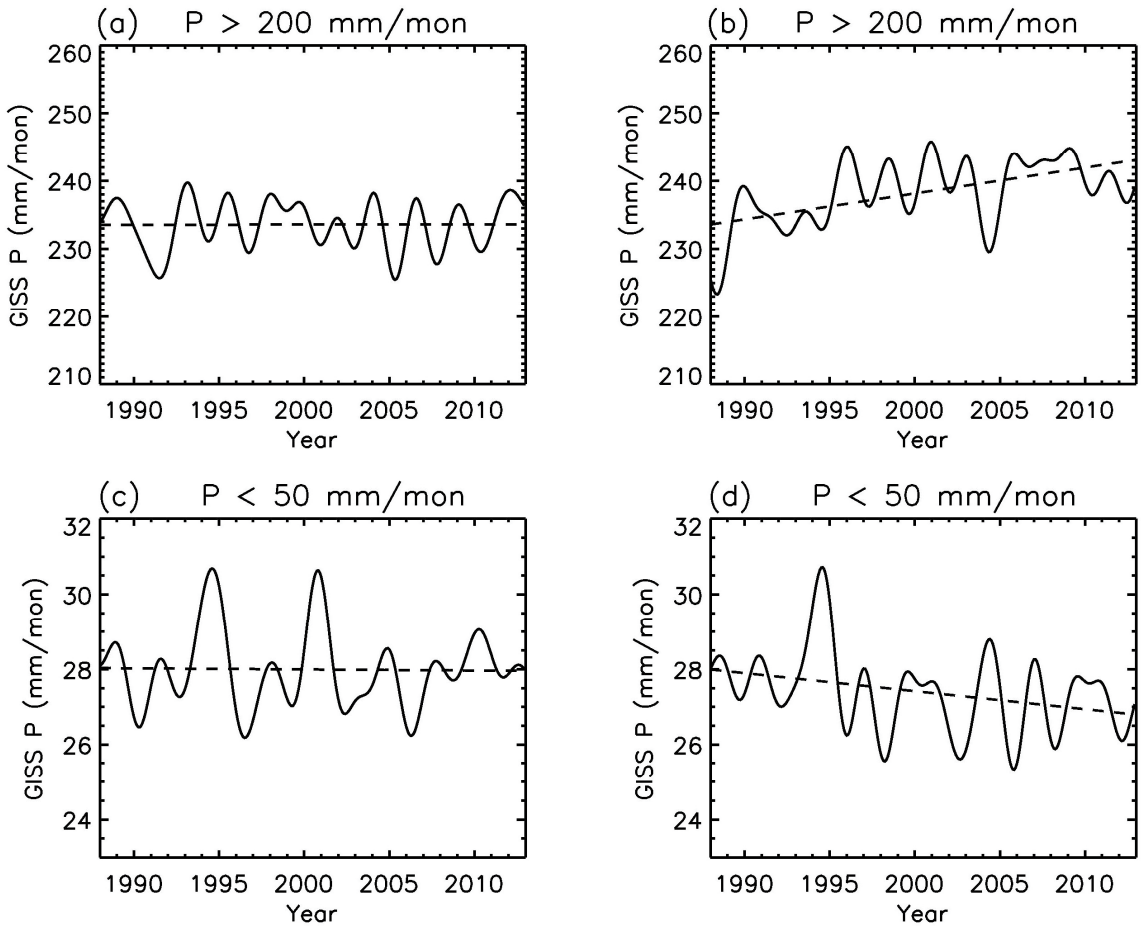

Figure 5.2. Lowpass filtered time series for precipitation (P) from GISS-HYCOM. (a) P over high precipitation (P > 200 mm/mon) from the control run (solid line) and trend (dashed line). (b) P over high precipitation area from the historic run (solid line) and trend (dashed line). (c) Same as (a) except for areas with precipitation < 50 mm/mon. (d) Same as (b) except for areas with precipitation < 50 mm/mon.

Next, we use the NASA GISS-HYCOM model to investigate whether the model can capture the overall trends seen in the observations and reproduce the characteristics of precipitation. We conduct experimental simulations in a control run where the greenhouse gases are fixed and a historic run where the historic greenhouse gases are included. Figure 5.2 illustrates the identified areas of high and low precipitation and contains each of their precipitation trends for both the control and historic simulations.

Corresponding trends and uncertainties in the control simulation for the wet areas are 0.02 ± 0.19 mm/mon/decade with -0.03 ± 0.24 mm/mon/decade for the dry areas, as shown in Figures 5.2a and 5.2c. There is no significant trend in the precipitation over the wet and dry areas when the greenhouse gas concentrations are fixed. In contrast, the historic run demonstrates trends of 3.8 ± 0.17 mm/mon/decade and -0.48 ± 0.21 mm/mon/decade for the wet and dry areas, respectively, as shown in Figures 5.2b and 5.2d. The trends (3.8 ± 0.17 mm/mon/decade and -0.48 ± 0.21 mm/mon/decade) in the GISS precipitation are smaller than those seen in the observations (Figures 5.1b and 5.1c), which might be related to the weakness of the model in simulating the Pacific Decadal Variability (PDV). As suggested by Gu and Adler (2012), the PDV can also contribute to the long-term trend of precipitation in addition to global warming. The GISS-HYCOM model cannot simulate the PDV well, which might contribute to the weak trends in the model precipitation.

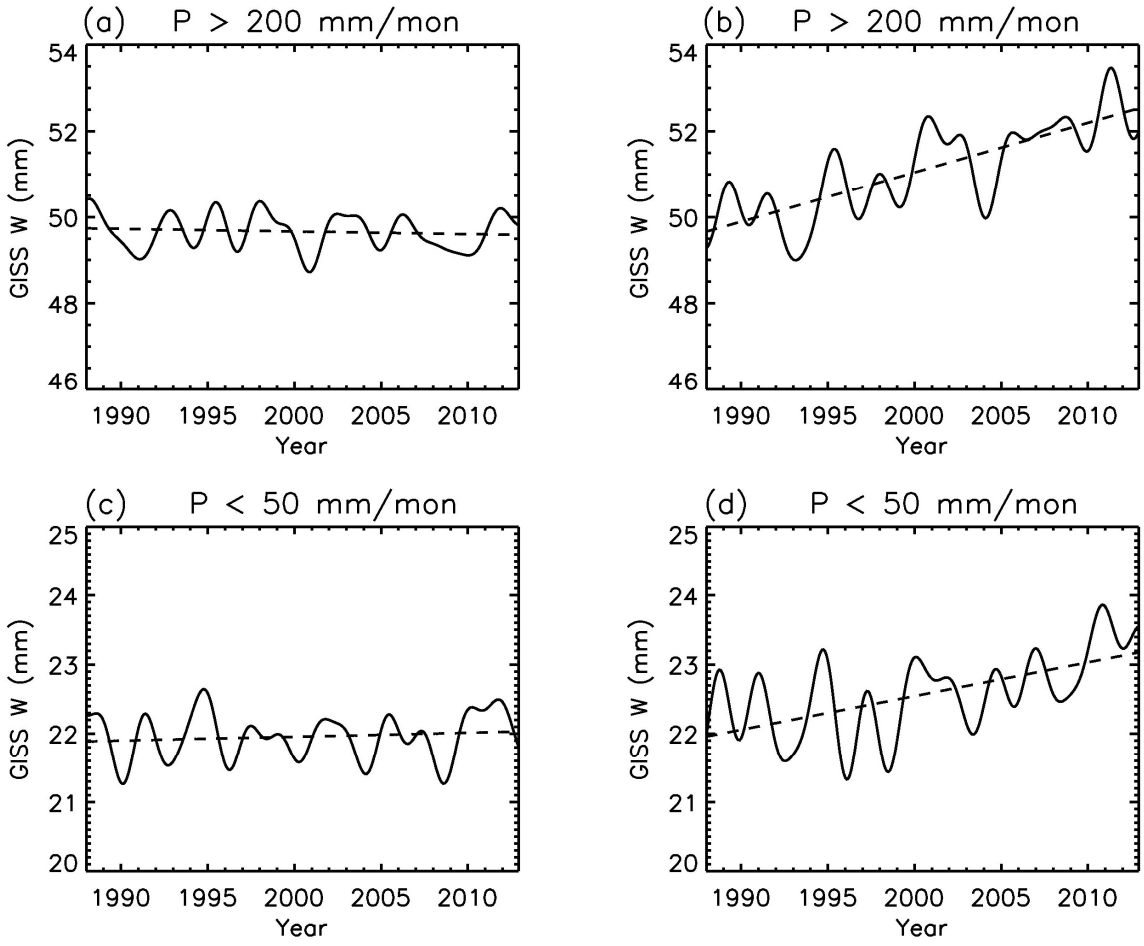

Figure 5.3. Lowpass filtered time series for column water vapor (W) from GISS-HYCOM. (a) W over high precipitation (P > 200 mm/mon) from the control run (solid line) and trend (dashed line). (b) W over high precipitation area from the historic run (solid line) and trend (dashed line). (c) Same as (a) except for areas with precipitation < 50 mm/mon. (d) Same as (b) except for areas with precipitation < 50 mm/mon.

The concentration of water vapor is one factor that can influence precipitation. Figure 5.3 illustrates the trends of column water for both the historic and control runs in the wet and dry areas. Corresponding trends in the control simulation for the wet areas are -0.06 ± 0.18 mm/mon/decade with 0.057 ± 0.20 mm/mon/decade for the dry areas. Column water trends for the historic run are 1.15 ± 0.21 mm/mon/decade over the wet areas with 0.49 ± 0.20 mm/mon/decade for the dry areas, as shown in Figures 5.3b and

5.3d. The historic run exhibits a strong positive trend for both the wet and dry areas, while the control run reveals virtually no trend in either. Furthermore, of considerable note is the strength of the trend in column water and the model's ability to simulate it with low uncertainties and small deviations.

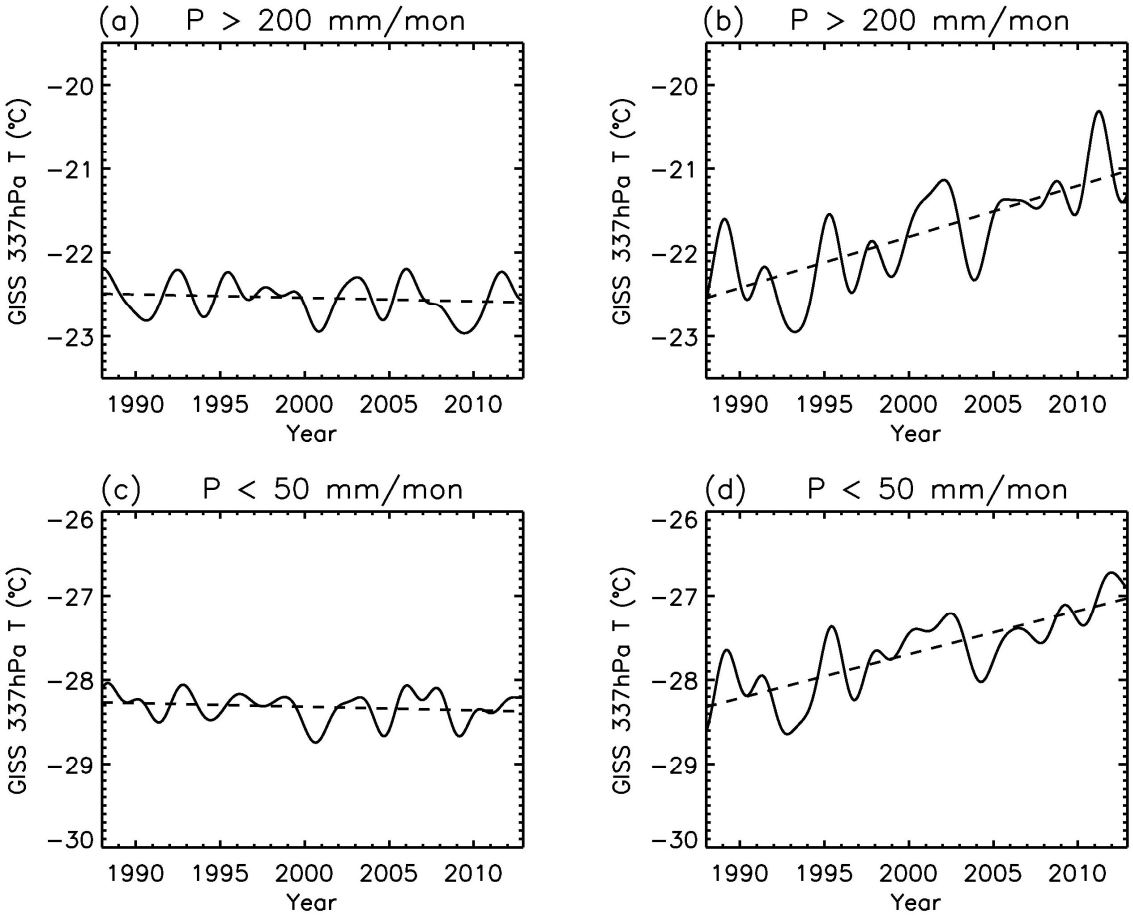

Figure 5.4. Lowpass filtered time series for 337 hPa temperature (T) from GISS-HYCOM. (a) T over high precipitation (P > 200 mm/mon) from the control run (solid line) and trend (dashed line). (b) T over high precipitation area from the historic run (solid line) and trend (dashed line). (c) Same as (a) except for areas with precipitation < 50 mm/mon. (d) Same as (b) except for areas with precipitation < 50 mm/mon.

The concentration of water vapor is related to the atmospheric temperature by the Clausius-Clapeyron equation (Salby, 2012). Therefore, we further examine the temporal variation of atmospheric temperature from the simulations by the GISS model. Results of the GISS 337 hPa temperature averaged in the identified areas of high and low precipitation are shown in Figure 5.4 for both the historic and control runs. Corresponding trends and uncertainties found in the control simulation for the wet areas are -0.04 ± 0.19 °C/decade and -0.04 ± 0.20 °C/decade for the dry areas. Trends for the 337 hPa temperature in the historic run are 0.61 ± 0.23 °C/decade over the wet areas and 0.52 ± 0.22 °C/decade over the dry areas, as illustrated in Figures 5.4b and 5.4d. Temperature has positive trends over both wet and dry areas, which are responses to the greenhouse forcing in the historic simulation. According to the Clausius-Clapeyron law, air with high temperature will hold more water vapor. Column water vapor also shows positive trends in both the wet and dry areas in Figure 5.3. This behavior is different from the temporal variation of precipitation for the wet and dry areas.

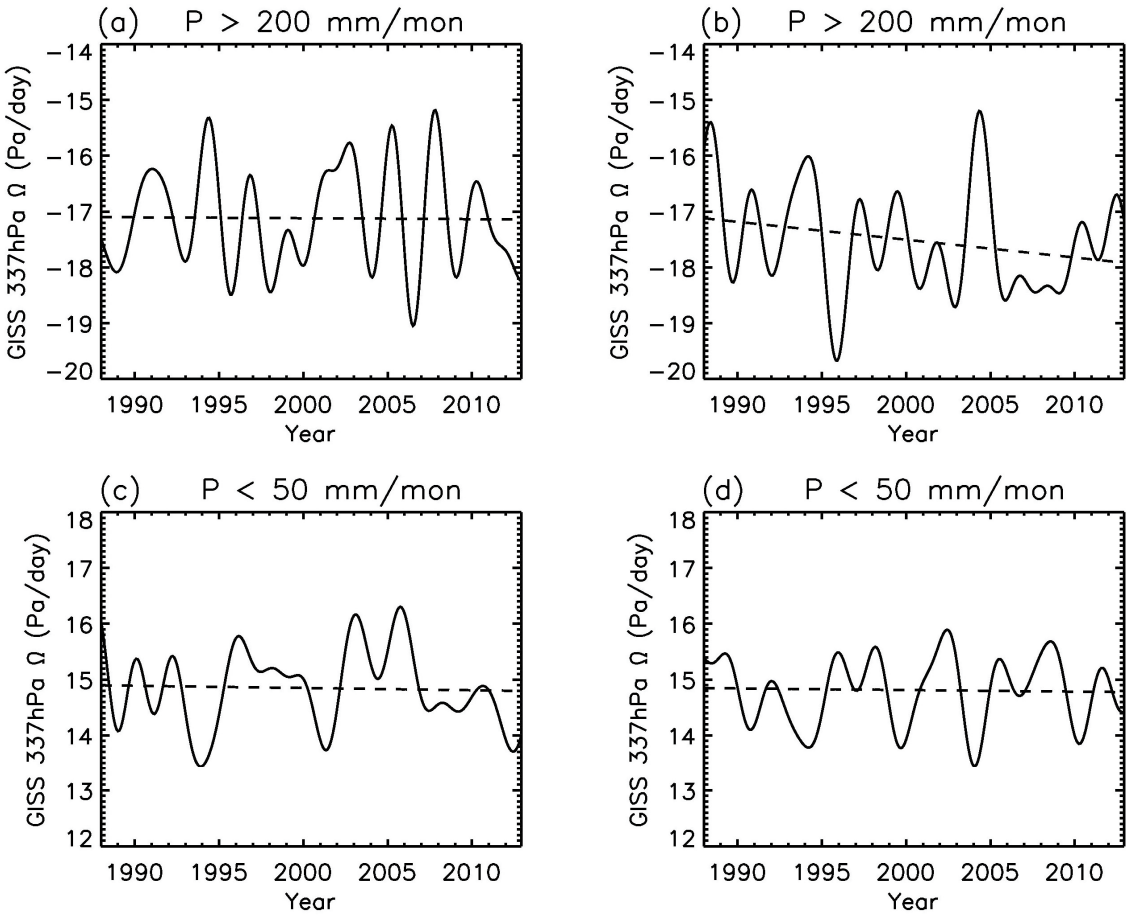

Figure 5.5. Lowpass filtered time series for 337 hPa vertical pressure velocity Ω (dP/dt) from GISS-HYCOM. (a) Ω over high precipitation (P > 200 mm/mon) from the control run (solid line) and trend (dashed line). (b) Ω over high precipitation area from the historic run (solid line) and trend (dashed line). (c) Same as (a) except for areas with precipitation < 50 mm/mon. (d) Same as (b) except for areas with precipitation < 50 mm/mon.

To better understand the possible physics in the temporal variation of precipitation, we examine omega (vertical pressure velocity) Ω = dP/dt, in the GISS model over the wet and dry areas. Results for Ω at 337 hPa are given in Figure 5.5. Corresponding trends in the control simulation for the wet areas are -0.016 ± 0.17 Pa/day/decade with -0.04 ± 0.18 Pa/day/decade for the dry areas. Trends for the 337 hPa Ω in the historic run are -0.32 ± 0.18 Pa/day/decade over the wet areas and -0.03 ± 0.21 Pa/day/decade over the dry areas,

as demonstrated in Figures 5.5b and 5.5d. Figure 5.5b illustrates a significant negative trend in the 337 hPa vertical pressure velocity. This negative trend suggests that the rising air is strengthening over the wet areas and, in turn, can lead to enhanced precipitation there. The temporal variation of the vertical pressure velocity is consistent with a mechanism suggested in some previous studies (Chou and Neelin, 2004; Chou *et al*., 2009), in which the gross moist stability of the atmospheric boundary layer is reduced due to increased moisture; and hence, the convection and the related precipitation is amplified. Our investigation of the column water vapor and temperature suggests positive trends of column water vapor and temperature over the dry areas. Furthermore, the GISS historic run reveals that the vertical pressure velocity did not significantly change during the past two decades over the dry areas. The temporal trend of precipitation over the dry areas poses a challenge to our current understanding, which will be explored in the future.

Table 5.1: Trends for precipitation (P), column water (W), temperature (T), and omega (Ω) over wet area (P > 200 mm/mon) and dry area (P < 50 mm/mon).

	Wet Area (P > 200 mm/mon)	Dry Area (P < 50 mm/mon)
GPCP P	**6.57 ± 0.27 mm/mon/decade**	**-0.98 ± 0.23 mm/mon/decade**
GISS P (Control Simulation)	**0.02 ± 0.19 mm/mon/decade**	**-0.03 ± 0.24 mm/mon/decade**
GISS P (Historic Simulation)	**3.8 ± 0.17 mm/mon/decade**	**-0.48 ± 0.21 mm/mon/decade**
GISS W (Control Simulation)	**-0.06 ± 0.18 mm/mon/decade**	**0.057 ± 0.20 mm/mon/decade**
GISS W (Historic Simulation)	**1.15 ± 0.21 mm/mon/decade**	**0.49 ± 0.20 mm/mon/decade**
GISS T (Control Simulation)	**-0.04 ± 0.19 °C/decade**	**-0.04 ± 0.20 °C/decade**
GISS T (Historic Simulation)	**0.61 ± 0.23 °C/decade**	**0.52 ± 0.22 °C/decade**
GISS Ω (Control Simulation)	**-0.016 ± 0.17 Pa/day/decade**	**-0.04 ± 0.18 Pa/day/decade**
GISS Ω (Historic Simulation)	**-0.32 ± 0.18 Pa/day/decade**	**-0.03 ± 0.21 Pa/day/decade**

5.4 Residual Meridional Stream Function from Model Simulation

Having achieved robust results examining the multiple observational data sets and performing statistical analyses, we now study the physics behind the temporal variations and spatial patterns of precipitation and their response to global warming. The GISS-HYCOM model is utilized to examine the temporal variation of residual meridional circulations over the last twenty years. Residual meridional circulation can be calculated using the following formulas:

$$\overline{\psi^*} = -\int \overline{v^*} dz \quad \overline{\psi^*} = \int \overline{w^*} dy ,$$

where $\overline{\psi^*}$ is the residual meridional circulation. $\overline{v^*}$ and $\overline{w^*}$ are the meridional and vertical residual velocities, which can be calculated using the following equations:

$$\overline{v^*} = \overline{v} - \rho_0^{-1} \partial(\rho_0 \overline{v'\theta'} / \theta_{0z}) / \partial z$$
$$\overline{w^*} = \overline{w} + \partial(\overline{v'\theta'} / \theta_{0z}) / \partial y ,$$

where v and w are the meridional and vertical velocity, ρ is the density, θ is the potential temperature, and θ_{0z} is the vertical derivative of the reference potential temperature. The overbar and prime denote the zonal average and its deviation from zonal mean, respectively.

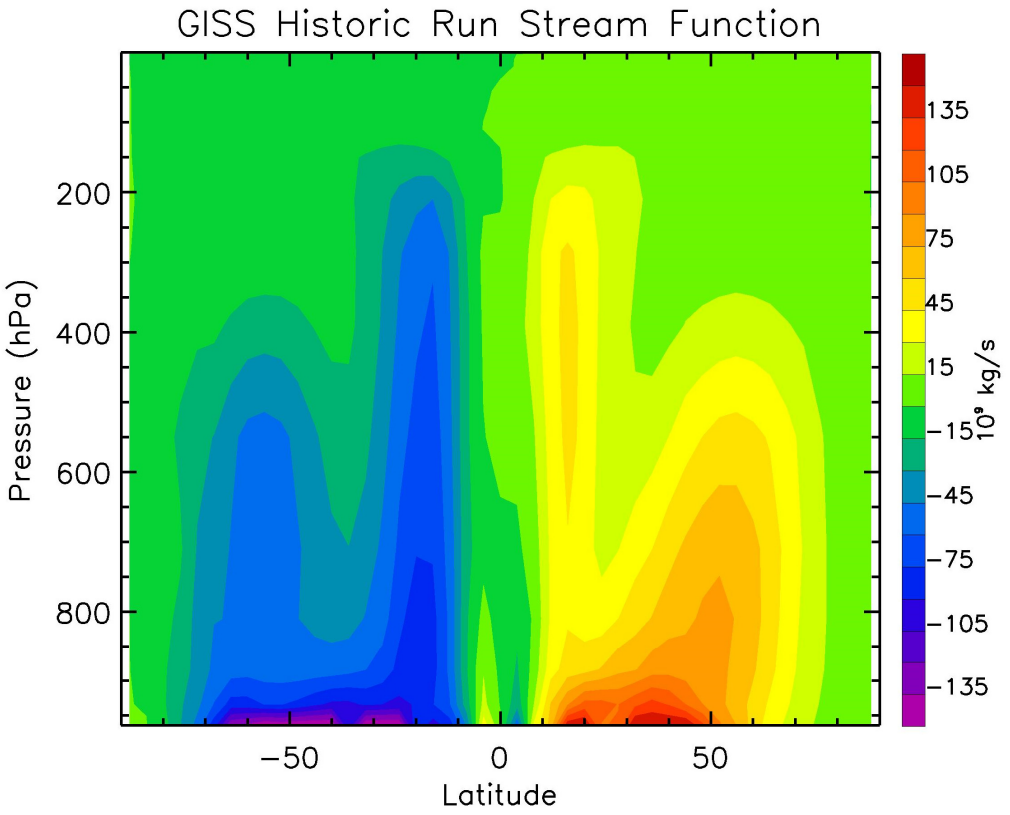

Figure 5.6. Climatological residual meridional stream function from the GISS-HYCOM model simulation historic run.

The resulting climatological residual meridional stream function from the GISS-HYCOM historic simulation is shown in Figure 5.6. From Figure 5.6, areas represented by red and yellow colors signify positive values, which demonstrate clockwise flow within the northern hemisphere. Areas represented by blue and purple colors signify negative values that show counterclockwise flow within the southern hemisphere. The model simulation supplies a good qualitative comparison with the observed stream function. The residual meridional circulation consists of a single thermally direct overturning in each hemisphere, with the strongest cell in the winter hemisphere owing to

a stronger horizontal temperature gradient present between the equator and pole and stronger wave activity (Chen, 2013). The tropical circulation is characterized by an intense updraft within 10° latitude of the summer hemisphere, crossing the equator in the upper troposphere, and then descending some in the subtropics of the winter hemisphere. The extratropical circulation rises from the subtropical lower troposphere to the extratropical upper troposphere. The high-latitude subsidence moves equatorward near the surface where it intersects the ground, completing the mean circulation.

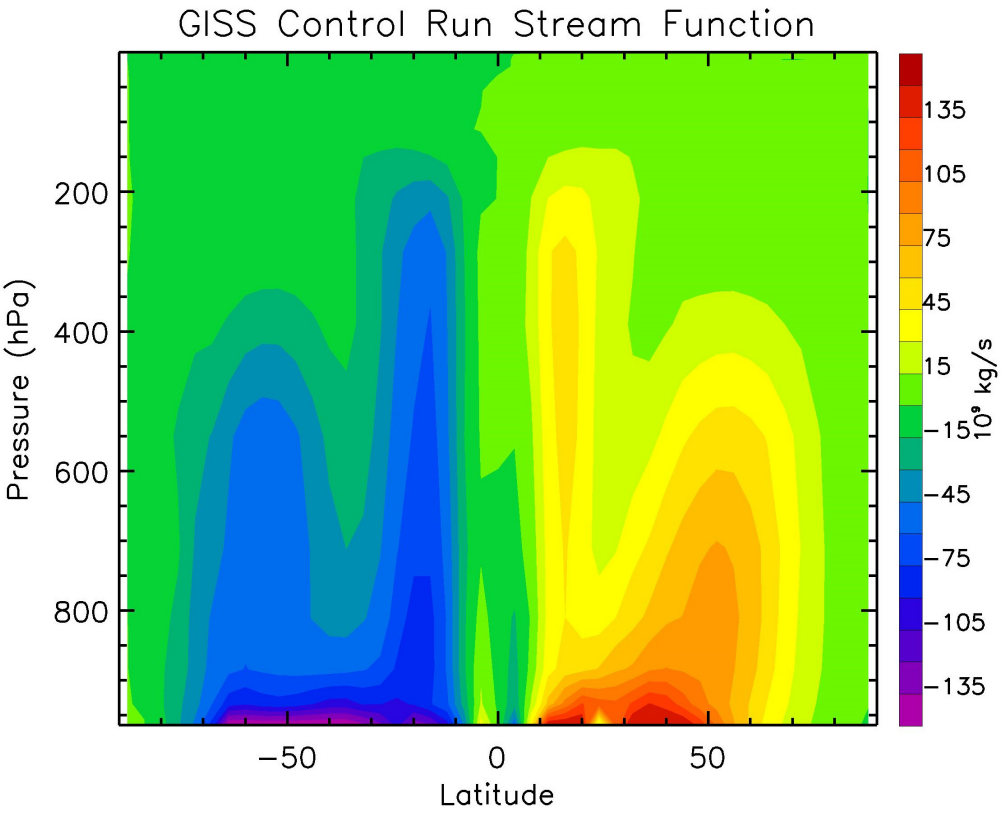

Figure 5.7. Climatological residual meridional stream function from the GISS-HYCOM model simulation control run.

Figure 5.7 illustrates the climatological residual meridional stream function from the GISS-HYCOM model simulation control run. The residual circulation transfers mass and trace chemicals upward across the tropopause in the tropics and downward in the extratropics (Holton, 2004). The wave-induced hemispheric scale circulation consists of upward and poleward motion across the isentropes in low latitudes, accompanied by diabatic heating, and downward motion across the isentropes at high latitudes, accompanied by diabatic cooling. In the lower stratosphere, zonal mean transport mainly takes the form of advection by the mean diabatic circulation in the meridional plane and eddy mixing approximately along isentropic surfaces (Holton, 2004). According to Holton, only if there is net diabatic heating or cooling can there be mean transport across the isentropes; that is, the circulation in which parcels that rise are diabatically heated and those that sink are diabatically cooled in order that their potential temperatures adjust to the local environment. The time-averaged residual meridional circulation approximates the mean motion of air parcels and provides an approximation to the mean meridional and vertical transport of trace substances. The spatial pattern of the climatological residual meridional circulation from the GISS-HYCOM control run is similar to that of the GISS-HYCOM historic run.

To better explore the influence of greenhouse gases on the meridional circulation, we calculated the time series of residual vertical velocity $\overline{w^*}$ averaged over 15°N-15°S from the GISS-HYCOM control run and GISS-HYCOM historic run. Results are shown in Figure 5.8. In general, the increasing precipitation over the ITCZ area (i.e., rich-get-richer) is accompanied by an intensifying convection over the tropical region. This intensifying convection can be seen by the increasing trend of residual vertical velocity

shown in Figure 5.8a of the model simulation. The residual vertical velocity displayed in Figure 5.8a is the result of the GISS-HYCOM model historic simulation containing varying greenhouse gases. Detailed data analysis reveals a 1.59 ± 0.8 m/day/decade increasing trend for years 1988-2013. Figure 5.8b illustrates the GISS-HYCOM model control simulation containing greenhouse gas concentrations at pre-industrial levels. Detailed data analysis reveals a 0.06 ± 0.76 m/day/decade trend for years 1988-2013. The historic simulation reveals a robust trend while the control run does not. The lack of an increasing trend in the control simulation supplies evidence of the influence anthropogenic greenhouse gas emissions have on the residual vertical velocity. The increasing trend demonstrated in the historic simulation suggests an intensifying convection is occurring over the tropical region, and thus aiding in the enhanced precipitation experienced in those regions. Such an intensifying convection is associated with a strong meridional circulation, making the large scale meridional circulation one more perspective in examining the temporal variation of tropical precipitation.

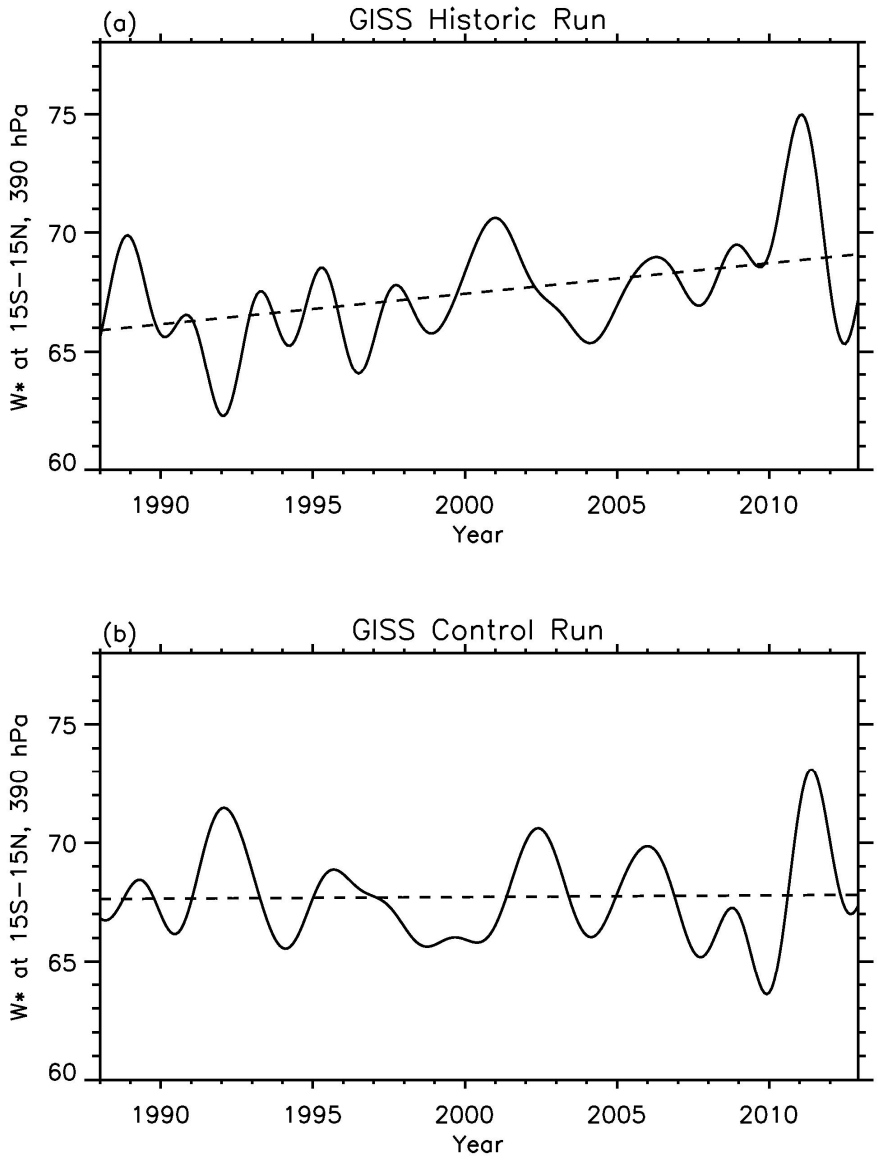

Figure 5.8. (a) Residual vertical velocity from GISS-HYCOM model historic simulation containing varying greenhouse gases from 15°N-15°S latitude. (b) Same as (a) except control simulation containing greenhouse gas concentrations at pre-industrial levels.

Comparison of the control and perturbed simulations from the GISS residual vertical velocity illustrates variations in meridional circulation as a result of global

warming, which can further aid in the increased precipitation over the tropical regions. Correct simulation of these important features by the climate model help to elucidate the physics behind the different temporal variations of precipitation, paving the way for more accurate prediction of future climate change driven by anthropogenic activities.

5.5 Conclusions

The GISS model simulations imply that the increasing greenhouse gases can affect the temporal variations of precipitation over the wet and dry areas, consistent with the observed "rich-get-richer" mechanism. The historic precipitation data in the wet areas illustrate an increasing trend of getting wetter while the dry areas are trending to be drier. The control run precipitation data containing fixed amounts of greenhouse gases do not demonstrate trends over the wet and dry areas. Additionally, the diagnostic studies of the simulations from the GISS model residual meridional stream function reveal that the atmospheric dynamics related to the convective stability, and hence the vertical motions, contribute to the increased precipitation over the tropical area. The residual vertical velocity from the GISS-HYCOM historic simulation shows a robust trend while the control run does not. The lack of an increasing trend in the control simulation supplies evidence of the influence anthropogenic greenhouse gas emissions have on the residual vertical velocity. The increasing trend demonstrated in the historic simulation suggests an intensifying convection is occurring over the tropical region. This aids in the enhanced precipitation experienced in those regions from which such an intensifying convection associates with a strong meridional circulation.

5.6 Acknowledgements

This work was supported by the NASA ROSES-2010 NEWS grant NNX13AC04G. Additionally, I would like to thank Dr. Liming Li, whose comments, insight, and previous research were invaluable to me concerning this chapter.

Chapter 6

Conclusions

This work utilized meteorological data sets, satellite observations, and climate models to study the temporal and spatial variability of precipitation.

First, our study revealed that the maximum cross correlation coefficient between precipitation and Southern Oscillation Index (SOI) was 0.5 when the lag is 5 months, suggesting that decreasing rainfall over Texas may appear five months after a period of increasing SOI, providing a possible forecasting factor for drought over Texas. To further explain the temporal variability of precipitation over Texas, we explored the relationship between vertical velocity and rainfall during 2011. The time series for precipitation and vertical velocity reveals they are related by the enhanced sinking motion and increased atmospheric stability. A statistical tool called Principal Component Analysis (PCA) was used to further explore the temporal and spatial variability of precipitation. The correlation between TRMM PC1 and SOI suggests the greatest variance is related to ENSO.

Second, further PCA was applied to the GPCP precipitation data set and CAM5 model. Results for the tropical domain show the spatial pattern of the precipitation anomalies regressed on the first PC illustrate positive precipitation anomalies over western Pacific and negative anomalies over central and eastern Pacific, which is verified by a recent study between GPCP rainfall anomalies and Niño3 Index (Ashok *et al*.,

2007). Spatial patterns of the PC2 mode illustrate positive precipitation anomalies over central Pacific and negative precipitation anomalies over western and eastern Pacific, which can be explained by the unique tripole nature of the SSTA caused by El Niño Modoki. The correlation between GPCP PC1 and SOI illustrates relation to ENSO while the correlation between GPCP PC2 and EMI suggests the second mode is related to the phenomenon known as El Niño Modoki. Comparison of CAM5 precipitation simulations produced a very similar correlation with that of the observed GPCP. CAM5 spatial patterns are consistent with the observed GPCP, although magnitudes are somewhat under predicted for both modes.

Third, results for the polar domain show the spatial pattern of precipitation anomalies regressed upon PC1 of Arctic GPCP precipitation were found to be approximately zonally symmetric with negative precipitation anomalies in the polar region and positive precipitation anomalies in the mid-latitudes. The spatial pattern of Antarctic GPCP precipitation was found to strongly resemble the first mode in the northern hemisphere (NH) when associated with the Southern Hemisphere Annular Mode (SAM). The correlation between Arctic GPCP PC1 and NAM index suggests when a stronger polar vortex exists, the NAM index is positive, and there are negative precipitation anomalies over the polar region and positive anomalies in the mid-latitudes. The leading PC1 of Antarctic GPCP precipitation compared with SAM index shows a good correlation and gives evidence of a stronger polar vortex in the SH when the SAM index is positive, leading to less precipitation in the SH high latitudes. CAM5 precipitation simulations demonstrate patterns similar to that of the observed GPCP; yet,

they do not capture the high precipitation anomalies over the NH Pacific Ocean and additionally position the positive precipitation anomalies slightly different in the SH.

Finally, the GISS model simulations imply that the increasing greenhouse gases can affect the temporal variations of precipitation over the wet and dry areas, consistent with the observed "rich-get-richer" mechanism. The historic precipitation data in the wet areas illustrate an increasing trend of getting wetter while the dry areas are trending to be drier. The control run precipitation data containing fixed amounts of greenhouse gases do not demonstrate trends over the wet and dry areas. The consistency between the historic GISS simulation and the GPCP precipitation suggests that the model can qualitatively capture the temporal trends of precipitation over the wet and dry areas. However, the precipitation trends are weaker in the model than in the observation. Additionally, the diagnostic studies of the simulations from the GISS model residual meridional stream function reveal that the atmospheric dynamics related to the convective stability, and hence the vertical motions, contribute to the increased precipitation over the tropical area. The residual vertical velocity from the GISS-HYCOM historic simulation illustrates a robust trend while the control run does not demonstrate a significant trend. The lack of an increasing trend in the control simulation supplies evidence of anthropogenic greenhouse gas influence on the residual vertical velocity. The increasing trend demonstrated in the historic simulation suggests an intensifying convection is occurring over the tropical region thus aiding in the enhanced precipitation experienced in those regions from which such an intensifying convection associates with a strong meridional circulation. However, the vertical motion in the dry

areas does not show significant change, making the physics of the negative trend of precipitation in these regions more complicated.

With increasing numbers of weather extremes related to climate change, it is important to investigate precipitation, temperature, and water vapor trends and their associated spatial distribution. The significance and broader impacts are evident when we look at the consequences of increased drought in some areas and flooding in others. Droughts create a heightened threat for fire weather and diminish the water supply with economic impacts taking years of recovery. On the other hand, rapid and abundant rainfall causes flooding and threatens life and property. My hope is that this research will provide insight into the causes of precipitation extremes that may be related to the influence of global warming. Armed with this knowledge, forecasters can better predict when and where these extremes may happen, and scientists can forge a path to alleviate their occurrences and severity.

References

Adler, R. F., G. J. Huffman, A. Chang, R. Ferraro, P. Xie, J. Janowiak, B. Rudolf, U. Schneider, S. Curtis, D. Bolvin, A. Gruber, J. Susskind, and P. Arkin, 2003: The version 2 global precipitation climatology project (GPCP) monthly precipitation analysis (1979-present). *J. Hydrometeorology*, **4**, 1147-1167.

Adler, R. F., G. J. Gu, J. J. Wang, G. J. Huffman, S. Curtis, and D. Bolvin, 2008: Relationships between global precipitation and surface temperature on interannual and longer timescales (1979-2006). *J. Geophysical Research*, **113**, 22, 104.

Ahrens, C. Donald, 2006: Meteorology Today, Eighth Edition, Cengage Learning, pp. 275-278, ISBN 111179569X, 9781111795696.

Allan, R. P., and B. J. Soden, 2007: Large discrepancy between observed and simulated precipitation trends in the ascending and descending branches of the tropical circulation. *Geophysical Research Letters*, **34**, 187-205.

Allan, R. P., and B. J. Soden, 2008: Atmospheric warming and the amplification of precipitation extremes. *Science*, **321**, 1481-1484.

Allan, R. P., B. J. Soden, V. O. John, W. Ingram, and P. Good, 2010: Current changes in tropical precipitation. *Environmental Research Letters*, **5**, doi:10.1088/1748-9326/5/2/025205.

Allen, M. R., and W. J. Ingram, 2002: Constraints on future changes in climate and the hydrological cycle. *Nature*, **419**, 224-232.

Ashok, K., S. K. Behera, S. A. Rao, H. Weng, and T. Yamagata, 2007: El Niño Modoki and its possible teleconnection. *J. Geophysical Research,* **112**, 110-07.

Baldwin, M. P. and T. J. Dunkerton, 1999: Propagation of the Arctic Oscillation from the stratosphere to the troposphere. *J. Geophysical Research*, **104**, 30, 937-30, 946.

Baldwin, M. P. and T. J. Dunkerton, 2001: Stratospheric harbingers of anomalous weather regime. *Science*, **294,** 581-584.

Baldwin, M.P., D. B. Stephenson, I. T. Jolliffe, 2007: Spatial weighting and iterative projection methods for EOFs. *J. Climate*, **20**, 1578-1594.

Bevington, P. R. and D. K. Robinson, 2003: Data Reduction and Error Analysis for the Physical Sciences. Third Edition (New York: McGraw-Hill).

Bony, S., G. Bellon, D. Klocke, S. Sherwood, S. Fermepin, and S. Denvil, 2013: Robust direct effect of carbon dioxide on tropical circulation and regional precipitation. *Nature Geoscience*, **6**, 447-451.

Bosilovich, M. G., S. D. Schubert, G. K. Walker, 2005: Global changes of the water cycle intensity. *J. Climate,* **18**, 1591-1608.

Bretherton, C. S., M. Widmann, V. P. Dymnikov, J. M. Wallace, and I. Blade, 1999: The effective number of spatial degrees of a time varying field. *J. Climate*, **12**, 1990-2009.

Brutsaert, W., 1998: Land-surface water vapor and sensible heat flux: Spatial variability, homogeneity, and measurement scales. *Water Resources Research,* **34(10)**, 2433–2442.

Camp, C. D., M. S. Roulston, and Y. L. Yung, 2003: Temporal and spatial patterns of the interannual variability of total ozone in the tropics. *J. Geophysical Research,* **108**, 43-46, doi:10.1029/2001JD001504.

Cavazos, T., 1999: Large-scale circulation anomalies conducive to extreme precipitation events and derivation of daily rainfall in northeastern Mexico and southeastern Texas. *J. Climate*, **12**, 1506–1523.

Chahine, M. T., 1992: The hydrological cycle and its influence on climate. *Nature,* **359**, 373-380.

Chahine M. T., Haskins R., and Fetzer E., 1997: Observation of the recycling rate of moisture in the atmosphere: 1988–1994. *GEWEX,* **7,** 1–4.

Chang, C. P. and T. Li, 2000: A theory for the tropical tropospheric biennial oscillation. *J. Atmospheric Sciences,* **57,** 2209-2224.

Chang, C. P., and T. Li, 2001: Nonlinear interactions between the TBO and ENSO, east Asian and western Pacific meteorology and climate. *Book Series on East Asian Meteorology, World Scientific Publishing Company,* Singapore, **1,** 25-38.

Chang, E. K. M., and Y. Fu, 2002: Interdecadal variations in Northern Hemisphere winter storm track intensity. *J. Climate*, **15**, 642–658.

Chen, Gang, 2013: The mean meridional circulation of the atmosphere using the mass above isentropes as the vertical coordinate. *J. Atmospheric Sciences,* **70:7**, 2197-2213.

Chou, C., and J. D. Neelin, 2004: Mechanisms of global warming impacts on regional tropical precipitation. *J. Climate*, **17**, 2688-2701.

Chou, C., J. D. Neelin, C. A. Chen, and J. Y. Tu, 2009: Evaluating the "rich-get-richer" mechanism in tropical precipitation change under global warming. *J. Climate*, **22**, 1982-2005.

Chou, C., J. C. H. Chiang, C. Lan, C. Chung, Y. Liao, and C. Lee, 2013: Increase in the range between wet and dry season precipitation. *Nature Geoscience*, **6**, 263-267.

Curry, J. A., and J. L. Schramm, 1994: Sea ice-albedo climate feedback mechanism. *J. Climate,* **8,** 240-247.

Dai, A., K. E. Trenberth, and T. Qian, 2004: A global data set of Palmer Drought Severity Index for 1870-2002: Relationship with soil moisture and effects of surface warming. *J. Hydrometeorology*, **5**, 1117-1130.

Dickinson, R. E., and R. J. Cicerone, 1986: Future global warming from atmospheric trace gases. *Nature*, **319**, 109-115.

Durack, P. J., S. E. Wijffels, and R. J. Matear, 2012: Ocean salinities reveal strong global water cycle intensification during 1950 to 2000. *Science*, **27**, 455-458.

Eisenman, Ian, Lisan Yu, and Eli Tziperman, 2005: Westerly Wind Bursts: ENSO's Tail Rather than the Dog?. *J. Climate*, **18**, 5224–5238.

Gill, Adrian E., 1982: Atmosphere–Ocean Dynamics, International Geophysics Series 30, Academic Press, pp. 378–380, ISBN 978-0-12-283522-3.

Gilman, D. L., F. J. Fuglister, and J. M. Mitchell, 1963: On the power spectrum of red noise. *J. Atmospheric Sciences*, **20**, 182-184.

Gu, G. J., R. F. Adler, G. J. Huffman, and S. Curtis, 2007: Tropical rainfall variability on interannual-to-interdecadal and longer time scales derived from the GPCP monthly product. *J. Climate*, **20**, 4033-4046.

Gu, G. J., and R. F. Adler, 2012: Interdecadal variability/long-term changes in global precipitation patterns during the past three decades: global warming and/or pacific decadal variability. *Climate Dynamics*, doi:10.1007/s00382-012-1443-8.

Heim, R. R., Jr., 2002: A review of twentieth-century drought indices used in the United States. *Bulletin of the American Meteorological Society*, **83**, 1149–1165.

Held, I. M., and B. J. Soden, 2006: Robust responses of the hydrological cycle to global warming. *J. Climate*, **19**, 5686-5699.

Holland, M. M. and C. M. Bitz, 2003: Polar amplification of climate change in coupled models. *Climate Dynamics,* **21,** 221-232, doi:10.1007/s00382-003-0332-6.

Holton, James R., 2004: An Introduction to Dynamic Meteorology, Fourth Edition, Academic Press, pp. 325, ISBN 0123540151, 9780123540157.

Hoskins, B. J., Draghici, I., and Davies, H. C., 1978: A new look at the ω-equation. *Quarterly J. of the Royal Meteorological Society*, **104**, 31-38.

Huffman, G. J., R. F. Adler, P. Arkin, A. Chang, R. Ferraro, A. Gruber, J. Janowiak, A. McNab, B. Rudolf, and U. Schneider, 1997: The global precipitation climatology project (GPCP) combined precipitation data set. *Bulletin of the American Meteorological Society,* **78**, 5-20.

Huffman, G. J., *et al*., 2007: The TRMM multi-satellite precipitation analysis: Quasi-Global, Multi-Year, Combined-Sensor precipitation estimates at fine scale. *J. Hydrometeorology,* **8**, 33-55.

Huffman, G. J., R. F. Adler, D. T. Bolvin, and G. J. Gu, 2009: Improvements in the GPCP global precipitation record: GPCP Version 2.1. *Geophysical Research Letters*, **36**, doi:10.1029/2009GL040000.

Huffman, G. J., D. T. Bolvin, and R. F. Adler, 2012: GPCP version 2.2 combined precipitation data set. NCDC, Asheville, NC.

Iacono, M.J., Delamere, J.S., Mlawer, E.J., Shephard, M.W., Clough, S.A. and Collins, W.D., 2008: Radiative forcing by long-lived greenhouse gases: Calculations with the

AER radiative transfer models. *J. Geophysical Research,* **113**, 23-33, doi: 10.1029/2008JD009944.

Intergovernmental Panel on Climate Change (IPCC), 2001: Climate Change 2000—Third Assessment Report. *Cambridge University Press,* Cambridge.

IPCC, 2007: Climate Change 2007: The Physical Science Basis. Cambridge University Press, Cambridge, United Kingdom and New York, NY, USA.

IPCC, 2013: Climate Change 2013: The Physical Science Basis. IPCC Secretariat, World Meteorological Organization, 7bis Avenue de la Paix, P. O. Box No. 2300 CH-1211 Geneva 2, Switzerland.

Iskenderian, H., 1995: A 10-year climatology of Northern Hemisphere tropical cloud plumes and their composite flow patterns. *J. Climate*, **8**, 1630-1637.

Jiang, X., *et al*., 2004: Quasi-biennial oscillation and quasi-biennial oscillation-annual beat in the tropical total column ozone: A two dimensional model simulation. *J. Geophysical Research,* **109**, 1-10, doi:10.1029/2003JD004377.

Jiang, X., S. Pawson, C. D. Camp, E. Nielsen, R. Shia, T. Liao, K. Jeev, V. Limpasuvan, and Y. L. Yung, 2008a: Interannual variability and trends in extratropical ozone. Part I: Northern Hemisphere. *J. Atmospheric Sciences,* **65,** 3013-3029.

Jiang, X., Q. Li, M. Liang, R. L. Shia, M. T. Chahine, E. T. Olsen, L. L. Chen, and Y. L. Yung, 2008b: Simulation of upper troposphere CO_2 from chemistry and transport models. *Global Biogeochemical Cycles*, **22,** 123-142, doi:10.1029/2007GB003049.

Jiang, X., M. T. Chahine, E. T. Olsen, L. Chen, and Y. L. Yung, 2010: Interannual variability of mid-tropospheric CO_2 from Atmospheric Infrared Sounder. *Geophysical Research Letters*, doi:2010GL042823.

John, V. O., R. P. Allan, and B. J. Soden, 2009: How robust are observed and simulated precipitation responses to tropical ocean warming?. *Geophysical Research Letters,* **36**, 147-02.

Kanamitsu, M., *et al*., 2002: NCEP-DOE AMIP-II Reanalysis (R-2). *Bulletin of the American Meteorological Society***, 83**, 1631-1643.

Lambert, F. H., A. R. Stine, N. Y. Krakauer, J. C. H. Chiang, 2008: How much will precipitation increase with global warming?. *EOS,* **89**, 193-194.

Lau, K. M., and S. Yang, 1996: The Asian monsoon and predictability of the tropical ocean-atmosphere system. *Quarterly J. of the Royal Meteorological Society,* **122,** 945-957.

Li, L., X. Jiang, M. T. Chahine, E. T. Olsen, E. J. Fetzer, L. Chen, and Y. L. Yung, 2011: The recycling rate of atmospheric moisture over the past two decades (1988-2009). *Environmental Research Letters*, **6**, 1-6, doi:10.1088/1748-9326/6/3/034017.

Liang, M., L. Lin, K. K. Tung, Y. L. Yung, and S. Sun, 2013: Impact of climate drift on twenty-first-century projection in a coupled atmospheric-ocean general circulation model. *J. Atmospheric Sciences*, **70**, 3321-3327.

Liepert, B. G., M. Previdi, 2009: Do models and observations disagree on the rainfall response to global warming?. *J. Climate,* **22**, 3156-3166.

Limpasuvan, V. and D. L. Hartmann, 1999: Eddies and the annular modes of climate variability, *Geophysical Research Letters*, **26**, 3133-3136.

Liu, S. C., C. B. Fu, C. J. Shiu, J. P. Chen, and F. T. Wu, 2009: Temperature dependence of global precipitation extremes. *Geophysical Research Letters*, **36**, L17702.

Lydolph, P. E., 1989: The Climate of the Earth. Rowan and Littlefield, 386 pp.

Marvel, K., and C. Bonfils, 2013: Identifying external influences on global precipitation. *PNAS*, **110**, 19301-19306.

Meehl, G. A., 1997: The South Asian monsoon and the tropospheric biennial oscillation (TBO). *J. Climate,* **10,** 1921-1943.

Meehl, G. A., and J. M. Arblaster, 2002: The tropospheric biennial oscillation and Asian-Australian monsoon rainfall. *J. Climate,* **15,** 722-744.

Mooley, D. A., and B. Parthasarathy, 1984: Fluctuations in All-India summer monsoon rainfall during 1871-1978. *Climatic Change,* **6**, 287-301.

Morrison, Hugh, and Andrew Gettelman, 2008: A new two-moment bulk stratiform cloud microphysics scheme in the Community Atmosphere Model, Version 3 (CAM3). Part I: Description and numerical tests. *J. Climate*, **21**, 3642–3659.

Neale, R. B., J. H. Richter, and M. Jochum, 2008: The impact of convection on ENSO: From a delayed oscillator to a series of events. *J. Climate*, **21**, 5904–5924.

Neelin, J. D., M. Munnich, H. Su, J. E. Meyerson, and C. E. Holloway, 2006: Tropical drying trends in global warming models and observations. *PNAS*, **103**, 6110-6115.

Nielsen-Gammon, J. W., 2011: OSC Report: The 2011 Texas Drought. The Office of the State Climatologist, 1-43.

Park, S. and C. S. Bretherton, 2009: The University of Washington shallow convection and moist turbulence schemes and their impact on climate simulations with the Community Atmosphere Model. *J. Climate,* **22**, 3449–3469.

Polson, D., G. C. Hegerl, R. P. Allan, and B. Balan Sarojini, 2013: Have greenhouse gases intensified the contrast between wet and dry regions?. *Geophysical Research Letters*, **40**, 4783-4787.

Preisendorfer, R. W., 1988: Principal component analysis in meteorology and oceanography. *Development in Atmospheric Sciences,* **17,** 425.

Press, W., S. Teukolsky, W. Vetterling, and B. Flannery, 1992: Numerical Recipes in Fortran 77: The Art of Scientific Computing. Cambridge Univ. Press, New York, 933 pp.

Räisänen, J., 2001: CO_2-induced climate change in CMIP2 experiments: Quantification of agreement and role of internal variability. *J. Climate*, **14,** 2088–2104.

Rasmusson, E. M. and K. Mo, 1993: Linkages between 200-mb tropical and extratropical circulation anomalies during the 1986-1989 ENSO cycle. *J. Climate*, **6**, 595-616.

Richard, P. A., B. J. Soden, V. O. John, W. Ingram, P. Good, 2010: Current changes in tropical precipitation. *Environmental Research Letters,* **5**, 1-7.

Richman, M. B., 1986: Rotation of principal components. *J. Climatology*, **6**, 293-335.

Ropelewski, C. F., M. S. Halpert, and X. Wang, 1992: Observed tropospheric biennial variability and its relationship to the Southern Oscillation. *J. Climate,* **5,** 594-614.

Santer, B. D., *et al*., 2007: Identification of human-induced changes in atmospheric moisture content. *PNAS*, **104**, 15248-15253.

Salby, M., 2012: Physics of the Atmosphere and Climate. Cambridge University Press, pp. 666, ISBN 0521767180.

Schneider, U., T. Fuchs, A. Meyer-Christoffer, and B. Rudolf, 2008: Global precipitation analysis products of the GPCC, 12 pp., Deutscher Wetterdienst, Offenbach am Main, Germany.

Schultz D. M., Daniel Keyser, and Lance F. Bosart, 1998: The effect of large-scale flow on low-level frontal structure and evolution in mid-latitude cyclones. *Monthly Weather Review*, **126**, 1767–1791.

Shen, S., and K. M. Lau, 1995: Biennial oscillation associated with the East Asian monsoon and tropical sea surface temperatures. *J. Meteorological Society Japan,* **73,** 105-124.

Shindell, D. T., G. Faluvegi, R. L. Miller, G. A. Schmidt, J. E. Hansen, and S. Sun, 2006: Solar and anthropogenic forcing of tropical hydrology. *Geophysical Research Letters*, **33**, doi:10.1029/2006GL027468.

Stephens, G. L., and T. D. Ellis, 2008: Controls of global-mean precipitation increases in global warming GCM experiments. *J. Climate*, **21**, 6141-6155.

Thompson, D. W. J., and J. M. Wallace, 1998: The Arctic Oscillation signature in the wintertime geopotential height and temperature fields. *Geophysical Research Letters*, **25**, 1297-1300.

Thompson, D. W. J., and J. M. Wallace, 2000: Annular modes in the extratropical circulation. Part I: Month-to-month variability. *J. Climate,* **13,** 1000-1016.

Tian, S. F., and T. Yasunari, 1992: Time and space structure of interannual variation in summer rainfall over China. *J. Meteorological Society Japan,* **70,** 585-596.

Trammell, J. H., X. Jiang, L. Li, M. Liang, M. Li, J. Zhou, E. Fetzer, and Y. Yung. Investigation of precipitation variations over wet and dry areas from observation and model. *Advances in Meteorology*, Submitted, 2015.

Trenberth, K. E., and D. J. Shea, 1987: On the evolution of the Southern Oscillation event. *Monthly Weather Review,* **115,** 3078-3096.

Trenberth, K. E., 1997: The definition of El Niño. *Bulletin of the American Meteorological Society,* **78**, 2771-2777.

Trenberth, K. E., 1998: Progress during TOGA in understanding and modeling global teleconnections associated with tropical sea surface temperatures. *J. Geophysical Research,* **103,** 14291-14324.

Trenberth, K. E., *et al*., 2003: The changing character of precipitation. *Bulletin of the American Meteorological Society*, **84**, 1205-1217.

Trenberth, K. E., J. Fasullo, and L. Smith, 2005: Trends and variability in column-integrated atmospheric water vapor. *Climate Dynamics*, **24**, 741-758.

Trenberth, K. E., and D. J. Shea, 2005: Relationships between precipitation and surface temperature. *Geophysical Research Letters*, **32**, L14703.

Trenberth, K. E., 2010: Changes in precipitation with climate change. Climate Research, doi:10.3354/cr00953, In Press.

Tuller, Stanton, 1968: World distribution of mean monthly and annual precipitable water. *Monthly Weather Review*, **96**, 785–797.

Uppala, S. M., *et al*., 2005: The ERA-40 reanalysis. *Quarterly J. of the Royal Meteorological Society,* **131**, 2961-3012.

Wang, J. J., R. F. Adler, G. J. Gu, 2008: Tropical rainfall-surface temperature relations using tropical rainfall measuring mission precipitation data. *J. Geophysical Research-Atmospheres,* **113**, D18115.

Waliser, D. E., and C. Gautier, 1993: A satellite-derived climatology of the ITCZ. *J. Climate*, **6**, 2162-2174.

Webster, P. J., A. M. Moore, J. P. Loschnigg, and R. R. Leben, 1998: Coupled ocean-atmosphere dynamics in the Indian Ocean during 1997-98. *Nature,* **401,** 356-360.

Weng, H., K. Ashok, S. K. Behera, S. A. Rao, and T. Yamagata, 2007: Impacts of recent El Niño Modoki on dry/wet conditions in the Pacific rim during boreal summer. *Climate Dynamics*, **29**, 113-129.

Wentz, F. J., L. Ricciardulli, K. Hilburn, 2007: How much more rain will global warming bring?. *Science,* **317**, 233-235.

Yasunari, T. and R. Suppiah, 1988: Some problems on the interannual variability of Indonesian monsoon rainfall. *Tropical Rainfall Measurements,* J. S. Theon and N. Fugono, Eds., Deepak, 113-122.

Yasunari, T., 1990: Impact of Indian monsoon on the coupled atmosphere ocean system in the tropical Pacific. *Meteorological Atmospheric Physics,* **44,** 29-41.

Yasunari, T., 1991: The monsoon year—A new concept of the climate year in the tropics. *Bulletin of the American Meteorological Society,* **72,** 1331-1338.

Zhang, G. J. and N. A. McFarlane, 1995: Sensitivity of climate simulations to the parameterization of cumulus convection in the Canadian climate centre general circulation model. *Atmosphere-Ocean*, **33**, 407-446.

Zhang, C., 2005: Madden-Julian oscillation. *Reviews of Geophysics,* **43**, RG2003, doi:10.1029/2004RG000158.